Catalytic Oxidation of Volatile Organic Compounds Over Co3O4-based Catalysts

Guangtao Chai

Université Claude Bernard Lyon 1

THESE de DOCTORAT DE
L'UNIVERSITE CLAUDE BERNARD LYON 1
EN COTUTELLE AVEC L'UNIVERSITE DES SCIENCES ET TECHNOLOGIES DE LA CHINE DE L'EST - SHANGHAI.

Ecole Doctorale N° 206
Ecole Doctorale de Chimie de Lyon

Discipline : Catalyse industrielle

Soutenue publiquement 13/12/2023, par :
Guangtao Chai

Catalytic Oxidation of Volatile Organic Compounds Over Co3O4-based Catalysts

Devant le jury composé de :

WANG, Xingyi	Professeure East China University of Science and Technology	Présidente
COURTOIS, Xavier	Maître de Conférences Université de Poitiers	Rapporteur
WU, Peng	Professeur East China Normal University	Rapporteur
BRIANCON, Stephanie	Professeure des Universités Université Claude Bernard Lyon 1	Examinatrice
VALVERDE, José Luis	Professeur Université de Castilla La Mancha	Examinateur
GIROIR-FENDLER, Anne	Professeure des Universités Université Claude Bernard Lyon 1	Directeurice de thèse
GUO, Yanglong	Professeur East China University of Science and Technology	Co-directeur de thèse

挥发性有机化合物在 Co_3O_4 基催化剂上的催化氧化研究

摘要

随着我国经济的快速发展，挥发性有机化合物(VOCs)的排放也日益增长。VOCs 的过量排放不仅对生态环境造成了严重的破坏，也对人类的生命健康有着致命的危害。催化氧化法因其操作条件温和、VOCs 净化效率高和无二次污染等优点，已成为 VOCs 净化的主要发展方向。本文围绕 VOCs 的催化氧化，基于密度泛函理论研究了氯乙烯在 Co_3O_4 催化剂上的催化氧化反应机理，而后设计制备了不同的 Co_3O_4 基催化剂，并将其用于多种 VOCs 的催化氧化反应中，系统研究了催化剂组成、结构、活性中心和催化性能之间的构效关系，为开发具有高活性和高稳定性的 Co_3O_4 基催化剂提供了理论基础。本文主要取得了以下研究成果：

基于密度泛函理论系统地研究了氯乙烯在 Co_3O_4 催化剂特定晶面((110)和(001))上的催化氧化反应机理。氯乙烯催化氧化的反应路径主要有三个步骤：氯乙烯吸附后 C-Cl 键的断裂、CH_2CH 基团的氧化以及 Cl 物种的消除。确定了氯乙烯在 Co_3O_4 表面上完全氧化的决速步骤是 Cl 物种的消除，而且最终产物中 HCl 比 Cl_2 更容易生成。通过两个晶面上氯乙烯氧化反应的对比，Co_3O_4(001)晶面对 Cl 脱除有着更低的能垒，从而具有更优异的氯乙烯催化氧化性能。

用溶胶凝胶法制备了一系列 Zr 改性(含量 ≥ 5 mol.%)的 Co_3O_4 催化剂，并研究了其对于氯乙烯催化氧化反应的性能。研究表明，含有 5 mol.% Zr 的 Co_3O_4 催化剂($Co_{95}Zr_5$)表现出最好的催化活性和稳定性，尤其是对含氯副产物的完全氧化。通过在 Co_3O_4 催化剂中引入少量的 Zr 可以调节氧化还原能力和增强表面酸性，从而提高其对氯乙烯的催化氧化性能。催化剂表面的 Co^{2+}和吸附氧物种含量随着 Zr 的加入而增多，促进了氯乙烯的催化氧化活性的提升。

用溶胶凝胶法制备了另一系列的适量 Zr(含量 ≤ 2 mol.%)掺杂的 Co_3O_4 催化剂，并将其用于丙烷的催化氧化。研究表明，只有很少一部分 Zr(~ 1 mol.%)可以被掺杂进入 Co_3O_4 晶格中。在 Zr 掺杂的催化剂中，Zr 引起 Co_3O_4 晶格畸变，形成更小的 Co_3O_4 晶粒尺寸、更大的比表面积、更好的氧化还原能力、更高的表面 Co^{2+}含量以及更多的表面氧空穴和活性氧物种。对丙烷催化氧化活性最好的催化剂是 1%Zr- Co_3O_4 催化剂，主要得益于其优异的低温可还原性和丰富的表面活性氧物种。原位红外实验研究表明，1%Zr-Co_3O_4 催化剂上丙烷催化氧化遵循 Mars-van Krevelen 机理。

基于适量 Zr 掺杂的 Co_3O_4 催化剂的实验结果，进一步探究了适量 Nb(含量 ≤ 1.5 mol.%)掺杂对 Co_3O_4 催化剂的影响，分别考察了其对丙烷和氯乙烯的催化氧化性能。研究表明，1%Nb-Co_3O_4 催化剂对丙烷和氯乙烯的催化氧化都表现出最好的催化活性，多氯副产物种类明显减少。Nb 的掺杂可以显著提升 Co_3O_4 催化剂的氧化还原能力和表面

酸性，增加表面 Co^{2+}、氧空穴和活性氧物种的含量，从而提升 Co_3O_4 催化剂的催化活性。原料气中存在一定含量水分时，1%Nb-Co_3O_4 催化剂对氯乙烯催化活性基本不受抑制，且最终产物中几乎没有氯气。该催化剂在丙烷和氯乙烯的催化氧化反应的稳定性测试中均表现出优异的性能。

分别用碳酸钠沉淀法和水热合成法制备了两个系列的 Co_3O_4 催化剂：具有不同含量残留 Na 的 Co_3O_4 催化剂和不同载体(YSZ 和 TiO_2)负载的 Co_3O_4 催化剂。残留 Na 可以部分进入 Co_3O_4 的晶格，引起晶格畸变，提高催化剂的比表面积，但同时它又降低催化剂的氧化还原性和氧的流动性，从而抑制其对丙烷氧化的催化性能。不同载体对负载型 Co_3O_4 催化剂的甲苯催化氧化性能产生了相反的作用。Co_3O_4 和 YSZ 载体之间的协同作用使得 Co_3O_4/YSZ 催化剂具有更好的氧化还原性、氧活化能力和氧流动性，从而表现出较好的甲苯氧化性能。而 Co_3O_4/TiO_2 催化剂较差的氧化还原性和氧活化能力抑制了其对甲苯氧化的催化性能。

关键词：挥发性有机化合物；Co_3O_4 基催化剂；催化氧化；氯乙烯；丙烷；甲苯

Oxydation catalytique des composés volatils sur des catalyseurs à base de Co_3O_4

Résumé

Avec le développement rapide de l'économie, les émissions de COV augmentent également. Les émissions excessives de COV peuvent non seulement causer de graves dommages à l'environnement écologique, mais aussi être mortelles pour la santé humaine. L'oxydation catalytique présente les avantages de conditions de fonctionnement douces, d'efficacité de purification élevée et d'absence de pollution secondaire. Elle est devenue l'une des principales orientations de développement de la purification des COV. Le mécanisme de réaction d'oxydation du chlorure de vinyle (VC) sur un catalyseur Co_3O_4 a été étudié sur la base de la théorie fonctionnelle de la densité. Différents catalyseurs à base de Co_3O_4 ont été conçus, synthétisés et étudiés pour leur oxydation catalytique de divers COV. Les relations Structure - performance entre la composition, la structure, la position active et les propriétés catalytiques des catalyseurs à base de Co_3O_4 ont été systématiquement étudiées, fournissant une base théorique pour le développement de catalyseurs de type Co_3O_4 hautement actifs et hautement stables. Les principaux résultats de recherche sont les suivants:

Le Mécanisme réactionnel catalytique de l'oxydation de VC sur deux surfaces représentatives de Co_3O_4, à savoir (110) et (001), a été étudié de manière systématique sur la base de la théorie fonctionnelle de la densité. La voie réactionnelle catalytique de l'oxydation du VC comprend trois étapes, la rupture de la liaison C-Cl après adsorption du VC, l'oxydation du CH_2CH et l'élimination des espèces Cl. L'étape de détermination de la vitesse d'oxydation du VC sur le catalyseur Co_3O_4 est déterminée pour éliminer les espèces Cl, et HCl est le produit chloré préféré au lieu de Cl_2. La barrière d'élimination du Cl de Co_3O_4(001) est faible par rapport à Co_3O_4(110), ce qui suggère des propriétés catalytiques potentiellement supérieures pour l'oxydation du VC.

Une série de catalyseurs Co_3O_4 modifiés par Zr (teneur en Zr ≥ 5 mol.%) a été préparée par la méthode sol-gel pour l'oxydation VC. Les résultats montrent que le catalyseur contenant 5% molaire de zirconium ($Co_{95}Zr_5$) présente une activité catalytique et une stabilité optimales, notamment pour l'oxydation complète des sous-produits chlorés. L'introduction de zirconium dans le catalyseur Co_3O_4 permet de modifier la réductibilité, d'améliorer l'acidité de surface et donc les performances catalytiques de l'oxydation du VC. Avec l'introduction du zirconium, la

quantité de Co^{2+} en surface et d'oxygène adsorbé augmente, favorisant l'oxydation catalytique du VC et améliorant l'activité catalytique des catalyseurs à base de Co_3O_4.

Une série de catalyseurs Co_3O_4 moyennement dopés Zr (teneur en Zr ≤ 2mol.%) a été préparée par la méthode sol - gel pour l'oxydation catalytique du propane. Les résultats montrent que seule une petite partie du zirconium (~ 1 mol.%) peut être dopée dans le réseau de Co_3O_4. Pour les catalyseurs dopés Zr, le zirconium perturbe les spinelles Co_3O_4, formant des espèces Co-O-Zr et conduisant à des tailles de grains Co_3O_4 plus petites, à une surface spécifique plus grande, à une meilleure réductibilité, à des concentrations de Co^{2+} en surface plus élevées et à plus de lacunes en oxygène de surface et d'espèces réactives en oxygène. Les meilleures propriétés catalytiques d'oxydation du propane ont été obtenues sur un catalyseur Zr- Co_3O_4 à 1%, principalement grâce à son excellente réductibilité à basse température et à l'abondance d'espèces réactives d'oxygène en surface. L'oxydation du propane sur un catalyseur Zr- Co_3O_4 à 1% est conforme au mécanisme de mars-van krevilen, sur la base d'un spectre de transformée de Fourier infrarouge en réflexion diffuse.

L'effet d'un dopage modéré au niobium (teneur en Nb ≤ 1.5mol.%) sur les propriétés catalytiques du Co_3O_4 a été étudié à partir des résultats expérimentaux obtenus avec un catalyseur Co_3O_4 moyennement dopé au Zr. Les catalyseurs synthétisés par la méthode sol-gel sont utilisés respectivement pour l'oxydation catalytique du propane et du VC. Les résultats montrent que les catalyseurs Nb-Co_3O_4 à 1% présentent les meilleures propriétés catalytiques pour l'oxydation du propane ou du VC, où le type de sous-produit polychloré de l'oxydation du VC est nettement réduit. Le dopage au Nb permet d'améliorer la réductibilité et l'acidité de surface du catalyseur Co_3O_4, d'augmenter la teneur en Co^{2+} de surface, en lacunes d'oxygène et en oxygène actif, et donc d'augmenter l'activité catalytique du catalyseur Co_3O_4. En présence d'eau dans le gaz d'alimentation, le catalyseur Nb-Co_3O_4 à 1% permet essentiellement de conserver son activité catalytique sur l'oxydation du VC sans formation de Cl_2 dans le produit final. Il peut présenter de bonnes performances dans les tests de stabilité pour l'oxydation du propane ou du VC.

Des catalyseurs Co_3O_4 à différentes teneurs résiduelles en sodium ont été préparés par précipitation. Le sodium résiduel peut être partiellement inséré dans le réseau de Co_3O_4, provoquant des distorsions et augmentant la surface spécifique du catalyseur. Dans le même temps, il peut affecter négativement la réductibilité et la mobilité de l'oxygène du catalyseur, inhibant l'activité catalytique du catalyseur Co_3O_4 sur l'oxydation du propane.

Mots clés: Les composés organiques volatils; Catalyseur à base de Co_3O_4; Oxydation catalytique; Chlorure de vinyle; Propane

Contents

Chapter 1 Introduction

1.1 Brief introduction of volatile organic compounds (VOCs)

In the comprehensive emission standard of air pollutants, VOCs generally refer to organic compounds involved in the atmospheric photochemical reactions, or those determined by measurement or accounting according to specified methods [1]. These organic compounds are widely used in industry, agriculture and medicine due to their volatile properties and excellent solubility. Based on the different chemical composition, VOCs can be divided into non-methane hydrocarbons, oxygen-containing organic compounds, halogenated hydrocarbons, organic compounds containing nitrogen, organic compounds containing sulfur, and other categories.

The sources of VOCs are mainly natural sources and human activities. Natural sources mainly include animal and plant emissions, volcanic activity, and other geochemical processes. This kind of VOCs source is relatively less harmful to the environment. With the rapid development of society and economy, human activities are also gradually increasing, including fossil fuel combustion, transportation, industrial process, the use of organic solvents, building and decoration materials, etc. The range of this kind of VOCs sources is very wide, being bigger threats to the environment and human health. Taking China's VOCs emissions in 2015 as an example (Fig. 1.1), it can be seen that anthropogenic sources from transportation and industrial processes account for more than 70% [2].

Fig. 1.1 VOCs emission from different sources in China in 2015 [2].

Due to the toxicity and carcinogenicity of VOCs, most VOCs can cause harm to the environment, such as VOCs can participate in the photochemical reaction by reacting with nitrogen oxides and hydrocarbons in the atmosphere. It will generate photochemical smoke, cause damage to the ozone layer, and increase the amount of ultraviolet radiation reaching the

Earth's surface, etc. At the same time, long-term exposure to VOCs will also seriously do harm to human life and health. They will stimulate the eyes and respiratory tract, causing headaches, sore throat, fatigue, and other symptoms. Some of the carcinogenic VOCs will cause irreversible damage to human health [3-5]. With the increasing intensification of environmental pollution, countries around the world have also developed increasingly strict standards for VOCs emissions. Therefore, the development of various efficient and low-cost VOCs purification methods has become a research hotspot and challenge in recent years.

1.2 Abatement methods of VOCs

Researchers have been studying the purification of VOCs for a long time, and some methods have been developed. Due to the different types, concentrations, and emission methods of VOCs, various purification methods also have their own characteristics. At present, there are two main ways to purify VOCs. One is the physical method for the purpose of recycling VOCs, the other is the chemical method for the purpose of degrading VOCs. Physical methods are generally suitable for VOCs with high concentration and high value, while chemical methods are more useful for VOCs with low concentration and low value. As shown in Fig. 1.2, the physical methods mainly include adsorption, absorption, condensation deposition, and membrane separation method, etc., while the chemical methods include direct incineration, biodegradation, photocatalytic oxidation, plasma technology, and catalytic oxidation method, etc.

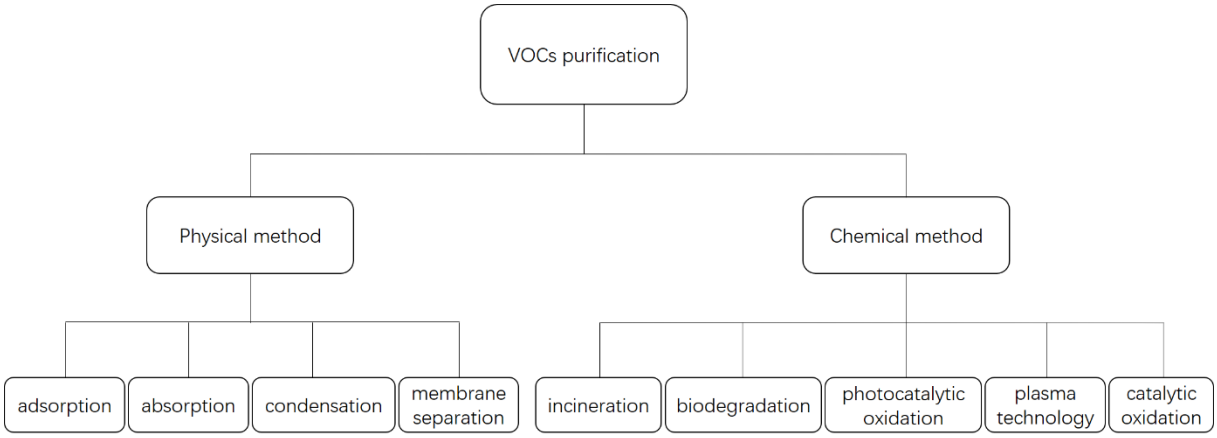

Fig. 1.2. Common techniques for VOCs purification.

1.2.1 Physical method

The adsorption method [6-7] uses adsorbents to adsorb and purify VOCs, and then the purified gas is discharged into the atmosphere. At present, the commonly used adsorbents are granular activated carbon, activated carbon fiber, molecular sieves, activated alumina, silica gel, multi-empty clay ore, and polymer adsorption resin. Activated carbon is currently the most

widely used adsorbent, mainly being used in the recovery of organic solvents. The adsorption method is more effective for the treatment of low concentration VOCs, but the cost of different adsorbents is different, and the higher cost of adsorbents will limit their use in industry to a certain extent. The absorption method [8] is widely used in the purification of high-concentration soluble VOCs, but it has high requirements on the solubility of VOCs and the cost of solvents.

The condensation method [9] mainly condenses VOCs in the gas at low temperature and achieves the purpose of separation through the condenser. This method is more suitable for high concentration VOCs. It is simple to operate, and the removal rate of VOCs is also high. However, the condensed VOCs need to be further purified, so it is often combined with other chemical methods to achieve the complete purification effect of VOCs. Membrane separation [10] is a new method for the treatment of high concentration VOCs. This method also has advantages of high VOCs purification rate, easy operation, and no secondary pollutants. However, the high cost, low membrane stability, and short life limit its application in the industrial. More research is needed to improve it and solve these problems.

1.2.2 Chemical method

Direct incineration [11] is a common method for industrial treatment of VOCs. It is also an effective means for purification of VOCs. But this method is a relatively backward technology. The required temperature of the total combustion of VOCs is too high. It is usually difficult to achieve complete combustion under the common condition, which is easy to produce secondary pollution in the process of burning pests, such as carbon monoxide, formaldehyde, etc. The high combustion temperature also makes the energy consumption very big, making it very uneconomical in the process of practical application.

The biodegradation method [12] uses VOCs as energy or nutrients needed for microbial life activities. It can degrade VOCs into simple inorganic substances or components of microorganisms through metabolism in microbial life activities. This method is a new method. It performs well when treating low concentration and easily degradable VOCs, with no secondary pollution in the purification process. Thus, it has a broad application prospect. However, this method has a poor purification effect for the VOCs containing complex components or VOCs with high degradation difficulty.

Photocatalytic oxidation [13] is a deep oxidation process, in which the specific light source and catalysts are combined to treat VOCs. The method has a strong ability to purify VOCs, and the degradation of pollutants is relatively thorough. At the same time, the operating conditions are mild. It can usually be carried out under normal temperature and pressure. However, in the current research status, the reaction speed of photocatalytic oxidation is slow, which is not conducive to the purification of VOCs in the industrial, which limits its practical application.

Plasma technology [14], as a highly efficient treatment method for VOCs purification, has the advantage of low energy consumption in the meantime. However, due to its non-selectivity, this method will lead to the generation of harmful by-products, such as ozone and nitrogen oxides, so it is not widely used in practice.

The catalytic oxidation method [15-20] is similar to the direct incineration method, in which VOCs react with oxygen to achieve the effect of degradation and purification of VOCs. However, the difference is the introduction of a specific catalyst in the process of catalytic oxidation, which can make the reaction between VOCs and oxygen occur at a lower temperature. Under the conditions of high treatment capacity and low VOCs concentration, the required temperature of the method can usually be lower of 300-500 ℃ than that of the direct incineration, and the catalytic oxidation can make VOCs be completely oxidized, without the production of CO and other combustible gases. The oxidation process is also not easy to generate secondary pollution byproducts, such as dioxins, nitrogen oxides. Furthermore, this method has the advantages of high efficiency of VOCs removal and heat recovery in the reaction process. Fig. 1.3 shows the difference of the activation energy in the process of VOCs oxidation with or without the presence of the catalyst. With the presence of the catalyst, the Gibbs free energy of the VOCs oxidation does not change, but the activation energy is significantly reduced [21].

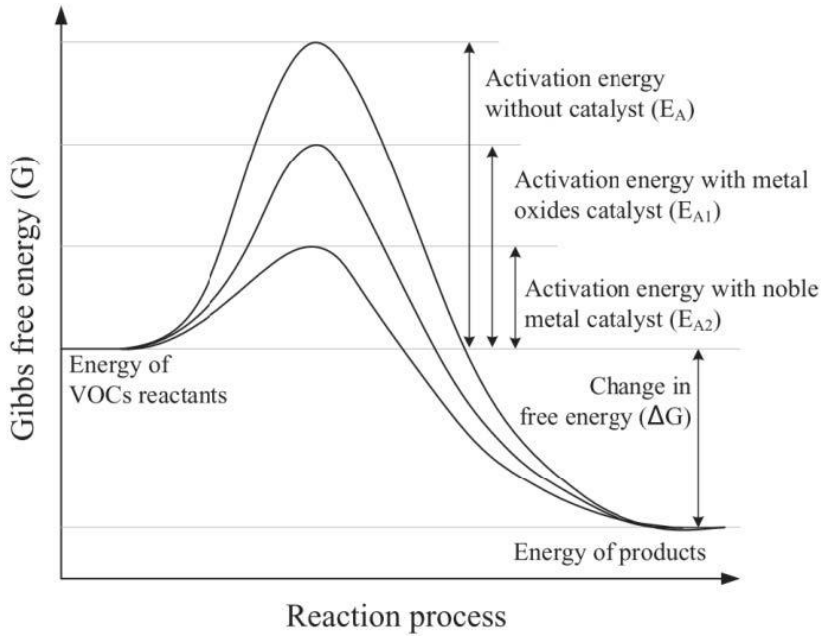

Fig. 1.3. Energy profile diagram of VOCs oxidation reaction with and without catalyst [21].

In the practical application, sometimes several methods will be combined to improve the purification efficiency. For example, for some low concentration VOCs, they can be enriched by physical methods, and then degraded and purified by chemical methods. Among the various ways of chemical degradation of VOCs, the catalytic oxidation method shows strong

elimination ability with low operating temperature and low energy consumption. The main advantage of this method is that the operating temperature is lower than that of the direct combustion method (< 500 ° C) and can deal with lower concentration (< 1%) of VOCs exhaust gas. At present, it has also become a relatively mature technology for VOCs abatement in industrial production [22-28]. Catalytic oxidation is also considered to be one of the most feasible, promising, and suitable methods for industrial VOCs elimination. For the catalytic oxidation process, the most critical problem is to develop catalysts with low ignition temperature, high catalytic activity, strong stability, and low price.

1.3 Current research on catalytic oxidation of VOCs

Researchers have studied the catalytic oxidation of VOCs for several decades, mainly focusing on noble metal catalysts and transition metal oxide catalysts. Particularly, the molecular sieve catalysts also show high catalytic activity for the catalytic oxidation of chlorinated volatile organic compounds (CVOCs).

1.3.1 Noble metal catalysts

Noble metal catalysts have been extensively studied because of their excellent catalytic activity and high value in industrial applications. Common noble metal catalysts mainly include Pt, Pb, Ru, Au, and Rh, etc. These noble metals are usually supported on a specific carrier to form a supported noble metal catalyst to participate in the catalytic oxidation of VOCs [29-33].

It is well known that the two most important factors affecting the activity of noble metal catalysts are the loading amount and dispersion of noble metal. Generally speaking, there exists an optimal loading amount. When the loading amount of noble metal is in a certain range, the catalytic activity would correlate with the amount of well-dispersed noble metals. However, when the amount of noble metal is more than the optimal value, the catalytic activity would not show obvious improvement. Considering the reason for this phenomenon, metal particles would easily gather on the surface of the carrier, reducing the degree of dispersion and the number of active sites on the catalyst surface. Masui et al. [34-35] prepared a series of Pt/CeO_2-ZrO_2-Bi_2O_3/γ-Al_2O_3 (Pt/CZB/Al_2O_3) catalysts with different Pt loading (5, 7, and 9 wt.%) and applied them in the catalytic oxidation of toluene. It was found that the addition of Pt promoted the oxygen mobility on the surface of the catalysts, which increased the catalytic reaction rate and catalyst activity. In addition, no carbon monoxide and other toluene-related by-products were produced in the whole reaction. At the same time, they also found that the addition of polyvinylpyrrolidone (PVP) in the preparation process of the catalysts can effectively promote the dispersion of Pt on the surface of the support and enhanced the catalytic activity of the catalysts. In particular, 7%Pt/ CZB/Al_2O_3 catalyst with PVP added in the preparation process showed the best catalytic activity for toluene oxidation, and the complete conversion

temperature can be achieved as low as 120 °C (Fig. 1.4). However, when the loading amount of Pt increased to 9 wt.%, the Pt on the surface of the catalyst agglomerated, the dispersion of Pt decreased, and the particle size of Pt became larger. The catalytic activity of the catalyst decreased correspondingly.

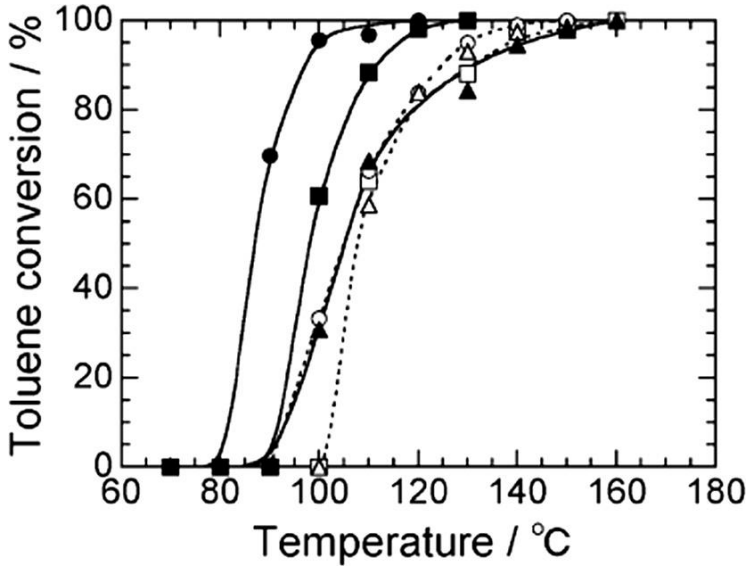

Fig. 1.4 Temperature dependence of the toluene oxidation on 5%Pt/CZB/Al_2O_3 (□, ■), 7%Pt/CZB/Al_2O_3 (○, ●), and 9%Pt/CZB/Al_2O_3 (△, ▲). Open and closed symbols correspond to the data for the catalysts prepared in the absence and presence of PVP, respectively [35].

For specific VOCs, the choice of appropriate noble metals and carriers is crucial in the design and preparation of the catalysts. The synergistic interaction between noble metals and carriers contributes to achieving the optimal catalytic activity. One strategy is to load different kinds of noble metals with the same content on the same carrier respectively, so as to investigate the different performance of different noble metals for VOCs oxidation. Recently, Zhang and He et al. [36-38] made a breakthrough in the study of complete oxidation of formaldehyde at room temperature. They prepared the 1 wt.% Pt/TiO_2 catalyst by a simple impregnation method. The catalyst can completely oxidize formaldehyde to carbon dioxide and water at room temperature without any by-products, which indicates that titanium dioxide can be used as a carrier for formaldehyde oxidation at room temperature in practical applications. In subsequent studies, they compared the catalytic activities of formaldehyde oxidation using titanium dioxide as the support for different noble metal catalysts. The results showed that the activity of Pt/TiO_2 catalyst is much higher than other titanium dioxide supported noble metal catalysts. The catalytic activity order was as follows: Pt/TiO_2 > > Rh/TiO_2 > Pd/TiO_2 > Au/TiO_2 > > TiO_2 (Fig. 1.5). Subsequently, they proposed a simple reaction mechanism for formaldehyde oxidation on these TiO_2 supported noble metal catalysts through the diffuse reflectance infrared Fourier transform spectroscopy experiments. It showed that formate and carbon monoxide are the main intermediate species during the whole process. The reason for the different activity of

these noble metal catalysts was the ability of formate formation and the conversion of surface formate to adsorbed CO. The latter one was the rate-determining step for the catalytic oxidation of HCHO over the catalysts.

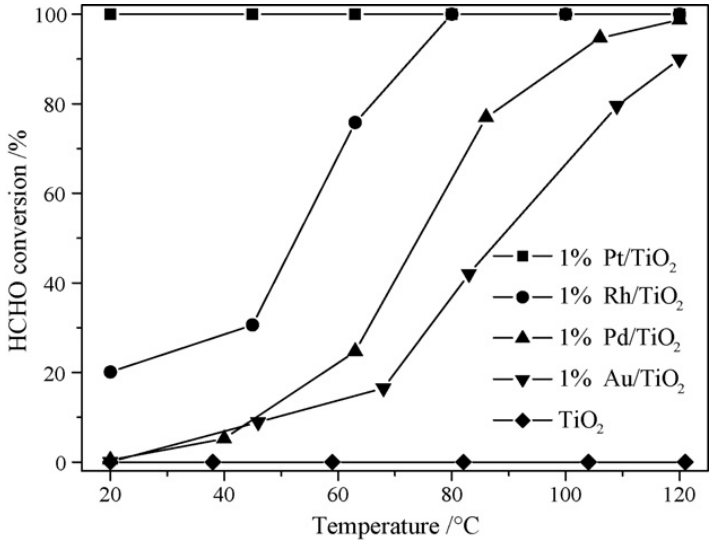

Fig. 1.5 HCHO conversions over TiO_2 supported noble catalysts at various temperatures. Reaction conditions: HCHO 100 ppm, O_2 20 vol.%, He balance, total flow rate 50 cm^3 min^{-1}, GHSV: 50,000 h^{-1} [37].

The synergistic interaction between the noble metals and supports are also studied by loading the same noble metals on different supports. Ousmane et al. [39] prepared a series of catalysts (Au/CeO_2, Au/TiO_2, Au/Al_2O_3, $Au/7.5Ce/Al_2O_3$) by deposition-precipitation method, with 1.5 wt.% of Au supported on different oxide carriers, and applied them in the study of low temperature oxidation of propylene and toluene. It was found that the best catalytic activity for propylene and toluene oxidation was achieved on Au/CeO_2, followed by Au/TiO_2, and Au/Al_2O_3 performed worst. However, when a small amount of Ce (7.5wt. %) was introduced into Al_2O_3, the activity of $Au/7.5Ce/Al_2O_3$ was significantly improved, even higher than that of Au/TiO_2, but still lower than that of Au/CeO_2 (Fig. 1.6). The characterization results of the catalysts showed that the high activity of Au/CeO_2 may be due to the following factors. First of all, CeO_2 has a good capacity of oxygen storage and release. It can also stabilize Au nanoparticles so that they will not be sintered during the preparation of the catalyst. Secondly, the strong interaction between Au nanoparticles and the carrier through the formation of oxygen vacancies resulted in the formation of Au-O structure at the interface, which promoted the improvement of the catalytic activity. Finally, they found that there was no deactivation of the catalyst after three catalytic cycles, and that the gold particles existed in the form of Au^0, suggesting the role of metallic Au (in close contact with Ce) in the oxidation of propylene and toluene. The activity of Au/TiO_2 may be due to the interface formed between the highly dispersed Au nanoparticles and the TiO_2 carrier, which was conducive to oxygen dissociation and activation. However, the weak interaction between Au and the un-reduceable Al_2O_3 support

led to the large size of gold particles on Au/Al_2O_3 catalyst, which resulted in the poor catalytic activity and stability. The increased activity of $Au/7.5Ce/Al_2O_3$ may be due to that the existence of oxygen vacancies on Ce can fix Au particles, resulting in the stronger interaction between Au particles and the carrier, and the smaller size of Au particles. Moreover, the presence of oxygen vacancies can also promote the oxygen mobility, thus enhancing the catalytic activity of propylene and toluene oxidation at low temperature.

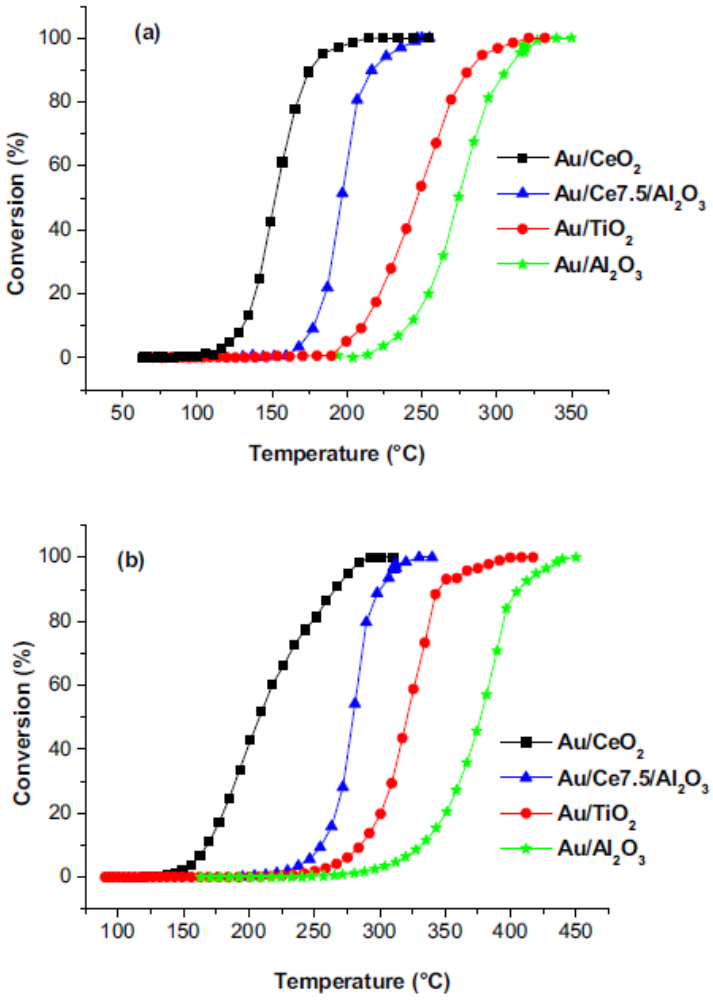

Fig. 1.6 Conversion of (a) propene and (b) toluene versus temperature over gold supported catalyst (third catalytic run) [39].

For the catalytic oxidation of CVOCs, the noble metal Ru is generally considered as a very potential catalyst [40-43]. Wang et al. [44] prepared supported and doped Ru-based catalysts by two methods, impregnation and one-step sol-gel method, respectively. They compared the difference of the activity of the two catalysts for the catalytic combustion of vinyl chloride (VC). The substrate used in both catalysts is cobalt trioxide. It was found that, compared with Co_3O_4 catalyst, the catalytic activity of both supported and doped catalysts was significantly improved, and the supported Ru based catalyst had higher activity. The physicochemical properties of the

catalysts showed that the Ru species mainly affected the redox performance of the substrate Co_3O_4, and thus played a key role in the catalytic oxidation of VC. The improvement of the redox performance of the substrate was mainly due to the high dispersion of Ru on the surface of Co_3O_4 and the obvious increase of Ru^{4+} content on the surface. More importantly, part of Co^{3+} on the surface of Co_3O_4 was replaced by Ru^{4+}, which resulted in a relative increase of surface Co^{2+} content. The increase of Co^{2+} generally indicated the increase of oxygen defects on the surface of the catalyst, which would eventually lead to the easier formation of surface active oxygen species and improve the catalytic activity of supported Ru-based catalyst for the oxidation of VC.

A patent (CN107233882A) discloses a preparation method and application of a Ru/SnO_2 catalyst for the catalytic combustion of vinyl chloride [45]. The invention uses impregnation method to load $Rucl_3$ on a SnO_2 carrier, in which the SnO_2 carrier is prepared by a simple ammonia precipitation method. The Ru-based catalyst obtained by the invention can completely oxidize VC to carbon dioxide, water, hydrogen chloride or chlorine at low temperatures, with no toxic polychlorinated by-products in the reaction process. The hydrogen chloride or chlorine in the tail gas can be adsorbed by alkali liquor to meet the emissions standards, and also to prevent the secondary pollution. The role of noble metal Ru in the invention is mainly removing the adsorbed Cl species on the surface of the catalyst in time through the Deacon reaction, so that the catalyst can maintain its activity, selectivity and stability without being poisoned. The invention has great practical application value because the preparation method used in the invention is impregnation, which is simple and feasible in industry, and the catalyst has high activity and good stability.

The advantage of noble metal catalyst is that VOCs ignition temperature and the complete oxidation temperature are relatively low. The catalytic activity of them is high. And there is basically no by-product generated on them. However, noble metals are expensive, and easy to aggregate and be deactivated under high temperature. Notably, they are easy to be poisoned by chlorine for CVOCs oxidation. All of these disadvantages have negative effects on the application of the noble metal catalysts. Therefore, the research of noble metal catalysts is still focused on reducing the loading amount, improving the dispersion, and enhancing the stability and the poisoning-resistant ability.

1.3.2 Transition metal oxide catalysts

Although noble metal catalysts have high catalytic activity for VOCs oxidation, their high price and poor availability limit their practical application. Recent studies have found that transition metal oxide catalysts also have relatively good catalytic activity for VOCs oxidation. Their easy availability and low cost make them a potential substitute for noble metal catalysts. In addition to lower cost, transition metal oxide catalysts also have some other advantages, such

as strong stability, strong regeneration ability, etc. Thus, researchers have also carried out a lot of studies on the efficient transition metal oxide catalysts for VOCs oxidation in recent years.

Transition metal oxide catalysts can participate in VOCs oxidation in the form of a single oxide [46-55]. Ma et al. [56] prepared a nanocrystalline rod-like Co_3O_4 catalyst for the catalytic oxidation of propane and compared its catalytic activity with that of supported noble metal catalyst Pt/Al_2O_3. It was found that the catalytic activity of nanocrystalline Co_3O_4 for propane oxidation was much higher than that of Pt/Al_2O_3. Later, they studied the reaction mechanism of propane oxidation on these two catalysts in detail, so as to explain the reason for the difference in the activity of the two catalysts. Kinetic data showed that the activation of C-H bond can be considered as the most dynamically related for both catalysts. The propane is first converted to the $C_3H_7O^*$ species. The intermediate products are further dissociated and oxidized to carboxylate. Acetate and formate are the most important intermediate species. Finally, these intermediate species are oxidized to the final products, carbon dioxide and water (Fig. 1.7). For Co_3O_4, propane oxidation follows the L-H (Langmuir-Hinshelwood) mechanism. The rate-determining step is the activation of the C-H bond. The C-H bond is cleaved, and H is adsorbed on the nearby oxygen atom. For Pt/Al_2O_3, the propane oxidation is proceeded according to the E-R (Eley-Ridel) mechanism, and the decisive step is the activation of gaseous propane on the adjacent oxygen atoms and oxygen vacancies on the catalyst surface. In situ infrared results showed that the activation of propane on Pt/Al_2O_3 was limited, which led to its poor activity.

1. $O_2 + * \overset{K_1}{\rightleftharpoons} O_2*$
2. $O_2* + * \overset{K_2}{\rightleftharpoons} 2O*$
3. $C_3H_8 + * \overset{K_3}{\rightleftharpoons} C_3H_8*$
4. $C_3H_8* + O* + O* \xrightarrow{k_4} C_3H_7O* + OH* + *$
5. $C_3H_7O* + 12O* \overset{K_5}{\rightleftharpoons} 3CO_2* + 7OH* + 3*$
6. $CO_2* \overset{K_6}{\rightleftharpoons} CO_2 + *$
7. $OH* + OH* \overset{K_7}{\rightleftharpoons} H_2O* + O*$
8. $H_2O* \overset{K_8}{\rightleftharpoons} H_2O + *$

Fig. 1.7 Proposed elementary steps for propane oxidation over Co_3O_4 nanorods [56].

Wang et al. [57] synthesized the nano-cube and nano-rod CeO_2 catalysts by hydrothermal method and applied them in the catalytic oxidation of o-xylene. It was found that the nanorod CeO_2 catalyst had the highest catalytic activity, even reaching the activity of traditional noble metal catalyst. At the same time, the catalyst also showed good stability, and no deactivation

occurred after 50 hours of stability test. The study of the catalyst structure showed that the nano-rod catalyst, with preferential exposure of (111) and (100) crystal facets, processed the highest amount of oxygen vacancies on the catalyst surface, which promoted the adsorption of molecular oxygen. Further oxygen temperature programmed desorption experiments showed that the desorption temperature of adsorbed oxygen on the surface of nanorods CeO_2 was lowest, confirming the key role of oxygen vacancies in the catalytic oxidation of o-xylene.

Piumetti et al. [58] prepared three kinds of manganese oxide catalysts (Mn_2O_3, Mn_3O_4 and Mn_xO_y) by solution combustion method and applied them in the complete oxidation of ethylene, propylene and mixtures of ethylene and propylene. The best catalytic activity came from the Mn_3O_4 catalyst, which possessed the highest concentration of electrophilic oxygen species on the catalyst surface. Further studies showed that the acid sites on the surface of Mn_3O_4 performed a crucial role in the catalytic reaction, which positively influenced the adsorption of reactants and the desorption rate of products, and also promoted the activation of reactants and intermediates to a certain extent.

Wang et al. [59] studied the cleavage mechanism of C-C bond in ethylene oxidation on Co_3O_4 using density functional theory (Fig. 1.8). Firstly, the adsorbed ethylene molecule removes a hydrogen atom through the help of the neighboring two-coordinated oxygen atom, forming the CH_2CH group at the Co site. CH_2CH reacts with the neighboring three-coordinated oxygen atom to generate CH_2CHO. Then, CH_2CHO is converted into CHCO through two steps of dehydrogenations, which can be oxidized by the oxygen molecule adsorbed at the oxygen vacancy to produce CHOCO. Finally, CHOCO could easily break its C-C bond, producing C_1 species (CO and CHO), which can be oxidized into CO_2. It can be seen that the formation of oxygen-containing groups plays an important role in the cleavage process of C-C bond in ethylene oxidation on Co_3O_4. Further studies showed that the breaking of C-C bond in C_2 species could only be completed when the C valence of the C_1 species reached saturation after the bond cleavage. The pathway for C-C cracking is called the valency-saturation-driven mechanism.

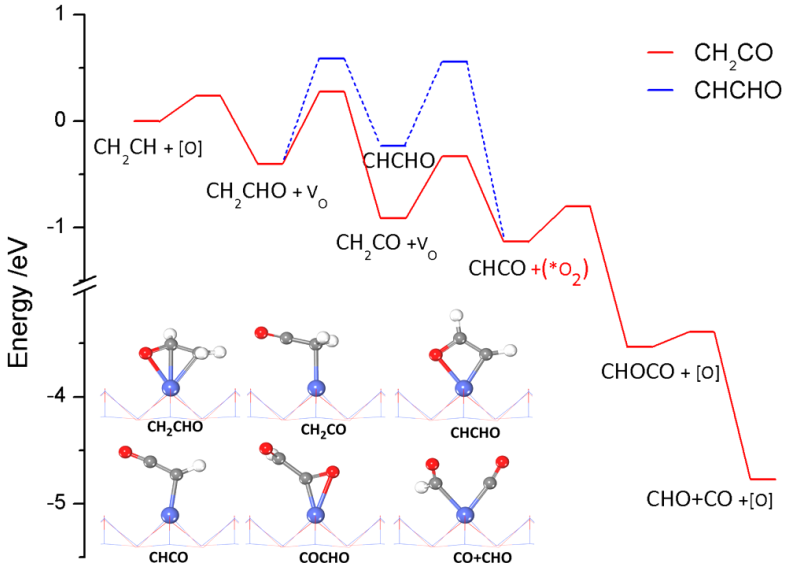

Fig. 1.8 Energy profiles of the conversion from CH_2CH to CHCO following two different oxidation-dehydrogenation pathways, as well as the conversion of CHCO into CO (CHO) through oxidation-cracking mechanism [59].

The researchers found that it can play a role in VOCs oxidation as the form of composite oxides by combing two or more metal oxides [60-75]. Generally speaking, the synergistic effect of the components in composite oxide catalysts can contribute to a better catalytic activity than single oxide. Zhu et al. [76] prepared a series of Co_3O_4-CeO_2 catalysts by combining cobalt tetroxide and cerium dioxide by sol-gel method and used them for the complete oxidation of propane. It was found that $CoCeO_x$-70 had the best catalytic activity. The strong interaction between Co_3O_4 and CeO_2 improved the redox ability and increased the amount of active oxygen species of the catalyst. The interaction is mainly as follows (Equations 1-1 and 1-2): Co_3O_4 can be reduced by the reaction gas to CoO or metal Co, accompanied by the generation of oxygen vacancies. The reduced state of Co can combine with oxygen species on the surrounding CeO_2 and then be oxidized, thus forming a large number of oxygen vacant sites at the interface between Co_3O_4 and CeO_2. These sites can adsorb molecular oxygen and generate a large number of active oxygen species, improving the catalytic activity of the catalyst. They proposed the mechanism of propane oxidation on the catalyst by in situ infrared spectroscopy experiments. Firstly, propane is adsorbed on the catalyst surface. Then it is decomposed into carbonate species, which are further oxidized to form acetone and lipid species. Finally, these C=O species are completely oxidized to carbon dioxide and water. By comparison, they found that the introduction of Ce promoted the adsorption and activation of propane on the catalyst surface during the reaction, rather than changed the reaction mechanism.

$$Co_3O_4 \rightarrow Co^{2+}/Co^{3+} + [O] \rightarrow Co^0 + [O] \quad (1\text{-}1)$$

$$Co^0\ (Co^{2+}) + CeO_2 \rightarrow Co^{2+}/Co^{3+}\ (Co^{3+}) + CeO_{2-x} + [O] \quad (1\text{-}2)$$

Ye et al. [77] prepared two kinds of Cu-Mn composite oxide catalysts by co-precipitation method and reductive precipitation method, respectively, and used them for the catalytic combustion of toluene. The physicochemical properties and catalytic activities of the two catalysts were then compared. Among them, nitrate and tetramethylammonium hydroxide are used as precursor precipitator in co-precipitation method. Manganese acetate and copper nitrate are used as precursors. Potassium permanganate is used as oxidant in reductive precipitation method. The experimental results showed that the catalytic activity of Cu-Mn composite oxide was higher than that of single oxide catalyst, and the catalyst prepared by reduction precipitation method exhibited better performance. The characterization of the catalyst showed that Cu species on the catalyst prepared by the reductive precipitation method had better dispersion when interacting with Mn, exposing more active sites on the catalyst surface. And the catalyst showed a larger specific surface area and a higher content of structural defects (more oxygen vacancies). The oxidation reaction without oxygen showed that the surface adsorbed oxygen played an important role in the catalytic activity. For the stability test, all the catalysts were deactivated to some extent when they did not reach the stable state in the reaction. The introduction of trace noble metal platinum into the catalysts prepared by the reductive precipitation method could enhance the stability of the catalysts, even though it could not improve the activity of the catalysts.

Recently a Mn-Ti composite oxide catalyst was reported for the catalytic oxidation of VC [78]. It was found that the Mn-O-Ti solid solution was formed in Mn-Ti composite oxides because Ti^{4+} and Mn^{4+} have similar ionic radii. Compared with TiO_2, there are a lot of defective sites on $MnyTi_{1-y}O_x$, so the surface acidity of the catalyst is strengthened. Among them, $Mn_{0.4}Ti_{0.6}O_x$ had the highest content of surface acid sites. By studying the relationship between surface acidity, reducibility and catalytic activity of the catalyst, it was proved that surface acidity played a key role in the complete oxidation of VC, mainly Lewis acid exhibited by the Ti species. The surface acidity promoted the adsorption and dissociation of VC on the catalyst surface by interacting with π electrons in VC. According to the experimental results, the reaction mechanism of complete oxidation of VC on the catalyst was proposed (Fig. 1.9). First, VC is adsorbed on the surface of the catalyst through the binding of C=C and Ti^{4+}. Secondly, the surface acid sites of the catalyst can help the C-Cl bond break, allowing the desorption of Cl from the catalyst surface in the form of HCl. The surface active oxygen species then oxidize the C_2H_3 groups into carbon dioxide and water. Finally, the oxygen vacancies formed on the surface are replenished by adsorption and dissociation of gaseous oxygen. It can be seen that the surface acidity and reducibility of the catalyst are essential in this process. This study can provide an effective strategy for coordinating the reducibility and surface acidity of the catalyst to improve the catalytic performance.

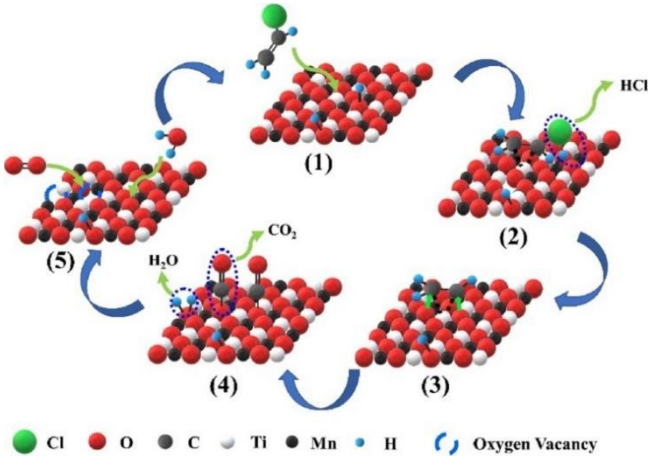

Fig. 1.9 Mechanism of deep oxidation of VC over the $Mn_yTi_{1-y}O_x$ catalysts [78].

Transition metal oxides can also be supported on a specific carrier to form a supported transition metal oxide catalyst to participate in VOCs catalytic oxidation reaction [79-88]. Cao et al. [89] studied the catalytic combustion of dichloromethanes with a novel two-bed catalyst (Ce/TiO_2-Cu/CeO_2). In the experiment, they also prepared three other catalysts as comparisons, namely Cu/CeO_2, Ce/TiO_2 and $(Ce+Cu)/TiO_2$. The experimental results showed that the catalytic activity of Cu/CeO_2 was particularly poor, with only 47.0% dichloromethane conversion at 375 °C. The activity of $(Ce+Cu)/TiO_2$ was higher than that of Cu/CeO_2, and the conversion of dichloromethane can reach 99.0% at 375 °C. The catalytic activities of Ce/TiO_2 and Ce/TiO_2-Cu/CeO_2 were similar, and the dichloromethane can be completely converted at 335 °C on them. However, when analyzing the by-products of the complete conversion of dichloromethane on these catalysts, they found that the content of by-products over Ce/TiO_2, $(Ce+Cu)/TiO_2$ and Ce/TiO_2-Cu/CeO_2 decreased in turn to 10.6%, 3.0% and 1.0%, respectively, indicating that Cu species can enhance the decomposition of by-products. More importantly, they found that the CO_2 concentration in the final products of dichloromethane oxidation on the catalysts containing Cu (71.0% for $(Ce+Cu)/TiO_2$、96.0% for Ce/TiO_2-Cu/CeO_2 and 97.0% for Cu/CeO_2) were much higher than that on Ce/TiO_2 (only 7.2%), suggesting the importance of Cu specie in the conversion of CO to CO_2. The result of the stability tests showed that Ce/TiO_2-Cu/CeO_2 effectively maintained the advantages of Ce/TiO_2 and $(Ce+Cu)/TiO_2$ (Fig. 1.10), which could keep the dichloromethane conversion stable and maintain the dominance of carbon dioxide in the final products. The excellent stability also suggested the new two-bed catalyst can basically get rid of the problem of chlorine poisoning. Through the study of the reaction mechanism by in situ infrared spectroscopy, they proposed the three steps for the catalytic oxidation of dichloromethane on the catalyst (Fig. 1.11). The first step is the adsorption of reactants on the surface of TiO_2 and the breaking of the C-Cl bond, generating some intermediate species. The second step is the removal of the chlorine species and the breaking of C-H bond in the by-products, which is assisted by CeO_2. The lase step is the oxidation of CO

to CO_2, in which CuO plays an important role due to its excellent redox ability. With the increase of the reaction time, the strong adsorption ability of CuO to Cl species on (Ce+Cu)/TiO_2 resulted in the poisoning of the catalyst and the decrease of the catalytic activity. However, the design of the two-bed catalyst Ce/TiO_2-Cu/CeO_2 greatly improved the anti-poisoning ability of the catalyst and helped maintain its excellent stability.

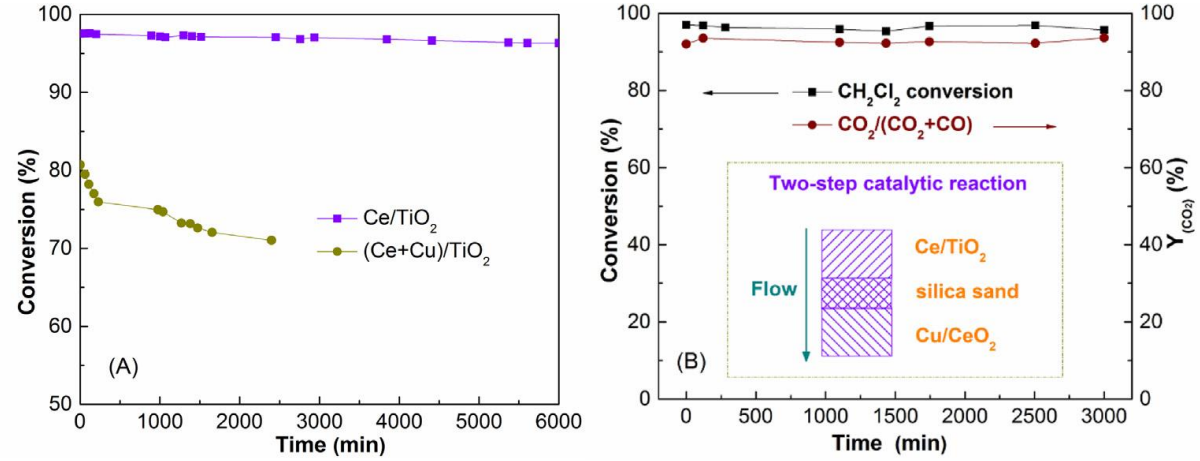

Fig. 1.10 Stability test of Ce/TiO_2, (Ce+Cu)/TiO_2 and Ce/TiO_2-Cu/CeO_2 catalysts at 330 ºC [89].

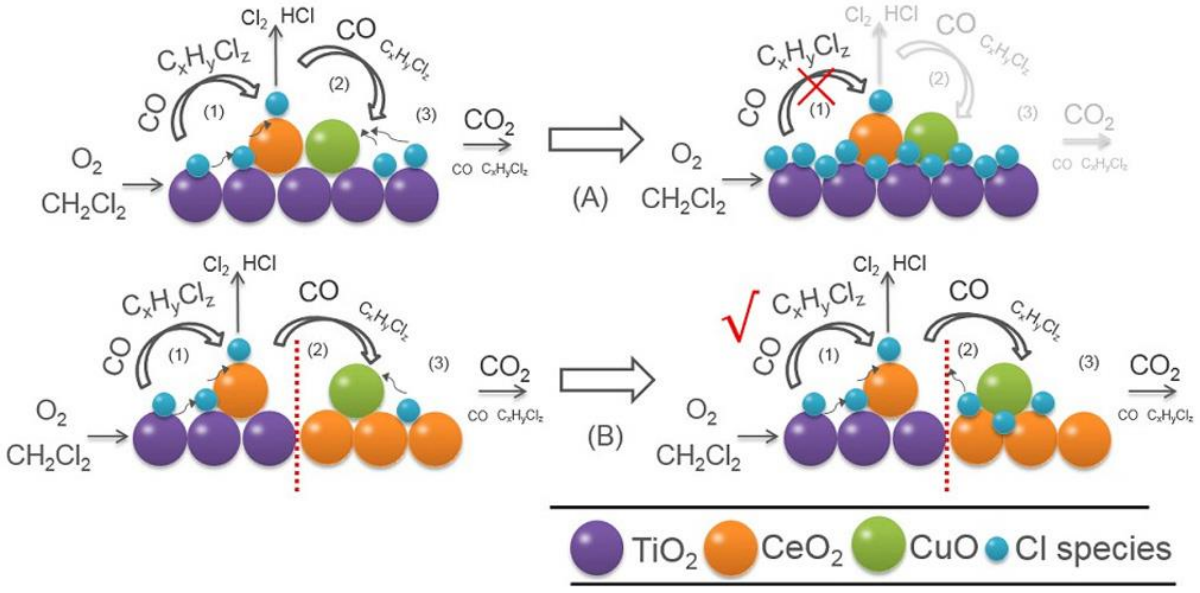

Fig. 1.11 Proposed three-step decomposition mechanisms for the catalytic combustion of DCM on (Ce+Cu)/TiO_2 (A) and Ce/TiO_2-Cu/CeO_2 (B) catalysts. ((1) The first step on the TiO_2 support; (2) the second step on the ceria; (3) the third step on the copper oxides) [89].

Zhu et al. [90] obtained a series of Co_3O_4/ZSM-5 catalysts by supporting Co_3O_4 on ZSM-5 support through different preparation methods and investigated the catalytic activity of these catalysts for propane oxidation. It was found that the different preparation methods had crucial effects on the catalytic activity of the catalysts. The highest activity was achieved on the catalyst prepared by the hydrothermal method. And the study on the relationship of the structure-performance of the catalysts showed that this catalyst had the best reducibility, the highest

amount of surface Co^{3+} and surface lattice oxygen species, and the best oxygen mobility. Propane oxidation over Co_3O_4/ZSM-5 follows the Mars-van Krevelen mechanism. The long-term stability test of propane oxidation on the synthesized catalyst showed good durability, suggesting the potential of the catalyst in the practical application.

Liu et al. [91] reported a deposition-precipitation method for the preparation of a Mn-based catalyst supported on diatomite, which was used for the catalytic oxidation of toluene. The structure characterization of the catalyst showed that the Mn species mainly existed in the form of amorphous MnO_2 and Mn_2O_3, and they were successfully supported on the surface and pores of diatomite (Fig. 1.12). The results of toluene oxidation experiments showed that the Mn-based catalyst supported on diatomite exhibited excellent activity for toluene oxidation, and the selectivity of CO_2 in the products was very high. The catalytic activity of the catalysts correlated well with the content of Mn. Moreover, the catalyst still maintained its high activity for toluene oxidation after one week of use, indicating its good stability. The study on the reaction mechanism showed that the catalytic oxidation of toluene on the catalyst followed the Mars-van Krevelen mechanism. With the increase of Mn content, the surface oxygen species increased, and the adsorption-reaction sites on the catalyst surface also increased. The activity of the catalyst was thus enhanced. Mn^{4+} played an important role in the catalytic oxidation of toluene. Its excellent reducibility promoted the catalytic activity.

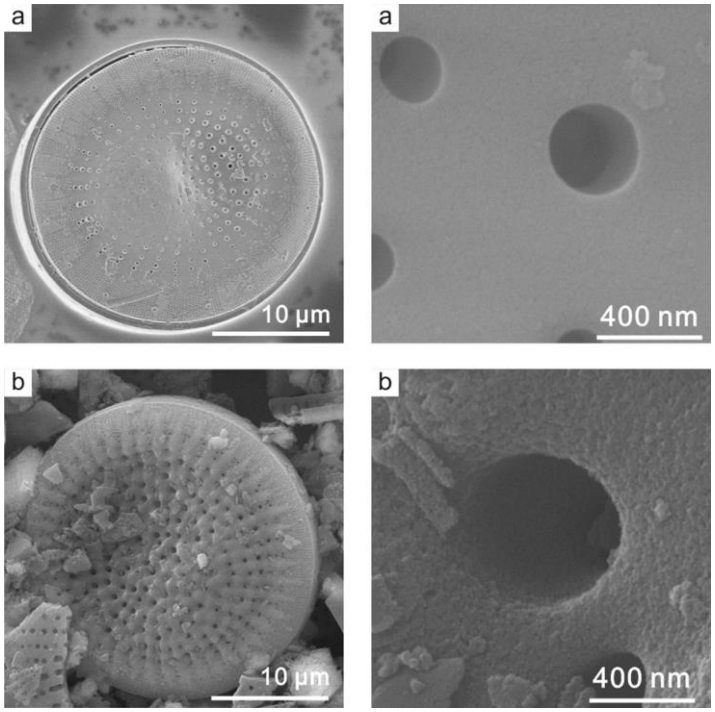

Fig. 1.12 The SEM images for (a) calcined diatomite and (b) the catalyst of Mn14.1-400 [91].

Under specific conditions, transition metal oxides can form perovskite-type catalysts in the preparation process. Due to the high calcination temperature, this kind of catalyst usually has very good thermal stability, so it has also received certain attention in the catalytic oxidation

of VOCs [92-98]. Zhu et al. [99] investigated the catalytic effect of cobalt-substituted $LaMnO_3$ perovskite type catalysts ($LaCo_xMn_{1-x}O_3$) on the complete oxidation of propane. Through the characterization of the catalysts, they found that a small amount of Co replacing Mn could increase the specific surface area of the $LaMnO_3$ perovskite type catalysts, produce a large number of active oxygen species, improve the reducibility of the catalysts, and finally promote its catalytic activity for propane oxidation. The results of in situ infrared spectroscopy and temperature programmed surface reactions of propane oxidation showed that the adsorption and activation of propane on the catalyst surface were accelerated by the substitution of Mn with appropriate amount of Co. The intermediate species of the reaction were mainly acetone and carboxylate species. The specific reaction mechanism is as follows: First, gaseous propane diffuses on the catalyst surface and adsorbs on the active site to form chemical adsorption C_3H_{8-n}, and gaseous oxygen is adsorbed on the catalyst surface and activated into active oxygen species. Then the C_3H_{8-n} species reacts with the active oxygen species, causing the C-C and C-H bonds to break and generating intermediate species such as esters, acetone, carboxylate and so on. Eventually, these adsorbed intermediate species are decomposed and oxidized, and desorbed from the catalyst surface in the form of carbon dioxide and water (Fig. 1.13).

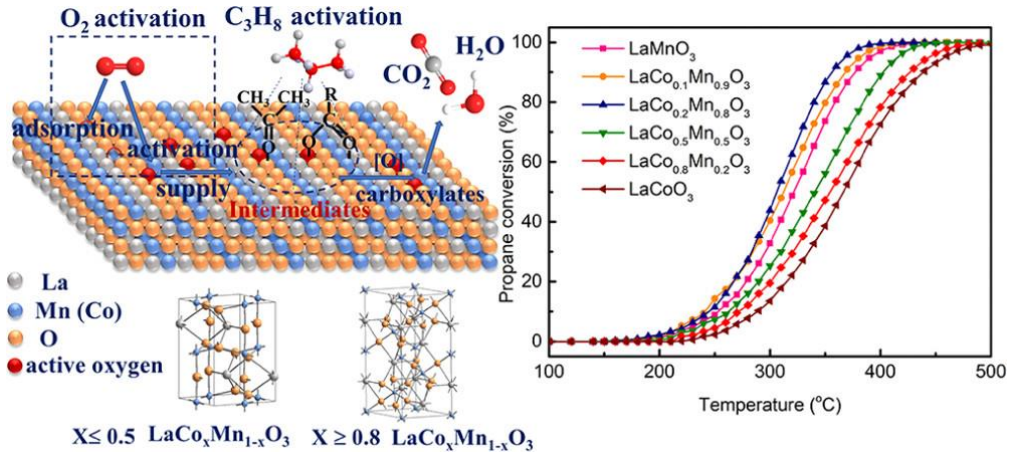

Fig. 1.13 Proposed reaction mechanism of propane oxidation on $LaCo_xMn_{1-x}O_3$ catalysts [99].

Chen et Al. [100] prepared a series of aluminum-substituted $La_{1-x}Al_xMnO_3$ (x = 0-0.3) catalysts by sol-gel method. The effects of Al doping and different heat treatments on the structure of the catalysts and the catalytic oxidation reaction of 1,2-dichloroethane over the catalysts were investigated. It was found that these two factors had a great influence on the catalytic activity. The best catalyst for the catalytic oxidation of 1,2-dichloroethane was $La_{0.8}Al_{0.2}MnO_3$ calcined at 700 °C, and the temperature needed to achieve 50% conversion was 295 °C. The enhanced activity was due to the synergistic effect of high specific surface area, high reducibility and strong surface acidity. Reducibility can play a role in the activation of oxygen, and surface acidity can promote the chemisorption of reactants. Among them, the reducibility of catalyst played a major role in the catalytic activity. Since the A site in

perovskite-type catalysts is generally inactive, A-site doping works primarily by affecting the oxidation state at the B site or by creating non-stoichiometric oxygen. The Al here is therefore considered as the structural additive of the catalyst, affecting the properties of the active manganese species and active oxygen species in the catalyst.

1.3.3 molecular sieve catalysts

For the catalytic oxidation of CVOCs, molecular sieves are widely concerned by researchers due to their extensive acidity and large specific surface area [101-103]. Lopez-Fonseca et al. [104] compared the catalytic oxidation performance of 1, 2-dichloroethane over three H-type molecular sieves (H-Y, H-ZSM-5, and H-MOR). The results showed that all the three molecular sieves showed good catalytic activity in the order of H-ZSM-5 > H-MOR > H-Y. The results of ammonia temperature-programmed desorption and pyridine adsorption experiments showed that the strong Brønsted acid site on the catalyst surface played an important role in the catalytic oxidation process. In situ infrared spectroscopy experiments showed that the adsorption of 1,2-dichloroethane on the surface of H-ZSM-5 by reacting with Brønsted acid site was the first step of the catalytic reaction. The intermediate product of the reaction process was vinyl chloride. Analysis of the complete oxidation products showed that the selectivity of carbon monoxide over all three molecular sieves was very high, indicating that these catalysts had low oxidation capacity. While the selectivity of hydrogen chloride in the products was very high (> 90%). They also investigated the effect of water on the activity of the catalysts and found that the addition of water inhibited the activity of the catalysts, but water also significantly affected the selectivity of the complete oxidation products. When water was introduced, the content of the intermediate product of vinyl chloride was greatly reduced, while the selectivity of carbon dioxide in the final product was significantly enhanced. The characterization of the deactivated sample showed that it was due to the partial collapse of the crystal structure of the molecular sieve.

The catalytic activity of molecular sieve catalysts mainly comes from the promotion effect of the large amounts of surface acid sites on the activation of C-Cl bond. However, the oxidation ability of molecular sieve catalysts is relatively weak, resulting in the large amounts of carbon monoxide presented in the products and the widespread problem of carbon deposition. Moreover, the enrichment of Cl on the catalyst surface could cause the deactivation of the catalyst. Therefore, the molecular sieve is usually used as a carrier to load noble metals or transition metal oxides to form supported catalysts, which could combine the strong acidity of the supports with the high reducibility of the supported substances to form efficient catalysts for CVOCs oxidation reactions [105-108]. Zhang et al. [109] prepared three kinds of supported Co_3O_4 catalysts by supporting cobalt tetroxide on three kinds of molecular sieves (silicalite-1, ZSM-5 and TS-1), and used them for the catalytic oxidation of dichloromethane. It was found

that Co_3O_4 would partially oxidize hydrogen chloride produced by the oxidation of dichloromethane to chlorine gas due to its good activity for Deacon reaction, accompanied by the generation of a large number of polychlorinated by-products, which eventually led to the deactivation of Co_3O_4 catalyst. However, when Co_3O_4 was supported on the molecular sieve, the selectivity of hydrogen chloride in the reaction product was much higher than that of chlorine gas, and the catalyst deactivation phenomenon disappeared in the reaction temperature range. The surface acidity sites of molecular sieve have been identified as the active sites for the adsorption and oxidation of dichloromethane. Dichloromethane is adsorbed and dissociated on these sites to generate adsorbed chlorine species, and then these chlorine species desorb directly in the form of hydrogen chloride, avoiding the direct contact of Co_3O_4 and chlorine species and suppressing the production of chlorine gas and polychlorinated by-products. Therefore, the deactivation of the catalyst was inhibited. The results showed that Co_3O_4/ZSM-5 catalyst had the highest catalytic activity for the oxidation of dichloromethane due to the highest amount of Brønsted acid sites on its surface, which contributed to the faster desorption rate of the adsorbed chlorine species in the form of hydrogen chloride.

1.4 The significance and main research content of the thesis

With the rapid development of the social economy and various industries, the production of VOCs is also increasing year by year. If these pollutants are directly discharged into the atmosphere, it will pose a serious threat to the natural environment and human health. The treatment of VOCs can be roughly started from two aspects. One is to optimize industrial technology in the process of development and reduce the production of VOCs from the source. But the optimization and upgrading of technology often requires a long period of accumulation, and it is difficult to be effective in a short time. On the other hand, VOCs can be purified by improving the industrial waste gas emission standards to reduce the emissions of VOCs. The catalytic oxidation process has been considered as a useful means of practical application in VOCs purification due to its highly activity, low cost and high maneuverability, etc. In order to get efficient and stable catalysts that can be used for VOCs oxidation, it is still needed to detailly study the structure-performance relationships of the catalysts between composition, structure, active sites and catalytic performance.

Focusing on the research and development of Co_3O_4-based catalysts for the catalytic oxidation of VOCs, this paper firstly explored and calculated the catalytic oxidation mechanism of VC on Co_3O_4 through density functional theory (DFT), and then prepared a series of Co_3O_4-based catalysts and carried out structural characterizations and activity tests on them. The catalytic oxidation reactions of propane and VC were used as the model reactions of alkane and chlorine-containing VOCs, respectively. The following studies were mainly carried out:

1. The catalytic oxidation of VC on two representative crystal planes (110 and 001) of Co_3O_4 was investigated based on DFT. The reaction mechanism of VC oxidation on these two crystal planes was studied at the molecular scale and the active sites were determined. By comparing the difficulty of each unit reaction, the rate determination step of the catalytic oxidation of VC on Co_3O_4 was determined. The different catalytic activities of VC oxidation on these two crystal planes were compared, and the reasons for the difference were discussed. The reason of Cl poisoning effect on Co_3O_4 in the catalytic oxidation of VC was explained from the point of theoretical calculation, and some feasible measures to reduce Cl poisoning and improve the catalytic activity of Co_3O_4 were put forward.

2. Co_xZr_y catalysts with different contents of Zr (5%, 10% and 20%) were prepared by sol-gel method and applied in the catalytic oxidation of VC. The physicochemical properties of the catalysts were studied by XRD, N_2-sorption, H_2-TPR and some other techniques. In combination with the catalytic activity of VC oxidation, the influence of Zr on the Co_3O_4 catalyst was investigated. Finally, the stability of the most active catalyst for VC oxidation was tested.

Another series of Zr-doped Co_3O_4 catalysts (x%Zr-Co_3O_4) (0.5%, 1%, 1.5% and 2%) were prepared by sol-gel method, and their catalytic performance for propane oxidation were investigated. The physicochemical properties of Co_3O_4 catalysts, such as crystallite size, reducibility, ratio of surface Co^{2+}/Co^{3+} and surface adsorbed oxygen/lattice oxygen, and oxygen mobility, were studied by different characterization methods, and the influence of these properties on their catalytic performance was discussed. The influence of space velocity and water stream on the catalytic performance of 1%Zr-Co_3O_4 was studied. Finally, the reaction mechanism of propane oxidation on the catalyst was studied by the diffuse reflectance infrared Fourier transform spectroscopy experiment.

3. x%Nb-Co_3O_4 catalysts modified by 0.5%, 1% and 1.5% Nb doping were prepared by sol-gel method and investigated in the catalytic oxidation of propane and VC, respectively. The physicochemical properties of the catalysts were investigated by XRD, N_2-sorption, Raman, FT-IR, H_2-TPR and some other techniques, and the effects of Nb-Co interaction induced by Nb doping on the structure and catalytic activity of the catalysts were investigated. The synergistic effect of reducibility, active oxygen species and surface acidity on the catalytic reaction was revealed. The effects of space velocity and water on the performance of the most active catalyst (1%Nb-Co_3O_4) were investigated. The stability of the most active catalyst for propane and VC oxidation was tested.

4. The Co_3O_4 catalysts with different contents of residual Na were prepared by precipitation method. The contents of residual Na were obtained by controlling different washing times of the precipitate. Then, the effects of residual Na on the specific surface area,

reducibility, active oxygen species and oxygen mobility of the catalysts were studied, and the effects of residual Na on the catalytic activity of propane oxidation were also investigated. The relationship between the structure and the performance was discussed. Finally, the stability of the most active catalyst was tested.

References

[1] S. Ojala, S. Pitkäaho, T. Laitinen, N. Niskala Koivikko, R. Brahmi, J. Gaálová, L. Matejova, A. Kucherov, S. Päivärinta, C. Hirschmann, T. Nevanperä, M. Riihimäki, M. Pirilä, R.L. Keiski, Catalysis in VOC abatement. Topics in Catalysis. 2011, 54: 1224-1256.

[2] Y. Lei, M. Ning. Thoughts on control path of the volatile organic compounds pollution during the period of "13th Five-Year". Environmental Protection. 2017, 45(13): 14-17.

[3] M. Amann, M. Lutz. The revision of the air quality legislation in the European Union related to ground-level ozone. Journal of Hazardous Material. 2000, 78(1-3): 41-62.

[4] Y. Jian, M. Tian, C. He, J. Xiong, Z. Jiang, H. Jin, L. Zheng, R. Albilali, J. Shi. Efficient propane low-temperature destruction by Co_3O_4 crystal facets engineering: Unveiling the decisive role of lattice and oxygen defects and surface acid-base pairs. Applied Catalysis B: Environmental. 2021, 283: 119657.

[5] C. Yang, G. Miao, Y. Pi, Q. Xia, J. Wu, Z. Li, J. Xiao. Abatement of various types of VOCs by adsorption/catalytic oxidation: A review. Chemical Engineering Journal. 2019, 370: 1128-1153.

[6] X. Li, L. Zhang, Z. Yang, P. Wang, Y. Yan, J. Ran. Adsorption materials for volatile organic compounds (VOCs) and the key factors for VOCs adsorption process: A review. Separation & Purification Technology. 2020, 235: 116213.

[7] K. Zhou, W. Ma, Z. Zeng, X. Ma, X. Xu, Y. Guo, H. Li, L. Li. Experimental and DFT study on the adsoption of VOCs on activated acarbon/metal oxides composites. Chemical Engineering Journal. 2019, 372: 1122-1133.

[8] M.S. Kamal, S.A. Razzak, M.M. Hossain. Catalytic oxidation of volatile organic compounds (VOCs) – A review. Atmospheric Environment. 2016, 140: 117-134.

[9] Y.C. Lin, F.T. Chang, H. Bai, B.S. Pei. Control of VOCs emissions by condenser pre-treatment in a semiconductor fab. Journal of Hazardous Materials. 2005, 120(1-3): 9-14.

[10] S. Al-Gharabli, W. Kujawski, Z.A. El-Rub, E.M. Hamad, J. Kujawa. Enhancing membrane performance in removal of hazardous VOCs from water by modified fluorinated PVDF porous material. Journal of Membrane Science. 2018, 556: 214-226.

[11] D.R. van der Varrt, W.M. Vatvuk, A.H. Wehe. Thermal and Catalytic Incinerators for the control of VOCs. Air Repair. 1991, 41(1): 92-98.

[12] S.K. Padhi, S. Gokhale. Biological oxidation of gaseous VOCs–rotating biological contactor a promising and eco-friendly technique. Journal of Environmental Chemical Engineering. 2014, 2(4): 2085-2102.

[13] W. Zou, B. Gao, Y.S. Ok, L. Dong. Integrated adsorption and photocatalytic degradation of volatile organic compounds (VOCs) using carbon-based nanocomposites: A critical review. Chemosphere. 2019, 218: 845-859.

[14] W.C. Chung, D.H. Mei, X. Tu, M.B. Chang. Removal of VOCs from gas streams via plasma and catalysis. Catalysis Reviews-Science and Engineering. 2019, 61(2): 270-331.

[15] H. Huang, Y. Xu, Q. Feng, D.Y.C. Leung. Low temperature catalytic oxidation of volatile organic compounds: a review. Catalysis Science & Technology. 2015, 5(5): 2649-2669.

[16] M.S. Kamal, S.A. Razzak, M.M. Hossain. Catalytic oxidation of volatile organic compounds (VOCs) – A review. Atmospheric Environment. 2016, 140: 117-134.

[17] M. Piumetti, D. Fino, N. Russo. Mesoporous manganese oxides prepared by solution combustion synthesis as catalysts for the total oxidation of VOCs. Applied Catalysis B: Environmental. 2015, 163: 277-287.

[18] P. Yang, S. Yang, Z. Shi, Z. Meng, R. Zhou. Deep oxidation of chlorinated VOCs over CeO_2-based transition metal mixed oxide catalysts. Applied Catalysis B: Environmental. 2015, 162: 227-235.

[19] W. Tang, G. Liu, D. Li, H. Liu, X. Wu, N. Han, Y. Chen. Design and synthesis of porous non-noble metal oxides for catalytic removal of VOCs. Science China Chemistry. 2015, 58: 1359-1366.

[20] K. Everaert, J. Baeyens. Catalytic combustion of volatile organic compounds. Journal of Hazardous Materials. 2004, 109(1-3): 113-139.

[21] Z. Zhang, Z. Jiang, W. Shangguan. Low-temperature catalysis for VOCs removal in technology and application: A state-of-the-art review. Catalysis Today. 2016, 264: 270-278.

[22] Y. Wang, D. Yang, S. Li, L. Zhang, G. Zheng, L. Guo. Layered copper manganese oxide for the efficient catalytic CO and VOCs oxidaiton. Chemical Engineering Journal. 2019, 357: 258-268.

[23] L. Yu, R. Peng, L. Chen, M. Fu, J. Wu, D. Ye. Ag supported on CeO_2 with different morphologies for the catalytic oxidation of HCHO. Chemical Engineering Journal. 2018, 334: 2480-2487.

[24] C. Hu, Q. Zhu, Z. Jiang, Y. Zhang, Y. Wang. Preparation and formation mechanism of mesoporous CuO-CeO2 mixed oxides with excellent catalytic performance for removal of VOCs. Microporous and Mesoporous Materials. 2008, 113(1-3): 427-434.

[25] Q. Dai, X. Wang, G. Lu. Low-temperature catalytic destruction of chlorinated VOCs over cerium oxide. Catalysis Communications. 2007, 8(11): 1645-1649.

[26] Z. Shi, P. Yang, F. Tao, R. Zhou. New insight into the structure of CeO_2-TiO_2 mixed oxides and their excellent catalytic performance for 1,2-dichloroethane oxidation. Chemical Engineering Journal. 2016, 295: 99-108.

[27] L. Meng, H. Zhao. Low-temperature complete removal of toluene over highly active nanoparticles CuO-TiO_2 synthesized via flame spray pyrolysis. Applied Catalysis B: Environmental. 2020, 264: 118427.

[28] P. Liu, G. Wei, H. He, X. Liang, H. Chen, Y. Xi, J. Zhu. The catalytic oxidation of formaldehyde over palygorskite-supported copper and manganese oxides: Catalytic deactivation and regeneration. Applied Surface Science. 2019, 464: 287-293.

[29] H.J. Joung, J.H. Kim, J.S. Oh, D.W. You, H.O. Park, K.W. Jung. Catalytic oxidation of VOCs over CNT-supported platinum nanoparticles. Applied Surface Science. 2014, 290: 267-273.

[30] Y. Peng, L. Zhang, Y. Jiang, S. Han, Q. Zhu, X. Meng, F.S. Xiao. Fe-ZSM-5 supported palladium nanoparticles as an efficient catalyst for toluene abatement. Catalysis Today. 2019, 332: 195-200.

[31] Y. Lao, N. Zhu, X. Jiang, J. Zhao, Q. Dai, X. Wang. Effect of Ru on the activity of Co_3O_4 catalysts for chlorinated aromatics oxidation. Catalysis Science & Technology. 2018, 8(18): 4797-4811.

[32] A.C. Gluhoi, N. Bogdanchikova, B.E. Nieuwenhuys. The effect of different types of additives on the catalytic activity of Au/Al_2O_3 in propene total oxidation: transition metal oxides and ceria. Journal of Catalysis. 2005, 229(1): 154-162.

[33] V.P. Santos, S.A.C. Carabineiro, P.B. Tavares, M.F.R. Pereira, J.J.M. Órfão, J.L. Figueiredo. Oxidation of CO, ethanol and toluene over TiO_2 supported noble metal catalysts. Applied Catalysis B: Environmental. 2010, 99(1-2): 198-205.

[34] N. Imanaka, T. Masui, K. Minami, K. Koyabu, T. Egawa. Significant low-temperature redox activity of $Ce_{0.64}Zr_{0.16}Bi_{0.20}O_{1.90}$ supported on γ-Al_2O_3. Advanced Materials. 2007, 19(12): 1608-1611.

[35] T. Masui, H. Imadzu, N. Matsuyama, N. Imanaka. Total oxidation of toluene on Pt/CeO_2-ZrO_2-Bi_2O_3/γ-Al_2O_3 catalysts prepared in the presence of polyvinyl pyrrolidone. Journal of Hazardous Materials. 2010, 176(1-3): 1106-1109.

[36] C. Zhang, H. He, K. Tanaka. Perfect catalytic oxidation of formaldehyede over a Pt/TiO_2 catalyst at room temperature. Catalysis Communications. 2005, 6(3): 211-214.

[37] C. Zhang, H. He. A comparative study of TiO_2 supported noble metal catalysts for the oxidation of formaldehyde at room temperature. Catalysis Today. 2007, 126(3-4): 345-350.

[38] C. Zhang, H. He, K. Tanaka. Catalytic performance and mechanism of a Pt/TiO_2 catalyst for the oxidation of formaldehyde at room temperature. Applied Catalysis B: Environmental. 2006, 65(43467): 37-43.

[39] M. Ousmane, L.F. Liotta, G.Di Carlo, G. Pantaleo, A.M. Venezia, G. Deganello, L. Retailleau, A. Boreave, A. Giroir-Fendler. Supported Au catalysts for low-temperature

abatement of propene and toluene, as model VOCs: Support effect. Applied Catalysis B: Environmental. 2011, 101(3-4): 629-637.

[40] J. Zhao, W. Xi, C. Tu, Q. Dai, X. Wang. Catalytic oxidation of chlorinated VOCs over Ru/Ti_xSn_{1-x} catalysts. Applied Catalysis B: Environmental. 2020, 263: 118237.

[41] H. Huang, Q. Dai, X. Wang. Morphology effect of Ru/CeO_2 catalysts for the catalytic combustion of chlorobenzene. Applied Catalysis B: Environmental. 2014, 158-159: 96-105.

[42] X. Liu, L. Chen, T. Zhu, R. Ning. Catalytic oxidation of chlorobenzene over noble metals (Pd, Pt, Ru, Rh) and the distributions of polychlorinated by-products. Journal of Hazardous Materials. 2019, 363: 90-98.

[43] L. Ran, Z. Qin, Z. Wang, X. Wang, Q. Dai. Catalytic decomposition of CH_2Cl_2 over supported Ru catalysts. Catalysis Communications. 2013, 37: 5-8.

[44] C. Wang, C. Zhang, W. Hua, Y. Guo, G. Lu, S. Gil, A. Giroir-Fendler. Low-temperature catalytic oxidation of vinyl chloride over Ru modified Co_3O_4 catalysts. RSC Advances. 2016, 6(101): 99577-99585.

[45] Y. Guo, W. Hua, X. Guo, R. Luo, L. Wang, L. Zhang, G. Lu, W. Zhan, Y. Guo, L. Wang, Y.Wang. The preparation method and application of the Ru/SnO_2 catalyst for the catalytic combustion of vinyl chloride. CN 107233882A. 2017.

[46] Q. Ren, Z. Feng, S. Mo, C. Huang, S. Li, W. Zhang, L. Chen, M. Fu, J. Wu, D. Ye. 1D-Co_3O_4, 2D- Co_3O_4, 3D- Co_3O_4 for catalytic oxidation of toluene. Catalysis Today. 2019, 332: 160-167.

[47] J. González-Prior, R. López-Fonseca, J.I. Gutiérrez-Ortiz, B. de Rivas. Oxidation of 1,2-dichloroethane over nanocube-shaped Co_3O_4 catalysts. Applied Catalysis B: Environmental. 2016, 199: 384-393.

[48] R. Wang, J. Li. Effects of precursor and sulfation on OMS-2 catalyst for oxidation of ethanol and acetaldehyde at low temperatures. Environmental Science & Technology. 2010, 44(11): 4282-4287.

[49] A.K. Sinha, K. Suzuki. Novel mesoporous chromim oxide for VOCs elimination. Applied Catalysis B: Environmental. 2007, 70(1-4): 417-422.

[50] B. Bai, Q. Qiao, J. Li, J. Hao. Synthesis of three-dimensional ordered mesoporous MnO_2 and its catalytic performance in formaldehyede oxidation. Chinese Journal of Catalysis. 2016, 37(1): 27-31.

[51] Q. Dai, X. Wang, G. Lu. Low-temperature catalytic combustion of trichloroethylene over cerium oxide and catalyst deactivation. Applied Catalysis B: Environmental. 2008, 81(3-4): 192-202.

[52] B. Solsona, T. García, R. Sanchis, M.D. Soriano, M. Moreno, E. Rodríguez-Castellón, S. Agouram, A. Dejoz, J.M. López Nieto. Total oxidation of VOCs on mesoporous iron oxide

catalysts: Soft chemistry route versus hard template method. Chemical Engineering Journal. 2016, 290: 273-281.

[53] Y. Xia, H. Dai, H. Jiang, L. Zhang, J. Deng, Y. Liu. Three-dimensionally ordered and wormhole-like mesoporous iron oxide catalysts highly active for the oxidation of acetone and methanol. Journal of Hazardous Materials. 2011, 186(1): 84-91.

[54] W. Tang, X. Wu, D. Li, Z. Wang, G. Liu, H. Liu, Y. Chen. Oxalate route for promoting activity of manganese oxide catalysts in total VOCs' oxidation: effect of calcination temperature and preparation method. Journal of Materials Chemistry A. 2014, 2(8): 2544-2554.

[55] X. Chen, X. Chen, E. Yu, S. Cai, H. Jia, J. Chen, P. Liang. In situ pyrolysis of Ce-MOF prepare CeO_2 catalyst with obviously improved catalytic performance for toluene combustion. Chemical Engineering Journal. 2018, 344: 469-479.

[56] L. Ma, Y. Geng, X. Chen, N. Yan, J. Li, J.W. Schwank. Reaction mechanism of propane oxidation over Co3O4 nanorods as rivals of platinum catalysts. Chemical Engineering Journal. 2020, 402: 125911.

[57] L. Wang, Y. Wang, Y. Zhang, Y. Yu, H. He, X. Qin, B. Wang. Shape dependence of nanoceria on complete catalytic oxidation of *o*-xylene. Catalysis Science & Technology. 2016, 6(13): 4840-4848.

[58] M. Piumetti, D. Fino, N. Russo. Mesoporous manganese oxides prepared by solution combustion synthesis as catalysts for the total oxidation of VOCs. Applied Catalysis B: Environmental. 2015, 163: 277-287.

[59] H.F. Wang, D. Wang, X. Liu, Y.L. Guo, G.Z. Lu, P. Hu. Unexpected C-C bond cleavage mechanism in ethylene combustion at low temperature: Origin and implications. ACS Catalysis. 2016, 6: 5393-5398.

[60] B. Faure, P. Alphonse. Co-Mn-oxide spinel catalysts for CO and propane oxidation at mild temperature. Applied Catalysis B: Environmental. 2016, 180: 715-725.

[61] M.H. Castaño, R. Molina, S. Moreno. Catalytic oxidation of VOCs on $MnMgAlO_x$ mixed oxides obtained by auto-combustion. Journal of Molecular Catalysis A: Chemical. 2015, 398: 358-367.

[62] W. Tang, X. Wu, S. Li, W. Li, Y. Chen. Porous Mn-Co mixed oxide nanorod as a novel catalyst with enhanced catalytic activity for removal of VOCs. Catalysis Communications. 2014, 56: 134-138.

[63] C. Wang, C. Zhang, W. Hua, Y. Guo, G. Lu, S. Gil. A. Giroir-Fendler. Catalytic oxidaiton of vinyl chloride emissions over Co-Ce composite oxide catalysts. Chemical Engineering Journal. 2017, 315: 392-402.

[64] X. Feng, F. Luo, Y. Chen, D. Lin, Y. Luo, L. Xiao, X. Liu, X. Sun, Q. Qian, Q. Chen. Boosting total oxidation of propane over CeO_2@Co_3O_4 nanofiber catalysts prepared by

multifluidic coaxial electrospinning with continuous grain boundary and fast lattice oxygen mobility. Journal of Hazardous Materials. 2021, 406: 124695.

[65] Z. Hu, S. Qiu, Y. You, Y. Guo, Y. Guo, L. Wang, W. Zhan, G. Lu. Hydrothermal synthesis of $NiCeO_x$ nanosheets and its application to the total oxidation of propane. Applied Catalysis B: Environmental. 2018, 225: 110-120.

[66] Y. Xie, Y. Guo, Y. Guo, L. Wang, W. Zhan, Y. Wang, X. Gong, G. Lu. A highly effective Ni-modified MnO_x catalyst for total oxidation of propane: the promotional role of nickel oxide. RSC Advances. 2016, 6(55): 50228-50237.

[67] W. Sun, B. Gong, J. Pan, Y. Wang, H. Xia, H. Zhang, Q. Dai, L. Wang, X. Wang. Catalytic combustion of CVOCs over Cr_xTi_{1-x} oxide catalysts. Journal of Catalysis. 2020, 391: 132-144.

[68] C. He, Y. Yu, L. Yue, N. Qiao, J. Li, Q. Shen, W. Yu, J. Chen, Z. Hao. Low-temperature removal of toluene and propanal over highly active mesoporous $CuCeO_x$ catalysts synthesized via a simple self-precipitation protocol. Applied Catalysis B: Environmental. 2014, 147: 156-166.

[69] W. Hua, C. Zhang, Y. Guo, G. Chai, C. Wang, Y. Guo, L. Wang, Y. Wang, W. Zhan. An efficient $Sn_yMn_{1-y}O_x$ composite oxide catalyst for catalytic combustion of vinyl chloride emissions. Applied Catalysis B: Environmental. 2019, 255: 117748.

[70] P.M. Shah, A.N. Day, T.E. Davies, D.J. Morgan, S.H. Taylor. Mechanochemical preparation of ceria-zirconia catalysts for the total oxidation of propane and naphtanlene volatile organic compounds. Applied Catalysis B: Environmental. 2019, 253: 331-340.

[71] J. Chen, X. Chen, W. Xu, Z. Xu. J. Chen, H. Jia, J. Chen. Hydrolysis driving redox reaction to synthesize Mn-Fe binary oxides as highly active catalysts for the removal of toluene. Chemical Engineering Journal. 2017, 330: 281-293.

[72] Y. Wang, L. Zhang, L. Guo. Enhanced toluene combustion over highly homogeneous iron manganese oxide nanocatalysts. ACS Applied Nano Materials. 2018, 1(3): 1066-1075.

[73] M.R. Morales, B.P. Barbero, L.E. Cadús. Combustion of volatile organic compounds on manganese iron or nickel mixed oxide catalysts. Applied Catalysis B: Environmental. 2007, 74(1-2): 1-10.

[74] S. Akram, Z. Wang, L. Chen, Q. Wang, G. Shen, N. Han, Y. Chen, G. Ge. Low-temperature efficient degradation of ethyl acetate catalyzed by lattice-doped CeO_2-CoO_x nanocomposites. Catalysis Communications. 2016, 73: 123-127.

[75] X. Jiang, X. Li, J. Wang, D. Long, L. Ling, W. Qiao. Three-dimensional Mn-Cu-Ce ternary mixed oxide networks prepared by polymer-assisted deposition for HCHO catalytic oxidation. Catalysis Science & Technology. 2010, 8(10): 2740-2749.

[76] W. Zhu, X. Chen, J. Jin, X. Di, C. Liang, Z. Liu. Insight into catalytic properties of Co_3O_4-CeO_2 binary oxides for propane total oxidation. Chinese Journal of Catalysis. 2020, 41(4): 679-690.

[77] Z. Ye, J.M. Giraudon, N. Nuns, P. Simon, N. De Geyter, R. Morent, J.F. Lamonier. Influence of the preparation method on the activity of copper-manganese oxides for toluene total oxidation. Applied Catalysis B: Environmental. 2018, 223: 154-166.

[78] H. Liu, X. Li, Q. Dai, H. Zhao, G. Chai, Y. Guo, Y. Guo, L. Wang, W. Zhan. Catalytic oxidation of chlorinated volatile organic compounds over Mn-Ti composite oxides catalysts: Elucidating the influence of surface acidity. Applied Catalysis B: Environmental. 2021, 282: 119577.

[79] C. Zhang, Y. Wang, G. Li, L. Chen, Q. Zhang, D. Wang, X. Li, Z. Wang. Tuning smaller Co_3O_4 nanoparticles onto HZSM-5 zeolite via complexing agents for boosting toluene oxidation performance. Applied Surface Science. 2020, 532: 147320.

[80] W. Huang, Y. Liu, Z. Wu. Enhanced stability of HZSM-5 supported copper oxides by Na doping for catalytic combustion of propene. Catalysis Communications. 2019, 122: 58-62.

[81] Y. Wang, S. Aghamohammadi, D. Li, K. Li, R. Farrauto. Structure dependence of Nb_2O_{5-x} supported manganese oxide for catalytic oxidation of propane: Enhanced oxidation activity for MnO_x on a low surface area Nb_2O_{5-x}. Applied Catalysis B: Environmental. 2019, 244: 438-447.

[82] J. Su, Y. Liu, W. Yao, Z. Wu. Catalytic combustion of dichloromethane over HZSM-5-supported Typical Transition Metal (Cr, Fe, and Cu) oxide catalysts: A stability study. The Journal of Physical Chemistry C. 2016, 120(32): 18046-18054.

[83] H.F. Lu, Y. Zhou, W.F. Han, H.F. Huang, Y.F. Chen. High thermal stability of ceria-based mixed oxide catalysts supported on ZrO_2 for toluene combustion. Catalysis Science & Technology. 2013, 3(6): 1480-1484.

[84] S. Todorova, J.L. Blin, A. Naydenov, B. Lebeau, D. Karashanova, H. Kolev, P. Gaudin, R. Velinova, L. Vidal, L. Michelin, L. Josien, D. Filkova, I. Ivanova, A. Dotzeva, K. Tenchev. Co-Mn oxides supported on hierarchical macro-mesoporous silica for CO and VOCs oxidation. Catalysis Today. 2021, 361: 94-101.

[85] J. Zeng, X. Liu, J. Wang, H. Lv, T. Zhu. Catalytic oxidation of benzene over MnO_x/TiO_2 catalysts and the mechanism study. Journal of Molecular Catalysis A: Chemical. 2015, 408: 221-227.

[86] W. Li, Z. Zhang, J. Wang, W. Qiao, D. Long, L. Ling. Low temperature catalytic combustion of ethylene over cobalt oxide supported mesoporous carbon spheres. Chemical Engineering Journal. 2016, 293: 243-251.

[87] Q. Dai, L.L. Yin, S. Bai, W. Wang, X. Wang, X.Q. Gong, G. Lu. Catalytic total oxidation of 1,2-dichloroethane over VO_x/CeO_2 catalysts: Further insights via isotopic tracer techniques. Applied Catalysis B: Environmental. 2016, 182: 598-610.

[88] H. Xie, X. Zhao, G. Zhou, X. He, H. Lan, Z. Jiang. Investigating the performance of Co_xO_y/activated carbon catalysts for ethyl acetate catalytic combustion. Applied Surface Science. 2015, 326: 119-123.

[89] S. Cao, M. Shi, H. Wang, F. Yu, X. Weng, Y. Liu, Z. Wu. A two-stage Ce/TiO_2-Cu/CeO_2 catalyst with separated catalytic functions for deep catalytic combustion of CH_2Cl_2. Chemical Engineering Journal. 2016, 290: 147-153.

[90] Z. Zhu, G. Lu, Z. Zhang, Y. Guo, Y. Guo, Y. Wang. Highly active and stable Co_3O_4/ZSM-5 catalyst for propane oxidation: Effect of the preparation method. ACS Catalysis. 2013, 3(6): 1154-1164.

[91] P. Liu, H. He, G. Wei, D. Liu, X. Liang, T. Chen, J. Zhu, R. Zhu. An efficient catalyst of manganese supported on diatomite for toluene oxidation: Manganese species, catalytic performance, and structure-activity relationship. Microporous and Mesoporous Materials. 2017, 239: 101-110.

[92] Y. Wang, Y. Xue, C. Zhao, D. Zhao, F. Liu, K. Wang, D.D. Dionysiou. Catalytic combustion of toluene with $La_{0.8}Ce_{0.2}MnO_3$ supported on CeO_2 with different morphologies. Chemical Engineering Journal. 2016, 300: 300-305.

[93] Y.W. Chen, B. Li, Q. Niu, L. Li, J.W. Kan, S.M. Zhu, S.B. Shen. Combined promoting effects of low-Pd-containing and Cu-doped $LaCoO_3$ perovskite supported on cordierite for the catalytic combustion of benzene. Environmental Science and Pollution Research. 2016, 23: 15193-15201.

[94] H. Chen, G. Wei, X. Liang, P. Liu, H. He, Y. Xi, J. Zhu. The distinct effects of substitution and deposition of Ag in perovskite $LaCoO_3$ on the thermally catalytic oxidation of toluene. Applied Surface Science. 2019, 489: 905-912.

[95] J. Zhang, D. Tan, Q. Meng, X. Weng, Z. Wu. Structural modification of $LaCoO_3$ perovskite for oxidation reactions: The synergistic effect of Ca^{2+} and Mg^{2+} co-substitution on phase formation and catalytic performance. Applied Catalysis B: Environmental. 2015, 172-173: 18-26.

[96] C. Zhang, C. Wang, S. Gil, A. Boreave, L. Retailleau, Y. Guo, J.L. Valverde, A. Giroir-Fendler. Catalytic oxidation of 1,2-dichloropropane over supported $LaMnO_x$ oxides catalysts. Applied Catalysis B: Environmental. 2017, 201: 552-560.

[97] A. Giroir-Fendler, M. Alves-Fortunato, M. Richard, C. Wang, J.A. Díaz, S. Gil, C. Zhang, F. Can, N. Bion, Y. Guo. Synthesis of oxide supported $LaMnO_3$ perovskites to enhance yields in toluene combustion. Applied Catalysis B: Environmental. 2016, 180: 29-37.

[98] Y. Lu, Q. Dai, X. Wang. Catalytic combustion of chlorobenzene on modified $LaMnO_3$ catalysts. Catalysis Communications. 2014, 54: 114-117.

[99] W. Zhu, X. Chen, Z. Liu, C. Liang. Insight into the effect of cobalt substitution on the catalytic performance of $LaMnO_3$ perovskites for total oxidation of propane. The Journal of Physical Chemistry C. 2020, 124(27): 14646-14657.

[100] S.X. Chen, Y. Wang, A.P. Jia, H.H. Liu, M.F. Luo, J.Q. Lu. Enhanced activity for catalytic oxidation of 1,2-dichloroethane over Al-substituted $LaMnO_3$ perovskite catalysts. Applied Surface Science. 2014, 307: 178-188.

[101] L. Intriago, E. Díaz, S. Ordóñez, A. Vega. Combustion of trichloroethylene and dichloromethane over protonic zeolites: Influence of adsoption properties on the catalytic performance. Microporous and Mesoporous Materials. 2006, 91(1-3): 161-169.

[102] R. López-Fonseca, A. Aranzabal, J.I. Gutiérrez-Ortiz, J.R. Gonzalez-Velasco. Comparative study of the oxidative decomposition of trichloroethylene over H-type zeolites under dry and humid conditions. Applied Catalysis B: Environmental. 2001, 30(3-4): 303-313.

[103] A. Aranzabal, J.A. González-Marcos, M. Romero-Sáez. J.R. Gonzalez-Velasco, M. Guillemot, P. Magnous. Stability of protonic zeolites in the catalytic oxidation of chlorinated VOCs (1,2-dichloroethane). Applied Catalysis B: Environmental. 2009, 88(3-4): 533-541.

[104] R. López-Fonseca, A. Aranzabal, P. Steltenpohl, J.I. Gutiérrez-Ortiz, J.R. Gonzalez-Velasco. Performance of zeolites and product selectivity in the gas-phase oxidation of 1,2-dichloroethane. Catalysis Today. 2000, 62(4): 367-377.

[105] L. Zhang, Y. Peng, J. Zhang, L. Chen, X. Meng, F.S. Xiao. Adsorptive and catalytic properties in the removal of volatile organic compounds over zeolite-based materials. Chinese Journal of Catalysis. 2016, 37(6): 800-809.

[106] W. Tang, Y. Deng, Y. Chen. Promoting effect of acid treatment on Pd-Ni/SBA-15 catalyst for complete oxidation of gaseous benzene. Catalysis Communications. 2017, 89: 86-90.

[107] X. Weng, P. Sun, Y. Long, Q. Meng, Z. Wu. Catalytic oxidation of chlorobenzene over $Mn_xCe_{1-x}O_2$/HZSM-5 catalysts: A study with practical implications. Environmental Science & Technology. 2010, 51(14): 8057-8066.

[108] M. Tian, M. Ma, B. Xu, C. Chen, C. He, Z. Hao, R. Albilali. Catalytic removal of 1,2-dichloroethane over $LaSrMnCoO_6$/H-ZSM-5 composite: Insight into synergistic effect and pollutant-destruction mechanism. Catalysis Science & Technology. 2018, 8(17): 4503-4514.

[109] L. Zhang, S. Huang, W. Deng, D. Yang, Q. Tang, S. Zhu, L. Guo. Dichloromethane catalytic combustion over Co_3O_4 catalysts supported on MFI type zeolites. Microporous and Mesoporous Materials. 2021, 312: 110599.

Chapter 2 Experimental methodology

2.1 Experimental material

The main reagents required for the experiment are shown in Table 2.1, and the main gases used are shown in Table 2.2.

Table 2.1 Main experimental reagents

Name	Formula	Purity	Supplier
Cobalt nitrate	$Co(NO_3)_2·6H_2O$	Analytical Grade	Sinopharm Chemical Reagent Co., Ltd
Zirconyl nitrate	$ZrO(NO_3)_2·nH_2O$	Analytical Grade	Shanghai Lingfeng Chemical Reagent Co., Ltd
Citric acid	$C_6H_8O_7$	Analytical Grade	Shanghai Lingfeng Chemical Reagent Co., Ltd
Polyethylene glycol	$HO(CH_2CH_2O)_nH$	Analytical Grade	Sinopharm Chemical Reagent Co., Ltd
Ammonium niobate oxylate hydrate	$C_4H_4NNbO_9·xH_2O$	Analytical Grade	Sigma-Aldrich
Sodium carbonate	Na_2CO_3	Analytical Grade	Sigma-Aldrich
Sodium hydroxide	NaOH	Analytical Grade	Sigma-Aldrich
Titanium dioxide	TiO_2	Analytical Grade	Cristal Company
Yttria stabilization zirconia	YSZ	Analytical Grade	Tosoh Corporation
Toluene	$C_6H_5CH_3$	Analytical Grade	Sigma-Aldrich
Deionized water	H_2O	99.99%	Homemade

Table 2.2 Main experimental gases

Name	Purity	Supplier
Vinyl chloride	$2\%C_2H_3Cl+98\%N_2$	Shanghai Pujiang Special Gas Co., Ltd
Nitrogen	≥99.999%	Shanghai Pujiang Special Gas Co., Ltd
Hydrogen	≥99.999%	Shanghai Pujiang Special Gas Co., Ltd
Air	≥99.999%	Air pump homemade
Propane	≥99.999%	Linde Gas
Oxygen	≥99.999%	Linde Gas
Helium	≥99.999%	Linde Gas
Synthetic air	$21\%O_2+79\%He$	Linde Gas

2.2 Experimental instruments and apparatus

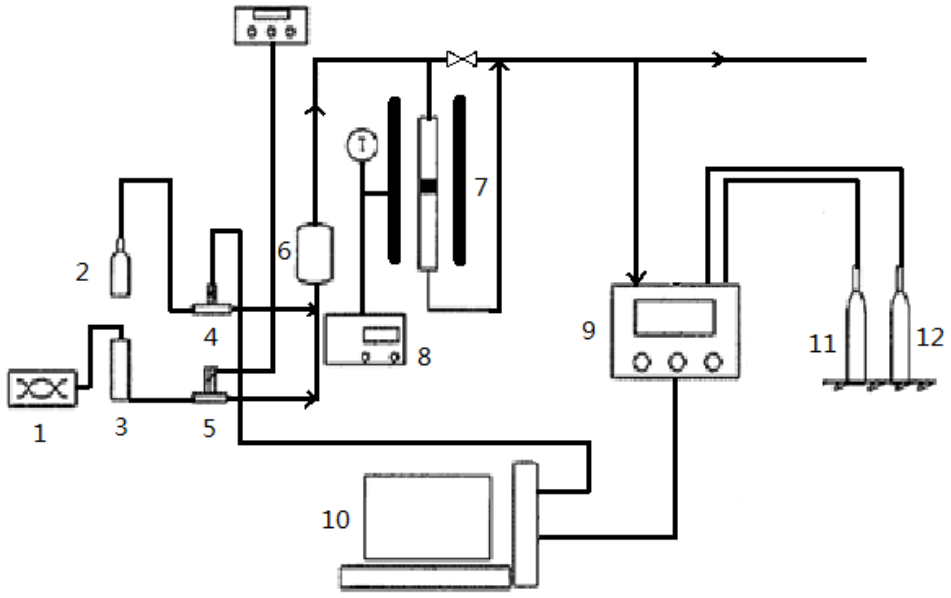

1. Air compressor，2. VC， 3. Desiccator， 4. Digital mass flow controller， 5. Digital mass flow controller， 6. Admixer， 7. Electric furnace， 8. Temperature-programmed controller， 9. Gas chromatograph， 10. Computer， 11. Nitrogen， 12. Hydrogen。

Fig. 2.1 Apparatus for catalytic oxidation of vinyl chloride-ECUST.

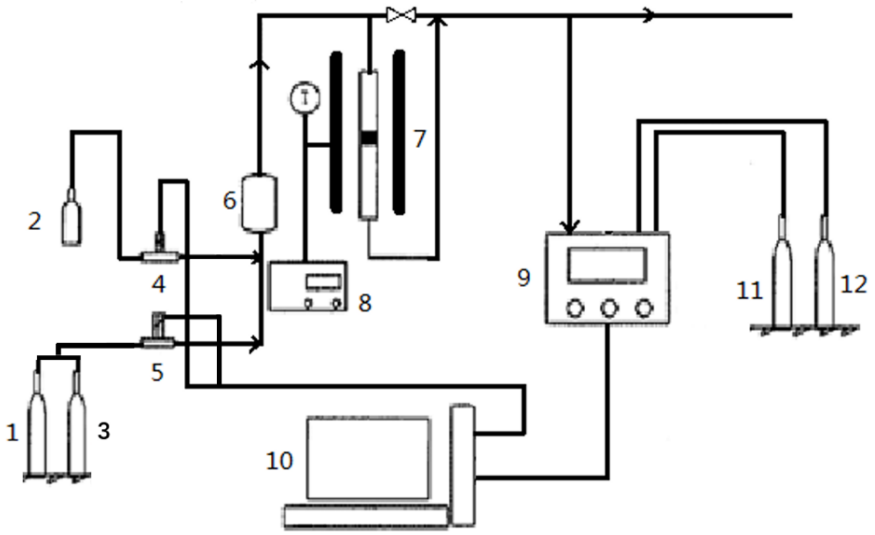

1. Oxygen，2. Propane， 3. Helium， 4. Digital mass flow controller， 5. Digital mass flow controller， 6. Admixer， 7. Electric furnace， 8. Temperature-programmed controller， 9. Gas chromatograph， 10. Computer， 11. Helium， 12. Hydrogen。

Fig. 2.2 Apparatus for catalytic oxidation of propane-UCBL1.

Table 2.3 Main experimental instruments

Name	Supplier
Electronic precision balance PL203	Mettler Toledo Instruments Co., Ltd
Thermostatic magnetic stirrer S21-2	Shanghai Sile Instruments Co., Ltd
Oven DHG	Shanghai Jinghong Experimental Equipment Co., Ltd
Muffle furnace	Shanghai Songping Electric Furnace Co., Ltd
Digital mass flow controller CS200A	Beijing Sevenstar Flow Co., Ltd
Gas chromatograph Clarus 580	PerkinElmer
Electronic precision balance BSA323S	Sartorius
Muffle furnace	Nabertherm
Digital mass flow controller 5850TR	Brooks
Gas chromatograph	SRA Instruments
Infrared detector X-STREAM	Emerson

2.3 Preparation of Catalysts

The catalyst preparation method is described in the subsequent chapters.

2.4 Characterization of catalysts

2.4.1 Thermo gravimetric analysis (TGA)

TGA of the powders was conducted on a SETARAM Setsys Evolution 12 Calorimeter. The powders were dried in an oven at 80 °C before handing, then, 3~7 mg of each sample was heated in flowing air (50 mL min^{-1}) at a heating rate of 10 °C min^{-1}. The temperature range was set from 50 to 550 °C. An empty aluminum pan was used as a reference.

2.4.2 X-ray diffraction (XRD)

XRD patterns of the catalysts in Chapter 4 were carried out on a Bruker AXS D8 Focus diffractometer with Cu Kα radiation (40 kV, 40 mA, λ = 1.5406 Å) operated at 40 kV and 40 mA. The catalysts were scanned in 2θ range from 10° to 80° with a a scanning speed of 6° min^{-1}. XRD patterns of the other catalysts were recorded on a Bruker D5005 diffractometer using a Cu Kα radiation (λ = 0.154184 nm). The continuous scanning was registered in the 2θ range of 10-80° with a step size of 0.02° and a scanning speed of 2 s per step.

2.4.3 Raman spectra

Raman spectra were obtained on a HORIBA Jobin Yvon Raman instrument with a 514 nm excitation wavelength and a CCD detector. The scanning range was set at 150–800 cm^{-1}.

2.4.4 Inductively coupled plasma-optical emission spectrometer (ICP-OES)

Elemental analysis of the catalysts was carried out using HORIBA Jobin Yvon Activa instrument. The catalysts were pretreated in acidic solution with H_2SO_4 and HNO_3 at 250 ℃ for complete dissolution.

2.4.5 N_2-sorption

N2-sorption isotherms were recorded at −196 °C on a Micromeritics TRISTAR II apparatus. Before the measurement, the samples were outgassed at 300 °C under vacuum for 3 h. The Brunauer-Emmet-Teller (BET) method was applied to obtain the specific surface area (SSA) of the catalysts. The pore size distribution and total pore volume (V_{pore}) were calculated using the Barrett-Jouner-Halenda (BJH) method.

2.4.6 Fourier transform infrared spectroscopy (FT-IR)

FT-IR analysis was carried out on a PerkinElmer FT-IR C92712 spectrometer. The spectrum was recorded in the range of 400–4000 cm^{-1} with a resolution of 1 cm^{-1}.

2.4.7 Scanning electron microscope (SEM)

SEM characterization of the catalysts was performed on a Hitachi S-3400N microscope with an electron accelerating voltage of 15 kV. The specimens were prepared by pasting the catalyst powder to the stage and needed to be plated before test.

2.4.8 X-ray photoelectron spectroscopy (XPS)

XPS measurement of the catalysts was performed on a Thermo Fisher ESCALAB 250Xi electron spectrometer with the excitation source of Al Kα (hν = 1486.6 eV) radiation. The charge of energy shift of the XPS spectra was corrected by setting the binding energy (B.E.) of contaminative carbon (C 1s) at 284.6 eV.

2.4.9 Temperature-programmed reduction of hydrogen (H_2-TPR)

H_2-TPR experiments of the catalysts in Chapter 4 were performed on a Micromeritics Autochem 2910 apparatus equipped with a thermal conductivity detector (TCD). The sample (~ 20 mg) was pretreated with O_2 (5 vol.% in He, 30 mL min^{-1}) at 500 °C for 1 h, then, cooled down under He. The TPR experiment was registered by flowing over the sample a gas mixture (5 vol.% H_2 in Ar, 30 mL min^{-1}), heating from 50 to 1000 °C with a rate of 10 °C min^{-1}. The influence of mass transfer on the shape of the TPR profiles has been avoided by controlling the sample amount (not exceeding 22 mg) and mixing the sample with silicon carbide. H_2-TPR experiments of the other catalysts were performed on PX200 apparatus from Pengxiang Technology Co., Ltd. The test process is similar.

2.4.10 Temperature-programmed reduction of carbon monoxide (CO-TPR)

CO-TPR experiments were conducted in a conventional flow system equipped with a TCD detector. A CO/He flow (100 mL min^{-1}) containing 3000 ppm CO was flowed over the sample pretreated with a He flow at 300 °C for 1 h, heating from 50 to 700 °C with a rate of 5 °C min^{-1}.

2.4.11 Temperature-programmed desorption of oxygen (O_2-TPD)

O_2-TPD experiments were performed with a TGA/DSC1 STAR system Mettler Toledo. The sample (15 mg) was pretreated in N_2 (30 mL min^{-1}), heating from 25 to 500 °C with a rate of 10 °C min^{-1} and maintained at this temperature for 15 min, to clean the surface and remove any chemisorbed species. Then, it was cooled down to 150 °C under N_2 atmosphere and saturated with pure O_2 for 1 h at the same temperature. After cooling down to 25 °C under O_2, a temperature programmed desorption (TPD) experiment was started by heating the sample from room temperature up to 800 °C with a rate of 5 °C min^{-1} under N_2 flow. The weight loss recorded during the TPD experiment was discussed in terms of desorbed oxygen species, according to the signal registered by online mass quadrupole (Thermostar TM, Balzers).

2.4.12 Temperature-programmed desorption of ammonia (NH_3-TPD)

NH_3-TPD experiments were conducted with the PX200 apparatus from Pengxiang Technology Co., Ltd. The catalysts were pre-treated at 300 °C for 1h with an Ar flow. After being cooled down to room temperature, the gas flow was changed to NH_3/Ar and kept for 30min. After stabilization at 80 °C for 30 min in Ar flow at a flow rate of 30 mL min^{-1}, the catalysts were heated from 80 to 500 °C with a heating rate of 10 °C/min.

2.4.13 Diffuse reflectance infrared Fourier transform spectroscopy (DRIFTS)

DRIFTS data were recorded on a Nicolet Nexus 670 FTIR spectrometer with 64 scans at an effective resolution of 4 cm^{-1}. The sample was pre-treated at 300 °C in Ar for 1 h and then cooled to 220 °C. The background spectrum was collected and subtracted from the sample spectrum at 220 °C. For the propane adsorption tests, 0.5 vol.% propane/Ar was introduced into the sample cell. For the reaction tests, 10 vol.% O_2 was incorporated. At the desorption stage, the mixed gas was switched to 10 vol.% O_2/Ar. The DRIFTS spectra of the sample were collected at a specific time. When the experiments were carried out, the total flow rate was kept at 50 mL min^{-1}, and each stage lasted for approximately 25 min.

2.5 Measurement of catalytic activity

2.5.1 Activity test for the catalytic oxidation of VC

Catalytic oxidation reactions were carried out at atmospheric pressure in a quartz fixed bed reactor with 6 mm inner diameter. For each catalyst, 200 mg sample (40 - 60 meshes) was used and mixed with an amount of silica, which had the same grain size as the sample. Then the feed gas containing 1000 ppm VC and air balance gas was passed through the catalyst bed at a flow rate of 100 mL min^{-1}, corresponding to a weight hourly space velocity (WHSV) of 30000 mL g^{-1} h^{-1}. After stabilization below 100 °C, the reaction was run in a step of 20 °C from 100 to 440 °C with a 40 min plateau at each temperature. The reactants and chlorinated by-products were analyzed online using a PerkinElmer Clarus 580 gas chromatograph equipped

with a flame ionization detector (FID). The conversion was calculated by the difference between inlet and outlet VC concentrations. The conversion (X_{VC}) and reaction rate (r) of VC were calculated by the following equations:

$$X_{VC} = \frac{[VC]_{in}-[VC]_{out}}{[VC]_{in}} \times 100\% \quad (2\text{-}1)$$

$$r = {X_{VC} * V_{VC}}/{M} \quad (2\text{-}2)$$

Where $[VC]_{in}$ and $[VC]_{out}$ represent the VC concentrations in the inlet and outlet gas, respectively. V_{VC} is the flow rate of VC gas (mol s^{-1}), and M is the weight of the catalyst (g).

2.5.2 Activity test for the catalytic oxidation of propane

Catalytic oxidation experiments were performed at atmospheric pressure in a U-shaped quartz fixed-bed reactor of 4 mm inner diameter. For the activity measurement, 150 mg catalyst was mixed with an amount of silicon carbide (~ 600 mg) to avoid any hot spot. The heigh of the catalytic bed was thus kept at 6 mm.

For propane oxidation, the feed gases (0.1 vol.% propane + 21 vol.% O_2 + He) were flowed over the catalyst bed with a flow rate of 100 mL min^{-1}, corresponding to a weight hourly space velocity (WHSV) of 40,000 mL g^{-1} h^{-1} (gas hourly space velocity (GHSV) of ~ 80,000 h^{-1}). After 30 min stabilization at 100 °C, the temperature was raised to 350 °C with a heating rate of 2 °C min^{-1} and kept for 1h. Then the reactor was cooled down to 100 °C with the same rate (2 °C min^{-1}). Three consecutive heating-cooling catalytic cycles were conducted to evaluate the catalytic stability. The outlet gases were in-situ analyzed online by using a gas chromatograph equipped with two TCDs for quantitative analyses. The conversion of propane to CO_2 was calculated by the following equation:

$$X_{C_3H_8} = \frac{[CO_2]_{out}-[CO_2]_{in}}{3[C_3H_8]} \times 100\% \quad (2\text{-}3)$$

Where $[CO_2]_{out}$ and $[CO_2]_{in}$ represented the outlet and inlet CO_2 concentrations. The reaction rate is calculated in a similar way to vinyl chloride.

The reaction temperatures for 50% and 90% conversions of propane or VC were assigned to T_{50} and T_{90}, respectively.

2.6 Details of the density functional theory (DFT) calculations

The reaction mechanism of VC oxidation over Co_3O_4 catalyst was studied by DFT. All the spin-polarized density functional theory (DFT) calculations have been performed with Perdew-Burke-Ernzerh (PBE) functional within the generalized gradient approximation (GGA) [1] using the VASP code [2-3]. The project-augmented wave (PAW) pseudopotentials [4] were used to represent the core-valence electron interaction. The valence electronic states were expanded in plane wave basis sets with a cutoff energy of 450 eV. Considering the strong

correlation between the electrons in partially occupied 3d orbitals of Co, the PBE+U approach (U = 2.0 eV for Co-3d orbital) with the on-site Coulomb correction included was applied. For the bulk structure of spinel Co_3O_4, a 4×4×4 k-point mesh was used and the optimized lattice constant is 8.084 Å, agreeing well with the experimental result (8.065 Å) [5]. Note that the stable spin antiferromagnet (AFM) configuration was used for the interior layers of the slab model [6-7]. The Co_3O_4(110) surface (Figure 2.3) was modeled as a p(1×1/2) slab with six atomic layers and the vacuum between slabs is ~15 Å. The bottom two layers were fixed, and all other atoms were fully relaxed. The Co_3O_4(001) surface was modeled as a p(1×1) slab with twelve atomic layers, in which the bottom six layers were fixed, and all others were fully relaxed. The vacuum between slabs is ~20 Å. The force threshold for the optimization was 0.05 eV/Å.

The transition states were searched using the constrained optimization scheme [8-10] and were verified when (i) all forces on atoms vanish and (ii) the total energy is a maximum along the reaction coordination, but a minimum with respect to the remaining degrees of freedom. The force threshold for the optimization and transition-state search was 0.05 eV/Å. Our previous works [6, 11] confirm that the above settings can give reasonable results. In addition, the adsorption energy, E_{ad}, of surface species was defined as:

$$E_{ad} = E_{surf/adsorbate} - E_{surf} - E_{adsorbate} \quad (2\text{-}4)$$

Where $E_{sur/adsorbate}$ and E_{surf} are the total energies of the surface slab with and without the adsorbate, respectively, and the $E_{adsorbate}$ is the energy of the VC or other small molecules under vacuum.

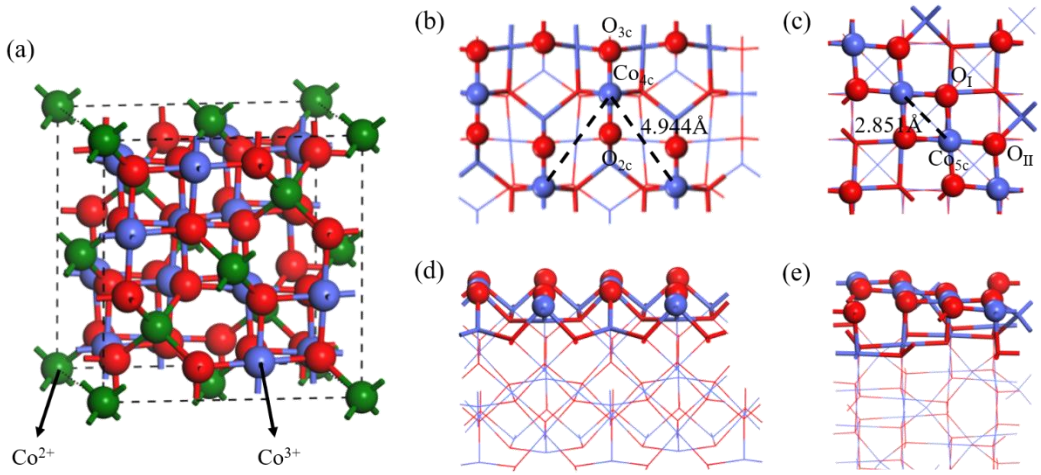

Fig. 2.3 (a) Unit cell of bulk Co_3O_4. (b) Top view and (d) side view of the Co_3O_4(110) surface. (c) Top view and (e) side view of the Co_3O_4(001) surface. Co and O atoms are shown in blue and red, respectively, expect for the Co^{2+} atoms in the bulk Co_3O_4, which are shown in dark green.

References

[1] J.P. Perdew, Y. Wang. Accurate and simple analytic representation of the electron-gas correlation energy. Physical Review B: Condensed Matter and Materials Physics. 1992, 45: 13244-13249.

[2] G. Kresse, J. Fruthmüller. Efficiency of ab-initio total calculations for metals and semiconductors using a plane-wave basis set. Computational Materials Science. 1996, 6(1): 15-50.

[3] G. Kresse, J. Hafner. Ab initio molecular-dynamics simulation of the liquid-metalamrphous-semiconductor transition in germanium. Physical Review B: Condensed Matter and Materials Physics. 1994, 49(20): 14251-14269.

[4] G. Kresse, D. Joubert. From ultrasoft pseudopotentials to the projector augmented-wave method. Physical Review B: Condensed Matter and Materials Physics. 1999, 59(3): 1758-1775.

[5] L. Hu, Q. Peng, Y. Li. Selective synthesis of Co_3O_4 nanocrystal with different shape and crystal plane effect on catalytic property for methane combustion. Journal of the American Chemical Society. 2008, 130(48): 16136-16137.

[6] H.F. Wang, R. Kavanagh, Y.L. Guo, Y. Guo, G. Lu, P. Hu. Origin of extraordinarily high catalytic activity of Co_3O_4 and its morphological chemistry for CO oxidation at low temperature. Journal of Catalysis. 2012, 296: 110-119.

[7] H.F. Wang, D. Wang, X. Liu, Y.L. Guo, G.Z. Lu, P. Hu. Unexpected C-C bond cleavage mechanism in ethylene combustion at low temperature: Origin and implications. ACS Catalysis. 2016, 6(8): 5393-5398.

[8] Z.P. Zhi, P. Hu. General Rules for predicting where a catalytic reaction should occur on metal surfaces: A density functional theory study of C-H and C-O bond breaking/making on flat, stepped and kinked metal surfaces. Journal of the American Chemical Society. 2003, 125(7): 1958-1967.

[9] A. Michaelides, P. Hu. Catalytic water formation on platinum: A first-principles study. Journal of the American Chemical Society. 2001, 123(18): 4235-4242.

[10] A. Alavi, P. Hu, T. Deutsch, P.L. Silvestrelli, J. Hutter. CO oxidation on Pt(111): An ab initio density functional theory study. Physical Review Letters. 1998, 80(16): 3650-3653.

[11] H.F. Wang, R. Kavanagh, Y.L. Guo, Y. Guo, G.Z. Lu, P. Hu. Structural origin: Water deactivates metal oxides to CO oxidation and promotes low-temperature CO oxidation with metals. Angewandte Chemie. 2012, 124(27): 6761-6765.

Chapter 3 The catalytic oxidation of VC over Co_3O_4 based on DFT

3.1 Introduction

Transition metal oxides have been attracting increasing attention in CVOCs oxidation for their Cl-poisoning tolerance, good catalytic activity and stability [1-7]. Co_3O_4 with spinel structure has been proved to be one of the most efficient catalysts for VOCs and CVOCs oxidation due to its low-temperature redox ability, high content of surface oxygen species and bulk oxygen mobility [8-9].

Recently, Miran and co-workers [10] investigated the reaction mechanism of VC oxidation on CeO_2 catalyst based on DFT calculations. Our previous experimental work [11] studied the morphological effect of Co_3O_4 crystallite on the catalytic oxidation of VC. The cubic Co_3O_4, with preferential exposure of (001) surface, was found to be the most active sample for VC oxidation. However, to the best of our knowledge, the atomic-level insight into the reaction mechanism of VC oxidation on Co_3O_4 has been rarely reported. There are still some puzzles which need to be clarified: (i) what is the overall reaction pathways of VC oxidation on Co_3O_4? (ii) what is the rate-determining step for VC oxidation on Co_3O_4? (iii) How can one efficiently improve the activity of Co_3O_4 via rational modulation strategy? Furthermore, crystal plane effect has been evidenced to play an important role for Co_3O_4 in several reactions [12-13]. Thus, it is requisite to rationalize the origin of the crystal plane effect of Co_3O_4 on VC oxidation.

Based on the previous work, the unsolved problems mentioned above will be discussed through DFT calculations. The reaction mechanism of VC oxidation on Co_3O_4 catalyst will be further studied, in order to provide some theoretical guidance for the design and preparation of Co_3O_4-based catalysts.

3.2 The reaction mechanism of VC oxidation over Co_3O_4.

The stable termination configuration of $Co_3O_4(110)$ surface has been verified with isolated four-coordinated Co_{4c} in the octahedral sites and two-/three-coordinated lattice oxygens (O_{2c}/O_{3c}) exposed under the common working conditions [12, 14]. Fig. 2.3b and 2.3d show the optimized surface structure of $Co_3O_4(110)$, from which one can see that the adjacent Co_{4c}-Co_{4c} distance on the (110) surface is very long (4.944 Å), indicating that the Co_{4c} sites are basically isolated [29]. Differently, the distance of the adjacent Co atoms on the $Co_3O_4(001)$ surface is 2.851 Å, implying that they could jointly play a role in the catalytic reaction. As depicted in Fig. 2.3c, the $Co_3O_4(001)$ surface exposes exclusively the five-coordinated Co_{5c} and two types of lattice O_{3c}, which constitute the basic active sites; one O_{3c} binds with three Co^{3+} (O_I), and the

other one binds with two Co^{3+} and one Co^{2+} (O_{II}).

For the CVOC molecule, the electronegativity of the Cl atom makes the polarity of C-Cl bond larger than the other C-H/C-C bonds. Consequently, the C-Cl bond is relatively easier to be activated, which has been widely accepted as the first step for catalytic oxidation of CVOCs [9, 15]. With these considerations, the reactions pathways of VC oxidation on Co_3O_4 can be divided into three subprocesses in Scheme 1: (i) the scission of C-Cl bond after VC adsorption on the Co_3O_4 surface, forming the adsorbed CH_2CH* and Cl* intermediates; (ii) the activation and oxidation of CH_2CH* by the oxidative species (lattice oxygen and adsorbed oxygen molecule); (iii) the elimination of Cl* through the generation of HCl or Cl_2.

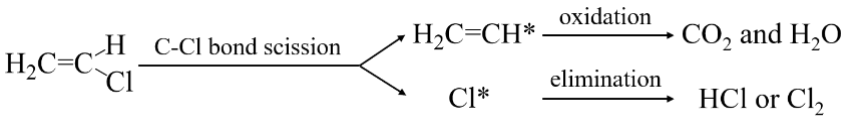

Fig. 3.1 Possible subprocesses involved in the VC oxidation on Co_3O_4.

3.2.1 C-Cl bond scission

To begin with, the adsorption of VC molecule on Co_3O_4(110) was calculated. VC prefers to adsorb at the surface Co^{3+} site in a π-adsorption configuration, and the chemisorption energy is -0.24 eV, implying the relatively weak adsorption of VC on the Co_3O_4(110) surface. Compared with the ethylene adsorption energy on Co_3O_4(110) (-1.18 eV), this weakened adsorption strength could be attributed to the steric repulsion effect of Cl with the neighboring lattice oxygens, and also the strong electron-attracting effect of Cl, which can decrease the electron density of C-C bond in the VC molecule. Then we considered the decomposition of VC on the stoichiometric Co_3O_4(110) surface. On the isolated Co_{4c} site, it corresponds to the C_2H_3* and Cl* co-adsorption after the C-Cl bond ruptures. The C-Cl bond is elongated to 2.280 Å at the transition state versus 1.721 Å in the initial adsorption state (Fig. 3.2). However, it was found that this reaction is endothermic by 1.02 eV and needs to overcome an activation barrier as high as 3.22 eV, indicating that the scission of C-Cl bond is not easy at relatively low temperature on stoichiometric Co_3O_4(110) surface.

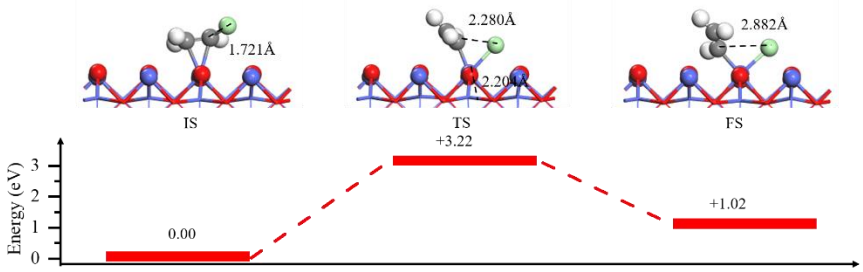

Fig. 3.2 The scission of C-Cl bond on the stoichiometric Co_3O_4(110) surface. H, C and Cl atoms are shown in white, gray and light green, respectively. The IS, TS and FS stand for initial, transition and final state, correspondingly.

According to the experimental results by many literatures [2, 4, 8], the actual surface Co^{2+}/Co^{3+} ratio of Co_3O_4 catalyst is higher than the stoichiometric value, which correlates with the presence of oxygen vacancies on the catalyst surface, namely partially reduced $Co_3O_4(110)$ surface (denoted as R-$Co_3O_4(110)$). Then, the possibility of C-Cl bond rupture was resorted to the participation of surface oxygen vacancies. Note that the O_{2c} site corresponds to a lower vacancy formation energy relative to the O_{3c} site, and could thus constitute the preferential defect site (V_{2c}). With an V_{2c} generated on $Co_3O_4(110)$, the original Co_{4c} site would turn into the less coordinated Co_{3c} site, which would become more reactive and have stronger ability to anchor the VC molecule. Accordingly, the chemisorption energy of VC at the Co^{3+} site nearest the O_{2c} vacancy was calculated to be -0.58 eV, higher than that on stoichiometric $Co_3O_4(110)$. Moreover, the C-Cl bond in the VC adsorption configuration is elongated to 1.744 Å on R-$Co_3O_4(110)$, suggesting the decreased C-Cl bond strength. Therefore, the C-Cl bond scission on the R-$Co_3O_4(110)$ surface can be expected more feasible.

Assisted by V_{2c}, the decomposition of VC on the R-$Co_3O_4(110)$ surface was then investigated. The optimized transition state and final state are shown in Fig. 3.3a. One can see that from this cleavage configuration, the oxygen vacancy plays a crucial role in accommodating the dissociated Cl species. In the transition state, the C-Cl bond is elongated to 2.159 Å to achieve the breaking. The barrier is decreased to be 1.53 eV and this process is exothermic by 0.34 eV, verifying the much facilitated C-Cl bond dissociation in comparison with the vacancy-free $Co_3O_4(110)$. The lower barrier could probably be elucidated by the geometric and electronic effects: on the stoichiometric $Co_3O_4(110)$ surface, the C_2H_3* and the Cl* would be competitively co-adsorbed on the same Co_{4c} site after the C-Cl bond scission, whereas the Cl* can be strongly trapped by V_{2c} on R-$Co_3O_4(110)$, leaving the C_2H_3* at the neighboring Co_{3c} site. Moreover, as V_{2c} forms on R-$Co_3O_4(110)$ surface, the electron density of the adjacent Co site would be enhanced as compared with that on the stoichiometric $Co_3O_4(110)$ surface. This electronic effect contributes to the adsorption of CH_2=CH* fragment and thus the lower barrier for the C-Cl bond scission on R-$Co_3O_4(110)$.

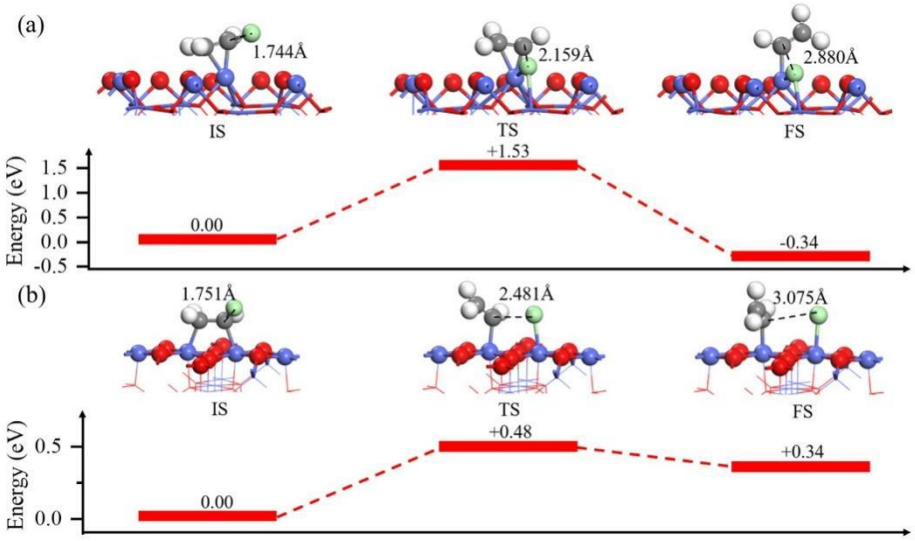

Fig. 3.3 The scission of C-Cl bond on (a) the R-Co_3O_4(110) surface and (b) the Co_3O_4(001) surface.

On Co_3O_4(001), the VC adsorption preferentially adopts a di-σ-bond configuration on two adjacent Co_{5c} sites as shown in Fig. 3.3b. The chemisorption energy was calculated to be -0.29 eV. This weak adsorption could be partially correlated with the higher bond saturability of the five-coordinated Co_{5c} site on Co_3O_4(001) than the Co_{4c} site on Co_3O_4(110). Then the possibility of the C-Cl bond scission on Co_3O_4(001) was examined, which indicates that the two adjacent Co_{5c} sites could synergistically break the C-Cl bond, with the CH_2CH* and Cl* species respectively adsorbed at each site. In the corresponding TS, the C-Cl bond is elongated to 2.481 Å and the C-Co_{5c} bond length is 2.204 Å. It gives an energy barrier as low as 0.48 eV, despite that it is endothermic by 0.34 eV. This low barrier suggests that the C-Cl bond scission on the Co_3O_4(001) surface is much more feasible than that on the Co_3O_4(110) surface.

3.2.2 CH_2CH oxidation

Regarding the conversion of CH_2CH* species resulting from VC de-chlorination on Co_3O_4(110), the C-C bond cleavage mechanism has been explored in our previous work [16]. As Fig. 3.4 shows, the valency-saturation-driven mechanism was identified for CH_2CH oxidation into CO2. Firstly, instead of breaking the C-H bond, CH_2CH* preferentially reacts with the lattice O_{3c} to form the CH_2CHO intermediate at a low barrier of 0.24 eV. By consecutive dehydrogenation (CH_2CHO → CH_2CO → CHCO), CH_2CHO can be then converted into CHCO, requiring the energy barriers of 0.68 eV and 0.52 eV, respectively. Secondly, CHCO could easily react with O_2 adsorbed in the O_{3c} vacancy to form CHOCO at a barrier of 0.30 eV, which can readily break the C-C bond into CHO* and CO* at the Co3+ site by overcoming a barrier as low as 0.14 eV. Finally, these formed C1 species could be easily converted to CO_2. It was evidenced that the C-C bond cleavage can be more feasibly accomplished when the C-end atom in the dissociated C1 species is stabilized by reaching the

valency saturation (i.e., CHO and CO). Following such a mechanism, it is feasible to accomplish the CH_2CH* oxidation on Co_3O_4(110) at low temperature.

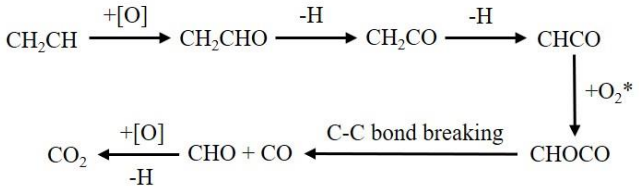

Fig. 3.4 Proposed reaction mechanism for CH_2CH oxidation.

Herein, this mechanism for CH_2CH* oxidation is also examined on the Co_3O_4(001) surface, as Fig. 3.5 illustrates. As described above, there are two types of lattice oxygen on Co_3O_4(001), i.e., O_I and O_{II}. It was found that CH_2CH* can react with the neighboring O_I or O_{II} to form CH_2CHO. For O_I that bonds with three Co^{3+}, the barrier is 0.51 eV, while it is a little more difficult for CH_2CH* to react with O_{II} that bonds with two surface Co^{3+} and one subsurface Co^{2+} at a barrier of 0.73 eV. This finding is analogous with CO oxidation on Co_3O_4(001), and the origin of the higher reactivity of O_I versus O_{II} toward CH_2CH* can be traced to the different coordination environment. Overall, it is evident that CH_2CH* can be easily oxidized into CH_2CHO by the lattice oxygen on Co_3O_4(001), according with the fact that Co_3O_4(001) exhibits good redox properties for CO oxidation [12]. Then, CH_2CO can be formed via the dehydrogenation of acyl-H in CH_2CHO, which is largely exothermic by 1.04 eV and gives a barrier of 0.68 eV. CH_2CO could further dissociate into CHCO through breaking the α-H atom with a barrier of 0.33 eV. From the energy profiles, we can see that the conversion of CH_2CHO to CHCO on Co_3O_4(001) is relatively easy to proceed following the same acetyl pathway as that on Co_3O_4(110).

Note that, with the CHCO formation, the oxygen vacancy will be generated at the O_I site, which must be replenished before further oxidation of CHCO. It was found that O_2 can efficiently adsorb in the O_I vacancy with a side-on configuration, which gives an adsorption energy of -0.77 eV, guaranteeing the presence of surface O_2*. Significantly, CHCO can easily react with O_2* to form CHOCO with a low barrier of 0.24 eV and it is extremely exothermic by 2.38 eV. Remarkably, CHOCO can readily break its C-C bond into CHO* and CO* by two adjacent Co_{5c} sites, which requires a barrier of only 0.35 eV. Once formed, CHO* and CO* can be easily converted to CO_2. Specifically, CO can easily react with the lattice O_I at a barrier of 0.58 eV, as demonstrated by Wang et al. [12]. For CHO*, it can either dissociate into CO* with a barrier of 0.78 eV or react with O_I to form the formate (HCOO) intermediate at a barrier of 0.38 eV, which can then dissociate into CO_2. Fig. 3.5 shows the energy profile of this overall process, revealing that the reaction pathway of CH_2CH oxidation on Co_3O_4(110) is

energetically plausible on Co_3O_4(001), and thus CH_2CH oxidation can proceed readily on the Co_3O_4(001) surface.

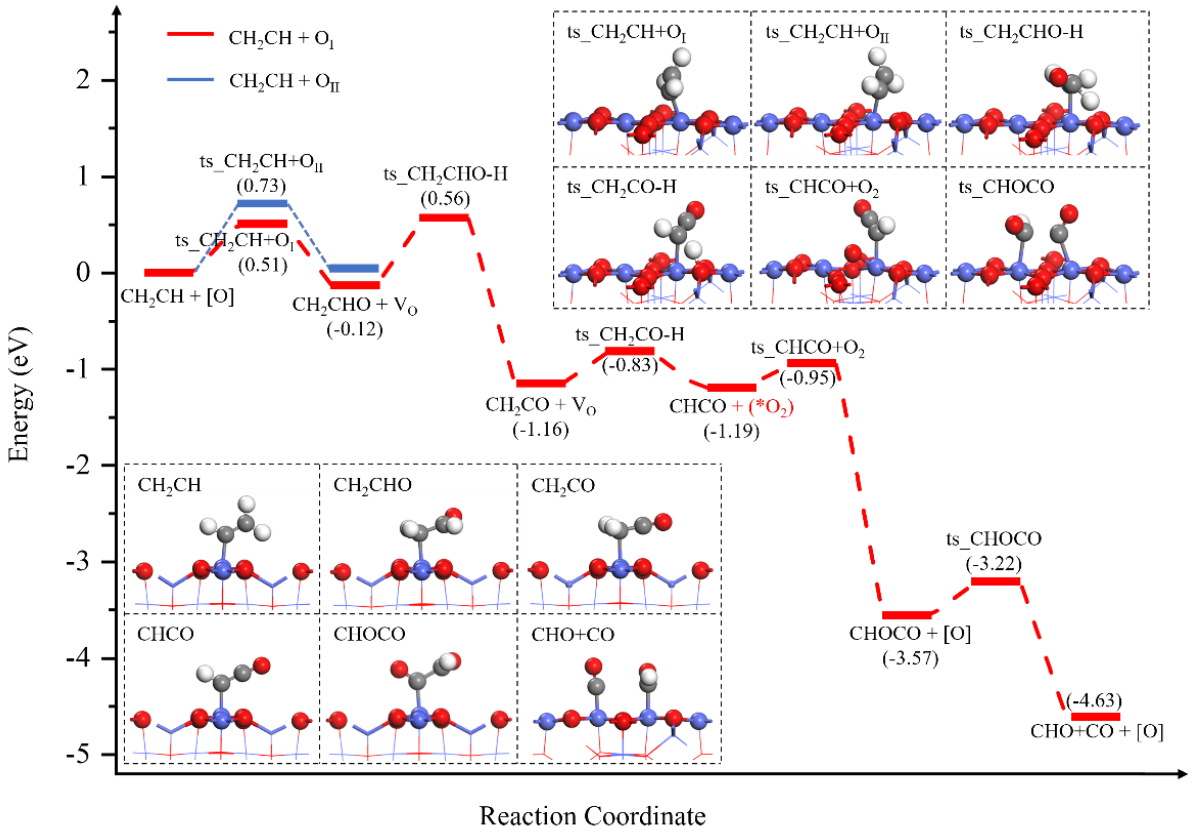

Fig. 3.5 Energy profiles for CH_2CH conversion into CHO + CO on Co_3O_4(001) through the oxidation-cracking mechanism. Insets show the optimized structures of the key intermediate and the transition states of some key reactions involved in the CH_2CH oxidation.

3.2.3 Cl elimination

According to the experimental results, HCl and Cl_2 are usually the final chlorine-containing product in CVOCs oxidation. Herein, we quantitatively calculated the energetics of the elimination of adsorbed Cl species to form HCl/Cl_2 products on the Co_3O_4 catalyst. On Co_3O_4(110), the Cl* adsorbed at the V_{2c} site was found to relatively difficult to couple with the H atom on the neighboring $O_{2c}H$ to produce HCl. It needs to overcome an energy barrier of 1.85 eV, and is largely endothermic by 1.58 eV. In the optimized transition state (Fig. 3.6), the O_{2c}-H bond is elongated as long as 2.487 Å and the forming Cl-H bond is 1.305 Å, exhibiting a very late-type TS. With respect to the Cl_2 formation via Cl-Cl coupling reaction on Co_3O_4(110), it was found the energy in searching the transition state by controlling Cl-Cl bond length is ever-increasing until forming the Cl_2 molecule, indicating that its inverse reaction is almost a barrierless process in the landscape of total energy. It gives a barrier as high as 2.61 eV. Therefore, the production of HCl is predicted to be relatively more feasible than Cl_2 formation on Co_3O_4(110). Nevertheless, the elimination of adsorbed Cl* species into either HCl

or Cl_2 is much more difficult in comparison with the C-Cl bond scission and CH_2CH oxidation subprocess on Co_3O_4(110). In addition to the high barrier, it is worth particularly emphasizing that the inverse reactions for both the HCl and Cl_2 formation are energetically much easier to proceed than the forward reaction, which constitutes one key factor leading to the difficult Cl elimination in reality. The inherent origin can be traced to the relatively weak H-Cl and Cl-Cl bond strength in HCl and Cl_2 molecule, respectively.

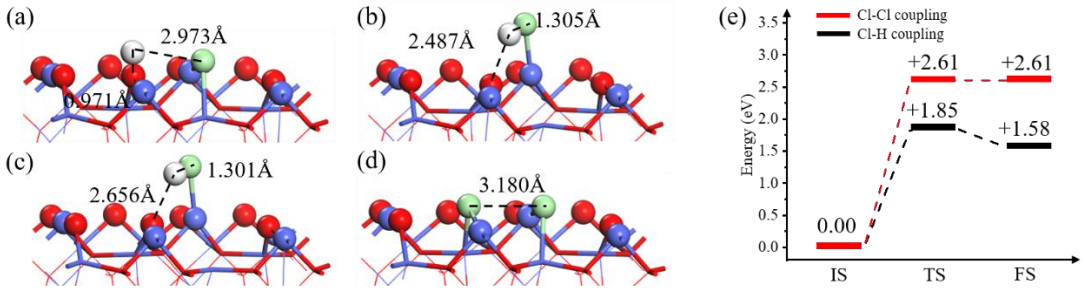

Fig. 3.6 (a-c) correspond to the initial state, transition state and final state, respectively, for the Cl-H coupling reaction on the R-Co_3O_4(110) surface. (d) illustrates the initial state of Cl-Cl coupling reaction on R-Co_3O_4(110), and (e) shows the energy profiles of HCl and Cl_2 formation.

For comparison, the elimination reaction of the adsorbed Cl species via forming HCl or Cl_2 was investigated on the Co_3O_4(001) surface. The calculation results show that Cl-H coupling on Co_3O_4(001) gives a barrier of 1.26 eV, and the enthalpy change is 1.11 eV. The transition state (Fig. 3.7) also corresponds to a late-TS type, where the O_{II}-H bond is elongated to 2.140 Å and the forming Cl-H bond is 1.307 Å. By contrast, the barrier of Cl_2 evolution via Cl-Cl coupling is 1.74 eV. This indicates that HCl formation keeps the primary reaction on Co_3O_4(001) relative to the Cl-Cl coupling. Notably, in comparison with Co_3O_4(110), the barrier of HCl formation on Co_3O_4(001) is evidently decreased, which could be attributed to the weak bond strength of H-O_{II} and Cl-Co_{5c} owing to the more saturated coordination environment of the Co_{5c} and O_{II} sites.

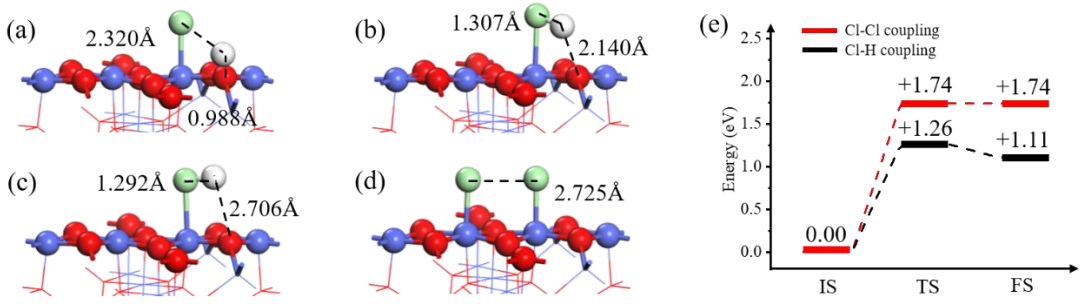

Fig. 3.7 (a-c) correspond to the initial state, transition state and final state, respectively, for the Cl-H coupling reaction on the Co_3O_4(001) surface. (d) illustrates the initial state of Cl-Cl coupling reaction on Co_3O_4(001), and (e) shows the energy profiles of HCl and Cl_2 formation.

3.3 General discussions

Fig. 3.8 compares the energy barriers of the key processes involved in the VC oxidation on Co_3O_4(110) and Co_3O_4(001), including (i) C-Cl bond cleavage, (ii) CH_2CH oxidation and (iii) Cl elimination via forming HCl or Cl_2. Firstly, the C-Cl bond cleavage is relatively easier on Co_3O_4(001) than that on Co_3O_4(110), in which the collaboration of two adjacent Co_{5c} on Co_3O_4(001) was proved to play significant roles. Secondly, it was evidenced that the catalytic activity of CH_2CH oxidation on Co_3O_4(001) is comparable with that on Co_3O_4(110) by comparing the highest energy barrier of these elementary steps on both surfaces. Thirdly, owing to the strong trapping ability of the oxygen vacancy toward the Cl atoms on Co_3O_4(110), the elimination of Cl species from the catalyst surface corresponds to the rate-determining step in the whole process, limiting the overall activity of Co_3O_4(110) for VC oxidation at relatively low temperature. Similarly, on the Co_3O_4(001) surface, the Cl elimination was also identified as the most difficult step for VC oxidation. Remarkably, one can see that the Cl elimination process, through forming either HCl or Cl_2, is significantly more facile on Co_3O_4(001) compared with Co_3O_4(110). Therefore, we can conclude that the Co_3O_4(001) surface is more conductive for VC oxidation than the Co_3O_4(110) surface, which benefits from the collaborative effect of the neighboring Co_{5c} sites on the surface, the excellent oxidation ability, and the relative easiness of Cl elimination from the surface.

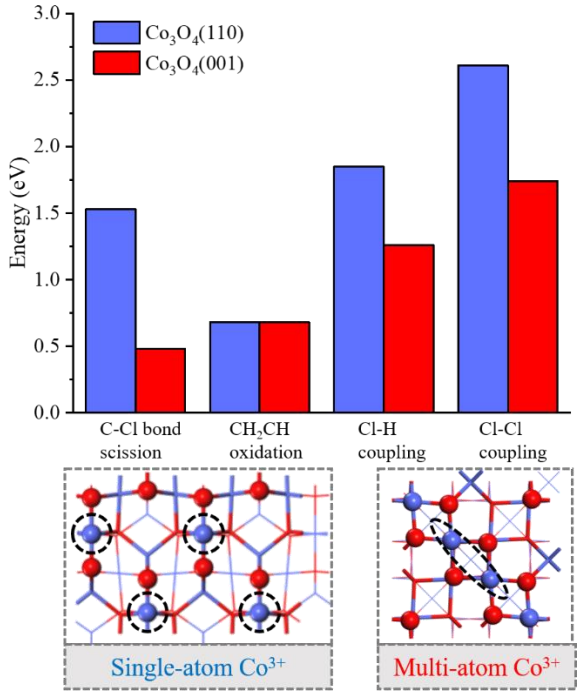

Fig. 3.8 The comparison of energy barriers of VC oxidation on Co_3O_4(110) and Co_3O_4(001). Note that for CH_2CH oxidation the highest barriers among the elementary steps are compared here.

As the Cl elimination constitutes the rate-determining step in the overall VC oxidation, there would exist the aggregation of Cl atoms on the Co_3O_4 surface accordingly, which results

in the blocking of the active sites to some extent. López and co-workers [17] reported the different coverage of O and Cl atoms on RuO_2(110) would affect the recombination of two Cl atoms. Herein, under the realistic condition, the effect of excess Cl and O atoms on the Cl-Cl coupling reaction on the Co_3O_4(001) surface is thus worth discussing. As shown in Fig. 3.9, the desorption energy of 1.78 eV was found with two Cl atoms at the neighboring Co_{5c} sites (corresponding to the situation with a high coverage of Cl species), which changes little compared with that (1.74 eV) on the pristine Co_3O_4(001); interestingly, the presence of O adatoms can significantly lower the energy required for Cl-Cl coupling (from 1.74 eV to 0.84 eV). This finding implies that the poisoned Co_3O_4 catalyst could be refreshed by a thermal treatment under oxygen atmosphere. Perhaps in another way, one can properly increase the feed O_2/VC ratio, which could be beneficial for the increase of O coverage on the surface at higher O_2 partial pressure and the lower energy demand for Cl removal. With this method, the Cl-poisoning effect would be weakened, and the catalytic activity of Co_3O_4 for VC oxidation could be facilitated.

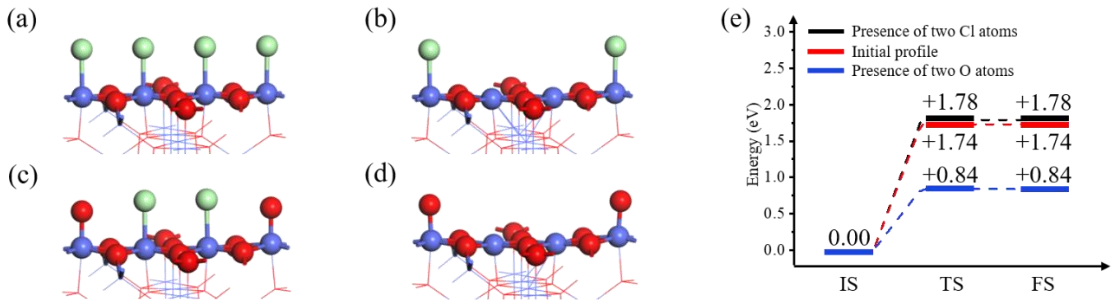

Fig. 3.9 The initial states of Cl-Cl coupling on Co_3O_4(001) in the presence of (a) two Cl atoms or (c) two O atoms at the neighboring Co sites. (b) and (d) correspond to the surfaces after Cl_2 release, respectively. (e) gives the energy profiles of Cl elimination under different conditions on Co_3O_4(001).

In addition, with the obtained insight, one may speculate that increasing the surface Brønsted acidity in the catalyst design/preparation can result in the enhancement of the proton supply and thus promote HCl formation. In other word, by such treatments the elimination of the Cl species from Co_3O_4 the surface would be accelerated, which accords with the experimental fact that increasing the surface acidity of the catalysts can commonly improve the catalytic performance of CVOC oxidation [15].

3.4 Conclusions

In this chapter, the reaction mechanism of VC oxidation over Co_3O_4 was systematically explored. The reaction pathways of VC oxidation were thoroughly calculated from the molecular scale. The rate-determining step in the overall VC oxidation was identified. The crystal plane effect on the catalytic performance was studied. Finally, some propositions were

made for how to improve the VC oxidation on Co_3O_4 catalysts. The following conclusions are drawn：

1. VC oxidation on Co_3O_4 mainly consists of three subprocesses, including the C-Cl bond scission, CH_2CH oxidation and Cl species elimination. The CH_2CH and Cl species formed after C-Cl bond scission are the reactants of the second and third parts respectively.

2. The oxygen vacancy is indispensable to the cleavage of C-Cl bond on Co_3O_4(110), while the C-Cl bond scission can be easily achieved through the collaboration of two adjacent Co_{5c} sites on the Co_3O_4(001) surface.

3. Compared with Co_3O_4(110), Co_3O_4(001) shows very good activity for the catalytic oxidation of CH_2CH group due to its excellent oxidation ability, and the overall performance is equivalent to that of Co_3O_4(110) for the catalytic oxidation of CH_2CH group.

4. The elimination of Cl species is the rate-determining step in the whole process, and it is easier to produce HCl rather than Cl_2 on both surfaces. On comparing the overall activity of (110) and (001) surfaces of Co_3O_4, (001) is theoretically identified to be the preferable surface for VC oxidation, rationalized from its higher Cl elimination ability.

5. Finally, based on these computational insights, some propositions are made. one can properly increase the feed O_2/VC ratio to lower the barrier for Cl removal and facilitate the catalytic activity of Co_3O_4 for VC oxidation. The poisoned Co_3O_4 catalyst could be refreshed by a thermal treatment under oxygen atmosphere. One can also increase the surface Brønsted acidity in the catalyst design/preparation to enhance the proton supply, thus promoting the HCl formation and Cl elimination and further improving the catalytic performance of Co_3O_4.

References

[1] W. Deng, Q. Tang, S. Huang, L. Zhang, Z. Jia, L. Guo. Low temperature catalytic combustion of chlorobenzene over cobalt based mixed oxides derived from layered double hydroxides. Applied Catalysis B: Environmental. 2020, 278: 119336.

[2] T. Cai, H. Huang, W. Deng, Q. Dai, W. Liu, X. Wang. Catalytic combustion of 1,2-dichlorobenzene at low temperature over Mn-modified Co_3O_4 catalysts. Applied Catalysis B: Environmental. 2015, 166-167: 393-405.

[3] C. Wang, C. Zhang, W. Hua, Y. Guo, G. Lu, S. Gil, A. Giroir-Fendler. Low-temperature catalytic oxidation of vinyl chloride over Ru modified Co_3O_4 catalysts. RSC Advances. 2016, 6(101): 99577-99585.

[4] C. Wang, C. Zhang, W. Hua, Y. Guo, G. Lu, S. Gil, A. Giroir-Fendler. Catalytic oxidation of vinyl chloride emissions over Co-Ce composite oxide catalysts. Chemical Engineering Journal. 2017, 315: 392-402.

[5] G. Li, C. Zhang, Z. Wang, H. Huang, H. Peng, X. Li. Fabrication of mesoporous Co_3O_4 oxides by acid treatment and their catalytic performances for toluene oxidation. Applied Catalysis A, General. 2018, 550: 67-76.

[6] W. Zhang, F. Wu, J. Li, Z. You. Dispersion-precipitation synthesis of highly active nanosized Co_3O_4 for catalytic oxidation of carbon monoxide and propane. Applied Surface Science. 2017, 411: 136-143.

[7] W. Hu, J. Lan, Y. Guo, X.M. Cao, P. Hu. Origin of efficient catalytic combustion of methane over Co_3O_4(110): Active low-coordination lattice oxygen and cooperation of multiple active sites. ACS Catalysis. 2016, 6(8): 5508-5519.

[8] J. González-Prior, R. López-Fonseca, J.I. Gutiérrez-Ortiz, B. de Rivas. Oxidation of 1,2-dichloroethane over nanocube-shaped Co_3O_4 catalysts. Applied Catalysis B: Environmental. 2016, 199: 384-393.

[9] M. Tian, C. He, Y. Yu, H. Pan, L. Smith, Z. Jiang, N. Gao, Y. Jian, Z. Hao, Q. Zhu. Catalytic oxidation of 1,2-dichloroethane over three-dimensional ordered meso-macroporous $Co_3O_4/La_{0.7}Sr_{0.3}Fe_{0.5}Co_{0.5}O_3$: Destruction route and mechanism. Applied Catalysis A, General. 2018, 553: 1-14.

[10] H.A. Miran, M. Altarawneh, Z.T. Jiang, H. Oskierski, M. Almatarneh, B.Z. Dlugogorski. Decomposition of selected chlorinated volatile organic compounds by ceria (CeO_2). Catalysis Science & Technology. 2017, 7(17): 3902-3919.

[11] C. Wang, W. Hua, G. Chai, C. Zhang, Y. Guo. Insights into the morphological effect of Co_3O_4 crystallite on catalytic oxidation of vinyl chloride. Catalysts. 2019, 9(5): 408.

[12] H.F. Wang, R. Kavanagh, Y.L. Guo, Y. Guo, G. Lu, P. Hu. Origin of extraordinarily high catalytic activity of Co_3O_4 and its morphological chemistry for CO oxidation at low temperature. Journal of Catalysis. 2012, 296: 110-119.

[13] Y. Wang, X. Yang, L. Hu, Y. Li, J. Li. Theoretical study of the crystal plane effect and ion-pair active center for C-H bond activation by Co_3O_4 nanocrystals. Chinese Journal of Catalysis. 2014, 35(4): 462-467.

[14] H.F. Wang, R. Kavanagh, Y.L. Guo, Y. Guo, G.Z. Lu, P. Hu. Structural origin: Water deactivates metal oxides to CO oxidation and promotes low-temperature CO oxidation with metals. Angewandte Chemie. 2012, 124(27): 6761-6765.

[15] P. Yang, S. Fan, Z. Chen, G. Bao, S. Zuo, C. Qi. Synthesis of Nb_2O_5 based solid superacid materials for catalytic combustion of chlorinated VOCs. Applied Catalysis B: Environmental. 2018, 239: 114-124.

[16] H.F. Wang, D. Wang, X. Liu, Y.L. Guo, G.Z. Lu, P. Hu. Unexpected C-C bond cleavage mechanism in ethylene combustion at low temperature: Origin and implications. ACS Catalysis. 2016, 6(8): 5393-5398.

[17] N. López, J. Gómez-Segura, R.P. Marín, J. Pérez-Ramríez. Mechanism of HCl oxidation (Deacon process) over RuO_2. Journal of Catalysis. 2008, 255(1): 29-39.

Chapter 4 The preparation and catalytic performance of the Zr-modified Co_3O_4 catalysts

4.1 Introduction

VOCs are one of the main exhausts from industrial processes and transportation activities. Over the past decades, researchers have developed several different technologies to abate VOCs. Among them, catalytic oxidation has been regarded as a promising method to reduce the emissions of VOCs due to its high efficiency and low cost under relatively moderate operation conditions [1-4]. Transition metal oxides are attracting increasing attentions for VOCs removal for their low cost, high thermal stability, easy availability and noticeable low-temperature activity, such as MnO_x-CeO_2 [5]、CuO-CeO_2/Al_2O_3 [6]、xMn1Fe [7]、$NiCeO_x$ [8]和 Co_3O_4-CeO_2 [9].

Co_3O_4 is one of the most extensively used transition metal oxides in different oxidation reactions [10-15]. Wang and co-workers [16] found that CO complete oxidation could be achieved at -78 °C on pure Co_3O_4 and the amount of active oxygen species played a critical role for the catalytic activity. Bai and co-workers [17] compared the different performances of nano-Co_3O_4, 2D-Co_3O_4 and 3D-Co_3O_4 catalysts for formaldehyde oxidation and found that active oxygen species and high concentration of Co^{3+} cationic species on the surface of 3D-Co_3O_4 were beneficial to formaldehyde oxidation. The catalytic performance of Co_3O_4 could be further improved by doping with other non-noble metal elements, which could result in the activation of surface oxygen species and the promotion of lattice oxygen mobility. Lou and co-workers [18] found that CO could be oxidized to CO_2 over In_2O_3-Co_3O_4 catalysts (25 InCo, namely 25% In_2O_3 was doped) at a temperature as low as -105 °C by tuning the adsorption strength of CO and oxygen activation simultaneously. Wang and co-workers [19] demonstrated the promoting effect of cerium to the catalytic activity of Co_3O_4 for vinyl chloride oxidation by increasing the presence of Co^{2+} species, the oxygen vacancies and the oxygen mobility. The highest catalytic activity and stability was achieved when the molar ratio of Ce/(Ce + Co) was 0.3.

Zirconium oxide (ZrO_2) has been applied in various formulations as a support or promoter of catalysts in order to improve their amphoteric properties and thermal stability [20-25]. Pu and co-workers [26] applied ZrO_2 in the modification of Co_3O_4 catalysts for lean methane combustion and found that the substitution of Co^{3+} by Zr ions enlarged the SSA, increased the Co^{2+} concentration and surface-active oxygen species, which further enhanced the performance of ZrO_2-Co_3O_4 catalysts.

In this chapter, the modification effect of Zr on the Co_3O_4 catalyst was investigated. Firstly, a series of Zr-modified Co_3O_4 catalysts (the molar ratio of Zr/(Zr + Co) were 5%, 10% and 20%) were prepared using the sol-gel method and investigated for the total oxidation of VC. After that, XRD, Raman, SEM, N_2-sorption, H_2-TPR, NH_3-TPD and XPS et al. were used to systematically characterize the physicochemical properties of the catalysts, such as crystal phase, crystallite size, morphology, specific surface area, reducibility, surface acidity and surface composition. The relationship between the structure and catalytic performance of the catalysts were correlated effectively.

Then, another series of Zr-doped Co_3O_4 catalysts with the molar ratio, Zr/(Zr + Co), less than 2% were prepared by a simple sol-gel method and applied in the total oxidation of propane. Several techniques were used to characterize the synthesized catalysts, so as to explore the effect of Zr doping content on the physicochemical properties and catalytic performance, as well as establish a structure-activity relationship. Stability tests for propane oxidation were performed over the most active catalyst.

4.2 The catalytic performance of the Zr-modified Co_3O_4 catalysts for VC oxidation

4.2.1 Preparation of catalysts

Zr-modified Co_3O_4 catalysts were prepared by the citrate sol-gel method. Cobalt nitrate and zirconyl nitrate, with different molar ratio of Co/Zr, were dissolved in a certain amount of water. Then citric acid (CA) and polyglycol were added into the above solution. The molar ratio of CA/(Co + Zr) was 1.1:1 and the weight amount of polyglycol was 5% of the CA weight. The mixture was heated up to 80 °C and kept at this temperature under stirring until the gel was formed. The gel was placed in a 110 °C oven overnight and then the spongelike precursor was obtained. It was further calcined at 500 °C for 4h under static air in a muffle furnace. The obtained Zr-modified catalysts were denoted as Co_xZr_y, where x and y represented the molar percentage composition and x + y = 100. Pure Co_3O_4 catalyst and ZrO_2 catalyst were prepared using the same method.

4.2.2 Evaluation of catalysts

The catalyst evaluation method is described in Chapter 2, Section 2.5.1.

4.2.3 Characterization of catalysts

After obtaining the catalysts, the real content of Zr in the catalyst was measured by ICP, and the experimental results are listed in Table 4.1.

(1) XRD

Fig. 4.1 showed the XRD patterns of the catalysts. The diffraction peaks of pure Co_3O_4, which were located at 2θ 19.0°, 31.3°, 36.8°, 44.8°, 59.3° and 65.2°, could correspond to pure cubic phase of Co_3O_4 spinel (PDF # 42-1467). For ZrO_2 catalyst, it showed a mixture of

monoclinic oxide structure (PDF # 50-1089) and tetragonal oxide structure (PDF # 37-1484). The diffraction peaks of 2θ 30.2°, 34.5°, 35.3°, 50.4°, 60.2°, 62.8° and 74.8° corresponded to the tetragonal phase of ZrO_2, and the diffraction peaks of 2θ 24.3°, 28.3°, 31.4°, 40.7°, 44.7°, 54.2°, 55.6° and 65.8° were ascribed to the monoclinic phase of ZrO_2. It was found that only diffraction peaks of Co_3O_4 were observed on catalysts of $Co_{95}Zr_5$, $Co_{90}Zr_{10}$ and $Co_{80}Zr_{20}$, which indicates that the zirconium could be doped into Co_3O_4 spinel structure, or maybe it was highly dispersed on the Co_3O_4 surface. In addition, it could be observed the diffraction peaks of Co_3O_4 became broader and weaker with the introduction of zirconium, which indicated the decrease in the degree of crystallization and the smaller crystalline size. The average crystalline sizes of Co_3O_4 spinel particles, as shown in Table 4.1, were calculated based on Scherrer formula.

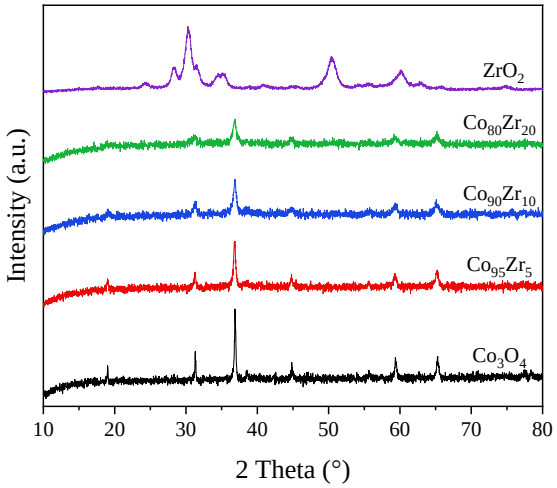

Fig. 4.1 XRD patterns of the synthesized Co_xZr_y catalysts.

(2) N_2-sorption

Fig. 4.2 showed the N_2 -sorption isotherms of the catalysts. The specific surface area, the average pore size and the pore volume were illustrated in Table 4.1. The results showed that all the samples exhibited type IV isotherm, indicating the presence of mesoporous in the samples. The introduction of Zr into Co_3O_4 could increase the specific surface area, which suggested smaller crystalline size of Co_3O_4 and was consistent with the results from XRD. The average pore size and pore volume of the Zr-modified catalysts were between pure Co_3O_4 and ZrO_2 catalysts. With the increase of the Zr amount, the pore size became smaller, so as the pore volume. Above all, it revealed that the introduction of Zr had an inhibitory effect on the growth of the crystalline Co_3O_4.

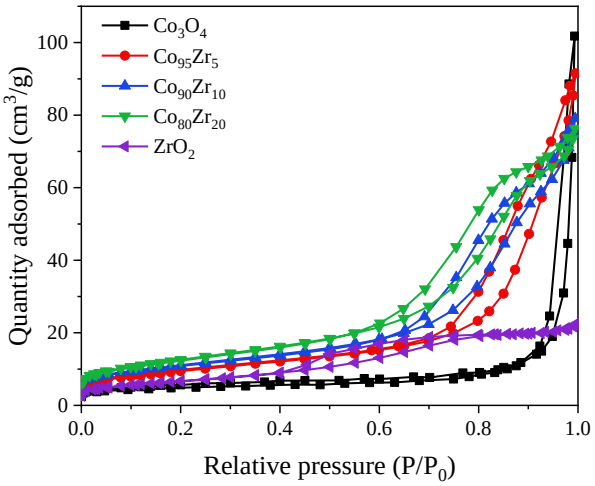

Fig. 4.2 N_2 adsorption-desorption isotherms of the synthesized Co_xZr_y catalysts.

Table 4.1 Physicochemical properties of the synthesized Co_xZr_y catalysts.

Catalyst	Zr (wt. %)	d (nm)	SSA ($m^2\ g^{-1}$)	Average pore size (nm)	V_{pore} ($cm^3\ g^{-1}$)	Acidity (mmol $NH_3\ g^{-1}$)		
						Total	Weak	Medium and strong
Co_3O_4	/	39.3	19	32	0.157	0.036	0.036	/
$Co_{95}Zr_5$	3.5	24.2	33	16	0.142	0.087	0.075	0.012
$Co_{90}Zr_{10}$	7.0	19.2	39	12	0.122	0.076	0.062	0.014
$Co_{80}Zr_{20}$	14.0	15.4	44	10	0.118	0.123	0.076	0.047
ZrO_2	/	/	24	5	0.035	0.069	/	/

(3) SEM

In order to intuitively observe the morphology and the Co_3O_4 particle size of the catalysts, Co_3O_4 and $Co_{95}Zr_5$ were characterized by SEM, as shown in Fig. 4.3. From the results, it can be seen that the two samples both showed a certain degree of sintering, manifested as the condensed blocky structure. The sintering of Co_3O_4 nanoparticles for pure Co_3O_4 was very serious. While the degree of sintering declined obviously after the incorporation of zirconium. The Co_3O_4 particle size was also largely reduced, which could be consistent with the XRD results. With the decrease of the particle size, the specific surface area generally would increase, this could also agree with the N_2-sorption experiments results.

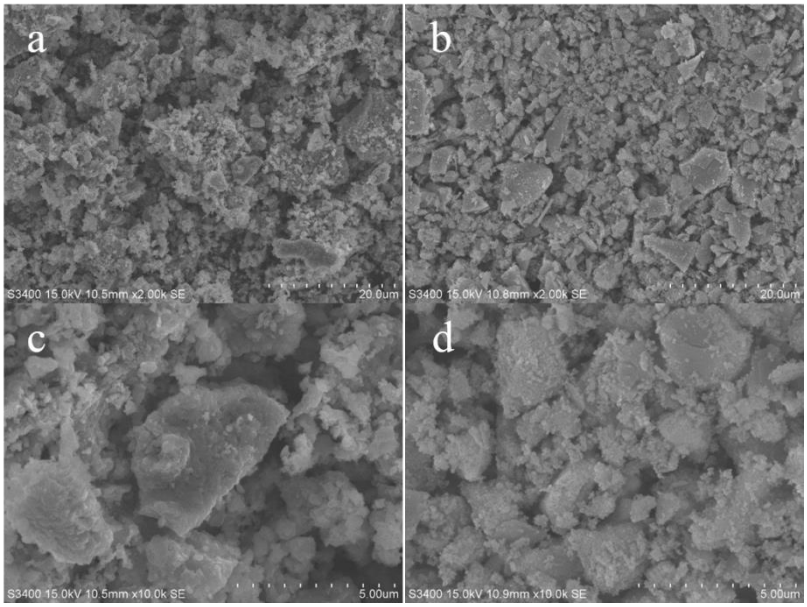

Fig. 4.3 SEM images of (a, c) pure Co_3O_4 and (b, d) $Co_{95}Zr_5$ catalysts.

(4) H_2-TPR

H_2-TPR measurement was used to investigate the redox property of the catalysts. The H_2-TPR profiles were showed in Fig. 4.4. Pure Co_3O_4 showed a broad reduction peak, which could be divided into two reduction peaks. The first peak corresponded to the reduction of Co^{3+} to Co^{2+} and the second peak was associated with the reduction of Co^{2+} to Co^0 [27]. The H_2-consumption of the Co_3O_4 catalyst calculated from the H_2-TPR profile was lower than the theoretical value, indicating that there were more Co^{2+} existing in the structure than expected and suggesting the presence of oxygen vacancies on the surface. The similar findings were observed for $Co_{95}Zr_5$ and $Co_{90}Zr_{10}$ catalysts. ZrO_2 showed no reduction peak in the investigated temperature range, which suggested that it could not be reduced and would rarely show activity to the oxidation of VC. Regarding the catalysts of $Co_{95}Zr_5$, $Co_{90}Zr_{10}$ and $Co_{80}Zr_{20}$, the reduction peak of Co^{3+} to Co^{2+} shifted to lower temperature compared with that of pure Co_3O_4 (Table 4.2), indicating the introduction of Zr improved the low-temperature reducibility of cobalt oxide. The best reducibility was achieved on $Co_{95}Zr_5$ catalyst. And for all zirconium-doped catalysts, a new small reduction peak appeared at a relatively high temperature (~ 600 °C), which might be attributed to the oxygen species in the structure of Co-Zr-O. This kind of oxygen species was difficult to be reduced. Therefore, one could deduce that excessive amount of zirconium would do harm to the reducibility of the catalyst. The reduction of Co-Zr-O in Co_xZr_y could explain the phenomenon that the H_2-consumption of $Co_{80}Zr_{20}$ was higher than the theoretical values.

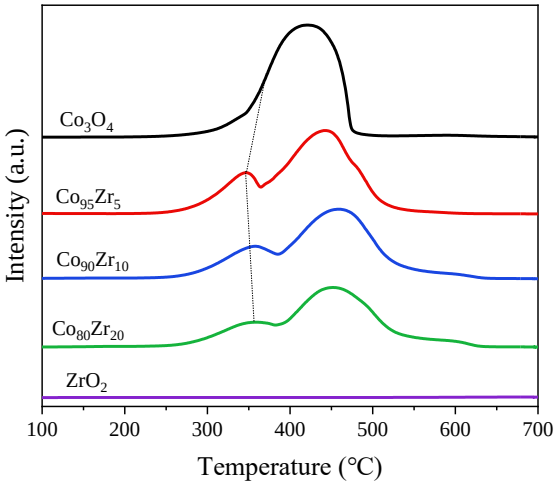

Fig. 4.4 H_2-TPR profiles of the synthesized Co_xZr_y catalysts.

(5) NH_3-TPD

The NH_3-TPD technique was used to evaluate the surface acid property of the catalysts, and the results were illustrated in Fig. 4.5. According to the results of Chapter 3, the cleavage of the C-Cl bond becomes the first step of VC oxidation. The C-Cl bond could be easier to be adsorbed, activated and dissociated by improving the surface acidity of the catalysts [28-29]. Pure Co_3O_4 exhibited nearly no acidity on the surface, whereas the other catalysts all showed an amount of acidity. The peaks below 200 °C were associated with the weak acid sites, whereas the peaks higher than 200 °C could correspond to the medium and strong acid sites. Pure Co_3O_4 has only a very small amount of weak acid sites, and other catalysts all show a certain amount of surface acidity. The total acidity of Zr-modified Co_3O_4 catalysts are higher than that of pure Co_3O_4 and ZrO_2 catalyst. The introduction of Zr mainly increased the surface weak acidity of the catalysts.

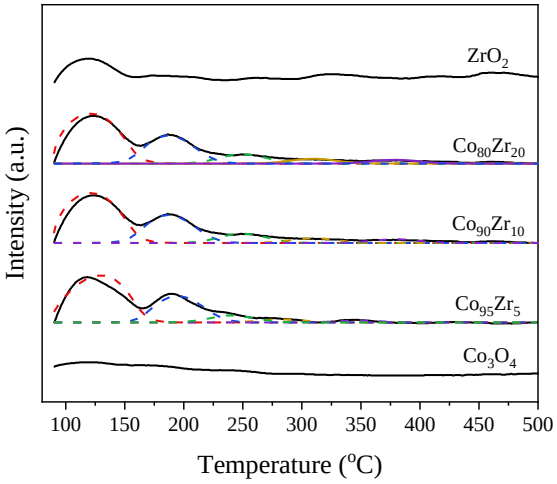

Fig. 4.5 NH_3-TPD profiles of the synthesized Co_xZr_y catalysts.

(6) XPS

XPS investigation was conducted to evaluate the surface chemical composition and the element states. Fig. 4.6 showed the XPS spectra of Co 2p and O 1s of the catalysts. As shown

in Fig. 4.6a, the Co 2p XPS spectra displayed two intense bands around the binding energies of 779.4 eV and 794.9 eV, corresponding to Co $2p_{3/2}$ and Co $2p_{1/2}$ spin-orbit peaks of spinel Co_3O_4 [1, 15]. The Co $2p_{3/2}$-Co $2p_{1/2}$ spin-orbit splitting energy of 15.5 eV was similar to the values in the literatures [26, 30]. Furtherly, the Co 2p spectra was deconvoluted. Each spin-orbit splitting peak could be deconvoluted into two peaks, accompanied by the appearance of satellite peaks. Since the Co $2p_{3/2}$ and the Co $2p_{1/2}$ peaks could supply the same information, only the Co $2p_{3/2}$ band was analyzed. The peaks around 779.5 eV and 781.1 eV were ascribed to Co^{3+} and Co^{2+}, respectively [19]. The surface atomic ratio of Co^{2+}/Co^{3+} are listed in Table 4.2. The ratio of Co^{2+}/Co^{3+} over all zirconium-modified catalysts were higher than that of the pure Co_3O_4 catalyst, and the catalyst $Co_{95}Zr_5$ had the highest Co^{2+}/Co^{3+} ratio. The higher Co^{2+} amount might also be related to more oxygen vacancies on the surface, which was beneficial for the formation of active oxygen species and the oxygen mobility.

The O 1s spectra of all the catalysts could be decomposed into two peaks, as shown in Fig. 4.6b. The one with a binding energy around 529.8 eV was associated with the lattice oxygen (O_{latt}), whereas the other one with a binding energy around 531.4 eV represented the surface adsorbed oxygen and oxygen-containing species (O_{ads}) [19]. The O_{ads} species was usually related with the active oxygen species on the catalyst surface. The ratio of O_{ads}/O_{latt} was calculated and summarized in Table 4.2. The results indicated that the Zr-modified Co_3O_4 catalysts performed higher O_{sur}/O_{latt} ratio when compared to the pure Co_3O_4 catalyst, and $Co_{95}Zr_5$ possessed the higher ratio of O_{ads} concentration. It should be noticed that as the amount of Zr increased, this ratio decreased, indicating that the content of the active oxygen species decreased. The higher O_{ads}/O_{latt} ratio of $Co_{95}Zr_5$ than the other catalysts might also suggest more oxygen vacancies existing on the surface, which could provide more sites for the oxygen adsorption and activation.

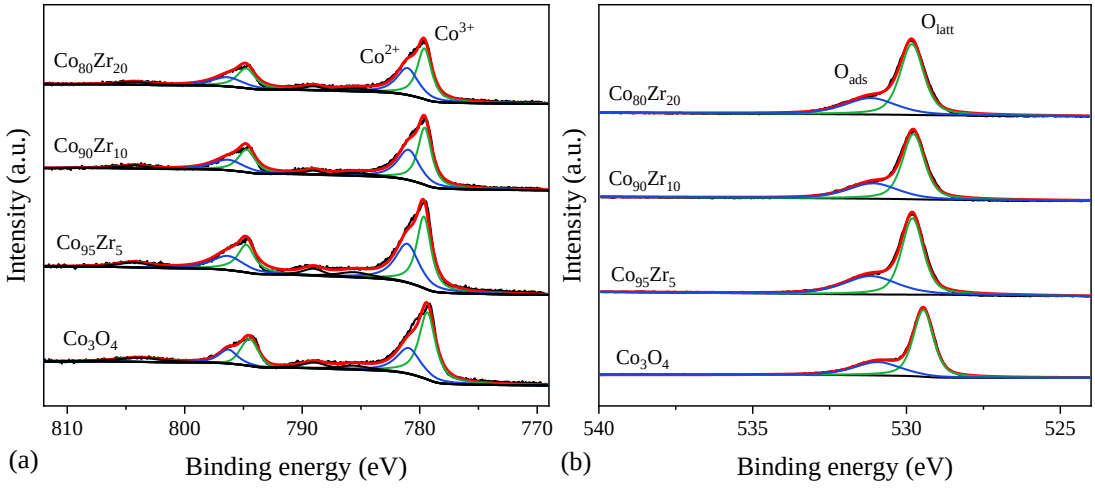

Fig. 4.6 XPS spectra of (a) Co 2p and (b) O 1s for the synthesized Co_xZr_y catalysts.

Table 4.2 H_2-TPR and XPS analysis of the synthesized Co_xZr_y catalysts.

Catalyst	Total H_2-consumption ($\mu mol\ g^{-1}$)	Theoretical H_2-consumption ($\mu mol\ g^{-1}$)	Reduction temperature of Co^{3+} to Co^{2+} (°C)	Co^{2+}/Co^{3+}	O_{ads}/O_{latt}
Co_3O_4	15818	16611	370	0.56	0.47
$Co_{95}Zr_5$	15008	15369	346	0.88	0.60
$Co_{90}Zr_{10}$	14037	14191	354	0.84	0.54
$Co_{80}Zr_{20}$	12264	12004	356	0.79	0.51

4.2.4 Catalytic performance of catalysts

The conversion curves and activity profiles for different catalysts were illustrated in Fig. 47. The T_{50} and T_{90} results of VC conversion were summarized in Table 4.3. The $Co_{95}Zr_5$ catalyst, on which T_{50} and T_{90} were 261 and 294 °C, respectively, showed the best activity for the oxidation of VC, followed by the $Co_{90}Zr_{10}$ catalyst. The performance of $Co_{80}Zr_{20}$ was almost the same as that of Co_3O_4. The ZrO_2 catalyst performed worst with a light-off temperature over 350 °C. With a small amount of Zr introduced, the performance of the Co_3O_4 catalyst was greatly improved (37 °C lower of T_{90} on $Co_{95}Zr_5$), indicating the high promotion effect of Zr on Co_3O_4 and the strong interaction between Co and Zr. The reaction rate (r_{VC}) was calculated at 240 °C (conversion below 25%) and the results were shown in Table 4.3. The reaction rate of catalyst $Co_{95}Zr_5$ (4.90×10^{-8} mol g^{-1} s^{-1}) is higher than that of pure Co_3O_4 and the other Zr-modified catalysts, which revealed that a small amount of Zr introduced into Co_3O_4 could remarkably enhance the performance of the catalyst.

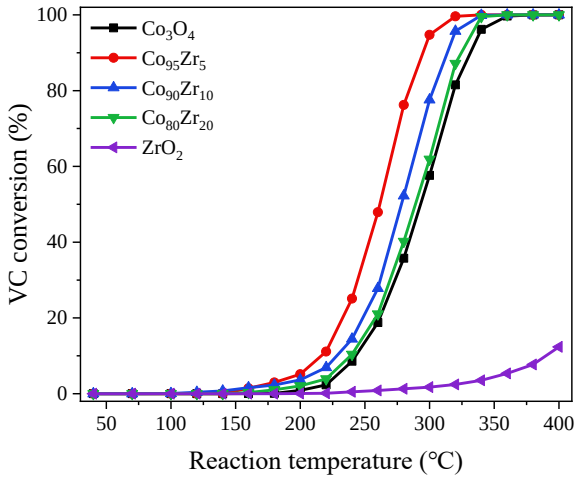

Fig. 4.7 Light-off curves of VC oxidation over the synthesized Co_xZr_y catalysts. Reaction condition: 1000 ppm VC and air balance; WHSV = 30000 mL g^{-1} h^{-1}.

Table 4.3 Catalytic performance of the synthesized Co_xZr_y catalysts.

Catalyst	T_{50} (°C)	T_{90} (°C)	$r \times 10^8$ (mol g^{-1} s^{-1})
Co_3O_4	292	331	3.30
$Co_{95}Zr_5$	261	294	9.21
$Co_{90}Zr_{10}$	278	313	5.60
$Co_{80}Zr_{20}$	288	324	4.12
ZrO_2	/	/	0.35

The total oxidation of CVOCs into CO_2, H_2O, HCl and/or Cl_2 should be the preference of the catalyst performance. However, it is a common phenomenon that the side reactions to yield chlorinated organics can take place on Co_3O_4-based catalysts [7, 11, 26]. In this work, there were four major chlorinated by-products and their concentrations during the reaction were shown in Fig. 4.8. These by-products could further be combusted into the final products with higher temperature. Among all the catalysts, $Co_{95}Zr_5$ still exhibited the best performance, with no chlorinated organics detected at 360 °C and higher temperature. Since the cleavage of C-Cl bond was the first step of the oxidation of VC, there would be numerous adsorbed Cl species on the surface of the catalyst. Then a possible mechanism of the formation of by-products was shown in Fig. 4.9. Apart from the chlorinated by-products, the other chlorine species were all transformed into HCl and/or Cl_2. A titration method [33, 34] was used to investigate the Cl_2 concentration over the most active catalyst $Co_{95}Zr_5$. The HCl concentration was calculated by the difference between the conversion concentration of VC and the other chlorinated products concentrations. The selectivity of HCl and Cl_2 in all the chlorinated products were shown in Fig. 4.10a. There was nearly no Cl_2 formed under 260 °C. however, the selectivity of Cl_2 began to increase from 260 °C and reached to 17.5% at 360 °C, which was attributed to the increasing Deacon reaction. The selectivity of HCl decreased below 260 °C mainly due to the increase of chlorinated organic by-products. When they were totally oxidized at higher temperature, the selectivity of HCl rose up to 82.5%.

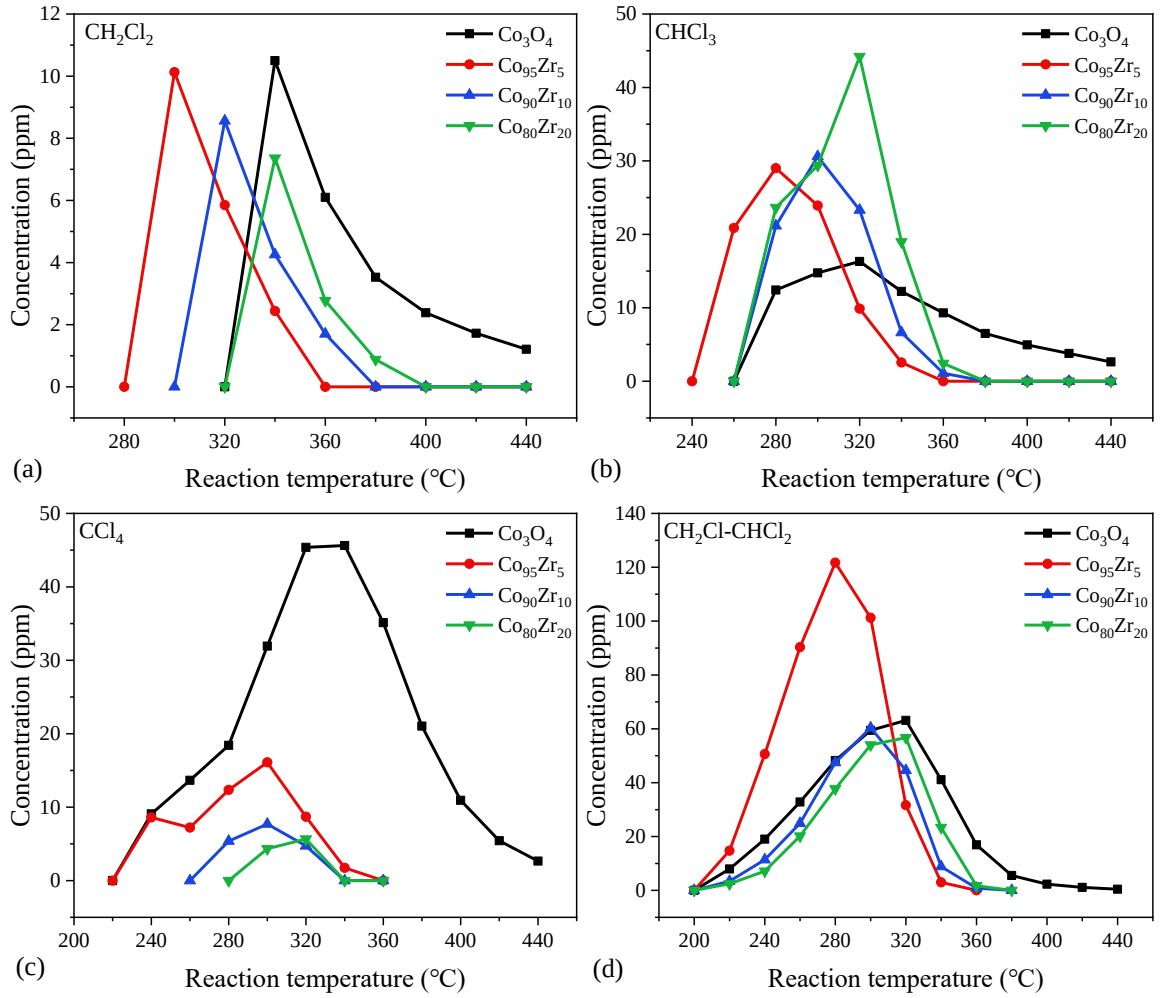

Fig. 4.8 Concentrations of chlorinated by-products vs. reaction temperature over the synthesized Co_xZr_y catalysts. Reaction condition: 1000 ppm VC and air balance; WHSV = 30000 mL g^{-1} h^{-1}.

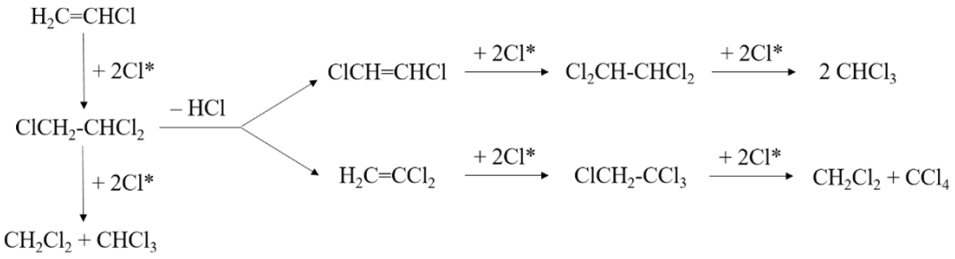

Fig. 4.9 A possible mechanism for the formation of chlorinated by-products over the synthesized Co_xZr_y catalysts.

In the end, a long-term stability test was performed on the $Co_{95}Zr_5$ catalyst and the result was shown in Fig. 4.10b. The test was carried out continuously at 260 °C for 25h, then 290 °C for 25h and finally 340 °C for 100h. At the relatively low temperature, the catalyst deactivated slightly at the beginning and then maintained its activity, while at the temperature of a complete conversion, it was quite stable without decrease of the conversion. It indicated that the chlorine atom would accumulate on the surface and poison the catalyst at low temperature, whereas the catalyst exhibited a good resistance to chlorine poisoning at higher temperature.

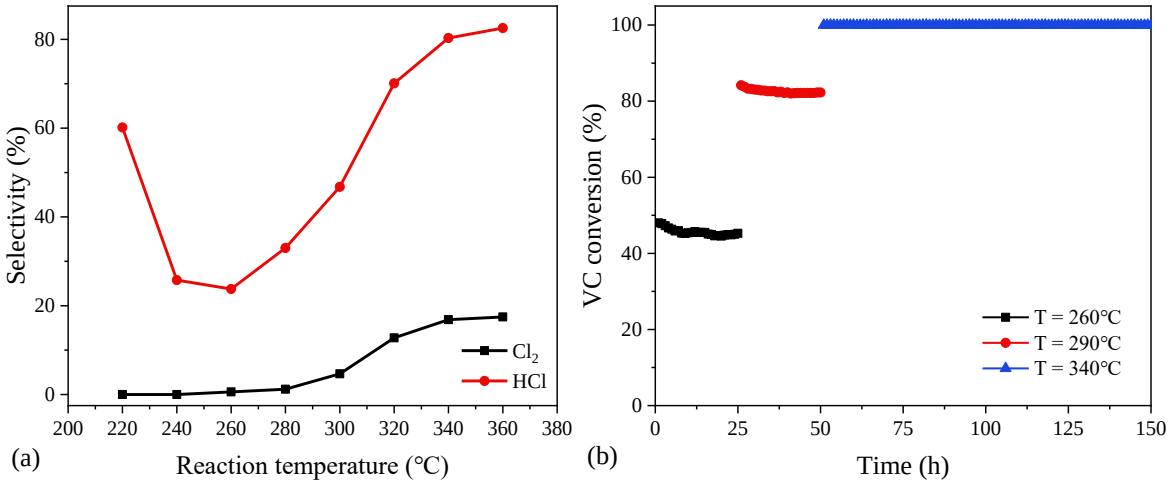

Fig. 4.10 (a) The selectivity of HCl and Cl_2 and (b) stability tests of VC oxidation over the $Co_{95}Zr_5$ catalyst. Reaction condition: 1000 ppm VC and air balance; WHSV = 30000 mL g^{-1} h^{-1}.

4.2.5 Discussions

The catalytic activity was dependent on the composition of the catalysts. Among all the catalysts, $Co_{95}Zr_5$ exhibited the best performance for both the conversion of VC and the further oxidation of chlorinated by-products. Fig. 4.11 shows the relationship of the Zr content and T_{50}, T_{90}, r, surface Co^{2+}/Co^{3+}, surface O_{sur}/O_{latt} and reduction temperature of Co^{3+} to Co^{2+} for the catalysts. It can be seen that the T_{50} and T_{90} of $Co_{95}Zr_5$ were lowest, and its reaction rate was highest. From the SEM images and the N_2-sorption results, it was evidenced that the introduction of Zr could restrain Co_3O_4 sintering and increase its specific surface area. While combined with the activity results, it could be revealed the particle size and the BET surface area were not the key factor affecting the catalytic performance in this work. By contrast, the H_2-TPR results revealed that the low-temperature reducibility of the catalysts was improved with the introduction of Zr, which can promote the catalytic performance. The reduction temperature order of Co^{3+} to Co^{2+} agreed well with the activity order of the catalysts. On the other hand, Zr increased the surface acidity to a large extent, resulting in easier C-Cl bond activation and promotion of further oxidation. What is more, through the XPS analysis, higher surface Co^{2+} was obtained with the introduction of Zr, which was associated with more surface oxygen vacancies. Oxygen vacancies are usually beneficial to the adsorption of oxygen, contributing to the formation of active oxygen species and oxygen mobility. The higher O_{sur} concentration of the Zr-modified catalysts was consistent with the above results. Thus, the improvement of the $Co_{95}Zr_5$ catalyst can be explained by the better reducibility, more surface acidity, higher surface Co^{2+} and O_{ads} concentrations, and better oxygen mobility.

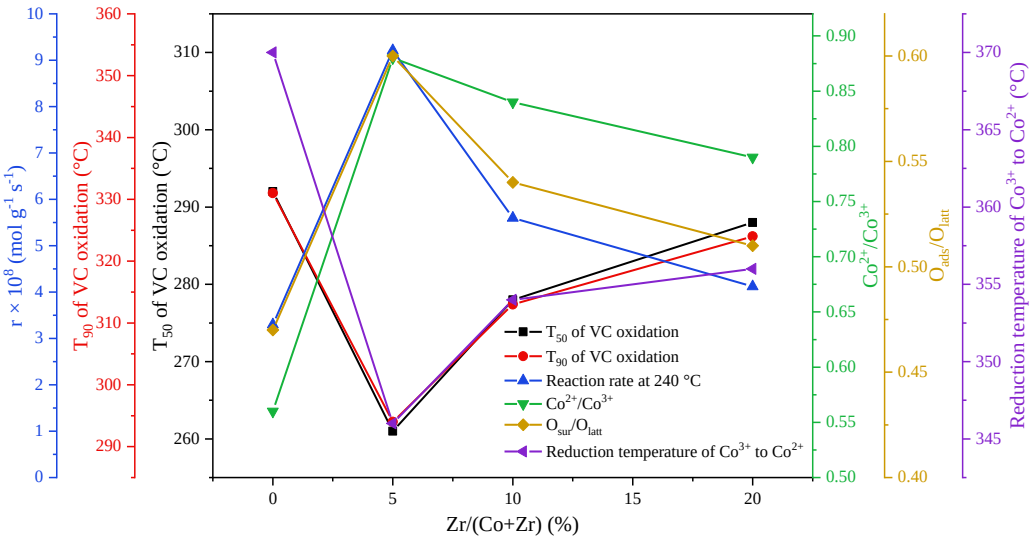

Fig. 4.11 The relationship between the catalytic performance of VC oxidation and the physico-chemical parameters of the Co_xZr_y catalysts.

4.3 The catalytic performance of the Zr-doped Co_3O_4 catalysts for propane oxidation

4.3.1 Preparation of catalysts

A series of Co_3O_4 catalysts with different compositions was synthesized via a sol-gel method using CA as the complexing agent. Typically, cobalt nitrate hexahydrate ($Co(NO_3)_2{\cdot}6H_2O$) and zirconyl nitrate ($ZrO(NO_3)_2 \cdot xH_2O$) were dissolved in 50 mL of distilled water. Then CA was added into the solution where the molar ratio of CA/(Co + Zr) was kept at 1.2. After complete dissolution of CA, the mixture was heated to 80 °C in a water bath and maintained at this temperature under stirring, until gel formation. After that, the gel was dried overnight in an oven at 120 °C to get a spongelike material that was calcined in a muffle furnace at 200 °C for 2 h, and then at 500 °C for 2 h with a rate of 2 °C min^{-1}. The obtained catalysts were denoted by x% Zr-Co_3O_4 (x = 0.5, 1, 1.5, 2), where x% represents the molar ratio of Zr/(Co + Zr). For the purpose of comparison, pure Co_3O_4 and ZrO_2 were prepared by the same method.

4.3.2 Evaluation of catalysts

The catalyst evaluation method is described in Chapter 2, Section 2.5.2.

4.3.3 Characterization of catalysts

Before the calcination of the dried gel powders, TG analysis was conducted to investigate their thermal decomposition profile and determine the correct calcination temperature. All the tested samples possessed similar weight loss curves (Fig. 4.12), with total mass loss of 65 ± 3%. Based on the above results, we have decided to first heat the dried gels at 200 °C for 2 h and then to further calcine them at 500 °C for 2 h as described in the catalyst preparation section to get the final catalysts. To determine the real contents of Zr and Co in the samples, ICP-OES analyses were performed, and the results are shown in Table 4.4.

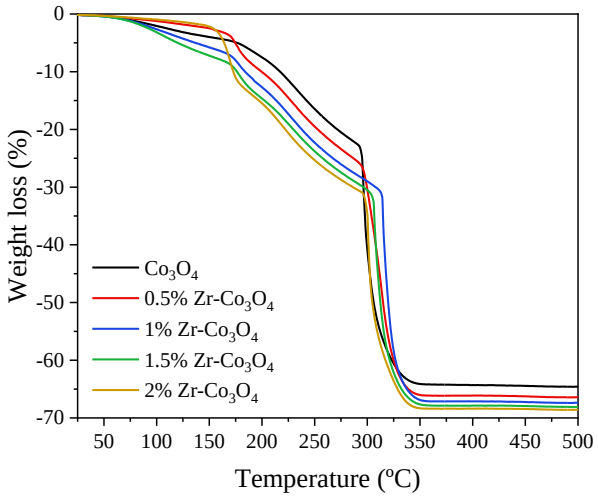

Fig. 4.12 TG curves of the dried precursors of the x%Zr-Co_3O_4 catalysts.

(1) XRD

The wide-angle XRD patterns of the prepared catalysts are displayed in Fig. 4.13. For pure Co_3O_4, diffraction peaks located at 19.0°, 31.3°, 36.8°, 38.5°, 44.8°, 55.6°, 59.3° and 65.2°, corresponding to the (111), (220), (311), (222), (400), (422), (511) and (440) crystal facets, respectively, were ascribed to the cubic phase of Co_3O_4 spinel (PDF # 43-1003) [31]. Likewise, Zr-doped Co_3O_4 catalysts showed crystalline features of cobalt oxide spinel and no signals due to any zirconia phase were detected, which suggested the successful doping of Zr into Co_3O_4 lattice or the high dispersion of ZrO_2, although we cannot exclude that it can be attributed to the low content of Zr. In the XRD patterns of pure ZrO_2, the peaks at 30.2°, 35.1°, 50.4° and 60.1° were attributed to the tetragonal phase ZrO_2 (PDF # 50-1089) [32].

From the enlarged diffraction peaks of (311) crystal facet (Fig. 4.13b), it could be seen that the signals were weakened and broadened by Zr doping, suggesting the reduced crystallinity and the decrease of Co_3O_4 crystallite sizes. Specifically, 1% Zr-Co_3O_4 showed the weakest and broadest diffraction peak, which corresponded to the smallest Co_3O_4 crystallite size (Table 4.4).

On the other hand, an obvious shift of the diffraction peaks of Zr-doped Co_3O_4 catalysts to smaller 2θ angles occurred, implying the lattice expansion due to Zr entering Co_3O_4 lattice [15, 26], The 1% Zr-Co_3O_4 sample showed the largest shift, suggesting that 1% represented the maximum amount of Zr that could enter into the Co_3O_4 lattice. The excess, as for 1.5% Zr-Co_3O_4 and 2% Zr-Co_3O_4, was likely as highly dispersed zirconium oxide.

The average crystallite sizes and lattice constants of the samples were calculated by the Scherrer equation based on the six most intense diffraction peaks, as listed in Table 4.4. The crystallite sizes of Co_3O_4 followed the order: 1% Zr-Co_3O_4 < 1.5% Zr-Co_3O_4 < 2% Zr-Co_3O_4 < 0.5% Zr-Co_3O_4 < Co_3O_4. Pure Co_3O_4 showed the largest crystallite size of 50.4 nm and the smallest lattice constant of 8.0874 Å, whereas the crystallite size decreased, and the lattice

constant increased with the doping of Zr, which was consistent with the intensities and shifts of the diffraction peaks.

The smallest crystallite size equal to 31.2 nm and the largest lattice constant of 8.0971 Å were obtained for 1% Zr-Co_3O_4. On the other hand, 2% Zr-Co_3O_4 showed the smallest lattice constant among Zr-doped Co_3O_4 samples, suggesting the lowest doping amount of Zr, but the crystallite size was smaller than that of 0.5% Zr-Co_3O_4. On this basis, it could be argued that highly dispersed zirconium oxides may inhibit Co_3O_4 crystals growth.

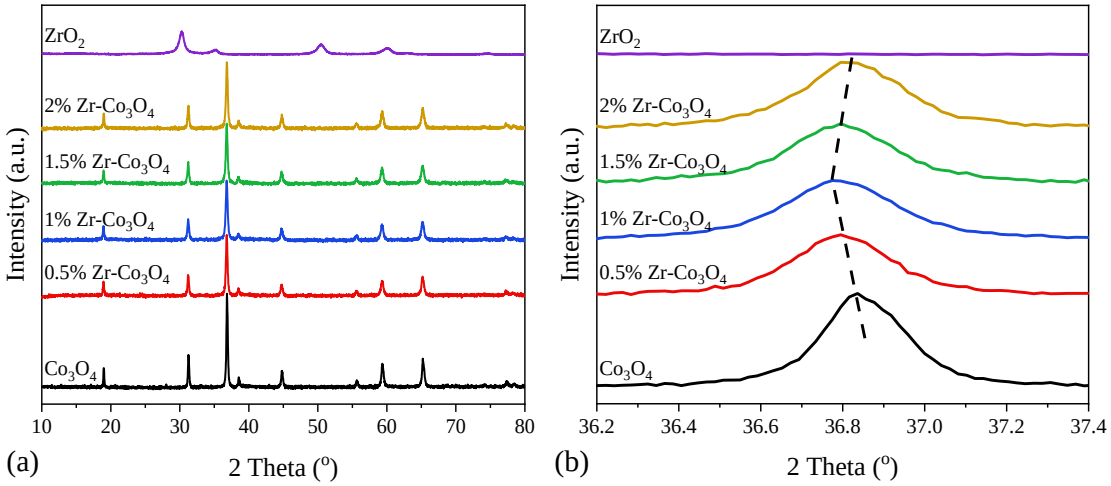

Fig. 4.13 (a) XRD patterns of the synthesized x%Zr-Co_3O_4 catalysts; (b) detail of the most intense diffraction peak of (311) crystal facet.

Table 4.4 The chemical composition, structural and textural properties of the synthesized x%Zr-Co_3O_4 catalysts.

Catalyst	Zr/Co (wt. %)		XRD data		N_2 sorption data	
	Expected	Actual	d (nm)	a (Å)	SSA ($m^2\ g^{-1}$)	V_{pore} ($cm^3\ g^{-1}$)
Co_3O_4	0/73.4	0/73.5	50.4	8.0874	7	0.039
0.5% Zr-Co_3O_4	0.6/72.9	0.4/72.4	36.7	8.0959	15	0.043
1% Zr-Co_3O_4	1.1/72.3	0.8/71.5	31.2	8.0971	22	0.083
1.5% Zr-Co_3O_4	1.7/71.7	1.1/71.3	34.2	8.0968	19	0.081
2% Zr-Co_3O_4	2.2/71.2	1.4/70.2	34.9	8.0915	18	0.074
ZrO_2	/	/	/	/	30	0.020

(2) Raman

Fig. 4.14 shows the Raman spectra of the synthesized catalysts. Pure Co_3O_4 presented five well-defined bands at around 194 (F_{2g}^1), 488 (E_g), 522 (F_{2g}^2), 618 (F_{2g}^3) and 691(A_{1g}) cm^{-1}, corresponding to the vibration modes of spinel Co_3O_4 [26, 32]. Raman bands around 691 and 194 cm^{-1} were assigned to the octahedral sites with A_{1g} symmetry and the tetrahedral sites with F_{2g}^1 symmetry of the crystalline Co_3O_4, respectively. Whereas the bands located at 488, 522 and 618 cm^{-1} were attributed to the E_g, F_{2g}^2 and F_{2g}^3 symmetry, respectively [33]. Similar

Raman bands were observed for the Zr-doped Co_3O_4 catalysts. While the bands became broader and the intensities were distinctly weakened, which could be correlated with the lattice distortion of the spinel structure caused by the doping of Zr that weakens the Co–O bonds [34]. Among the prepared samples, the weakest and broadest bands were observed for 1% Zr-Co3O4 and such finding is consistent with its lowest crystallinity and smallest crystallite size in XRD results. In addition, the presence of Zr shifted the Raman bands to lower frequencies, which would result in highly defective structures of the Zr-doped Co_3O_4 catalysts [35], especially for 1% Zr-Co_3O_4.

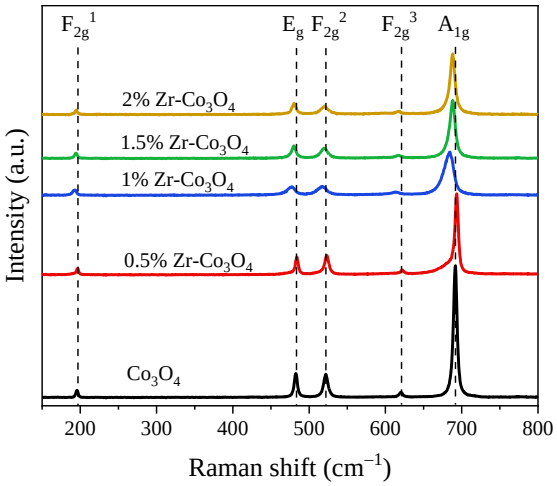

Fig. 4.14 Raman spectra of the synthesized x%Zr-Co_3O_4 catalysts.

(3) FT-IR

FT-IR analysis was further used to investigate the chemical structure of the synthesized catalysts, as shown in Fig. 4.15. For the pure Co_3O_4 and Zr-doped Co_3O_4 catalysts, the spectra displayed two sharp infrared adsorption bands at 654 and 539 cm^{-1}, which were assigned to the stretching vibrations of the metal-oxygen bond. The band at 654 cm^{-1} was attributed to the vibration mode of Co^{2+}-O from tetrahedral sites, whereas the band at 539 cm^{-1} was associated with the vibration mode of Co^{3+}-O from octahedral sites [36], which is consistent with the formation of spinel Co_3O_4 during the synthesis. As for ZrO_2, no characteristic adsorption bands were found in the set range.

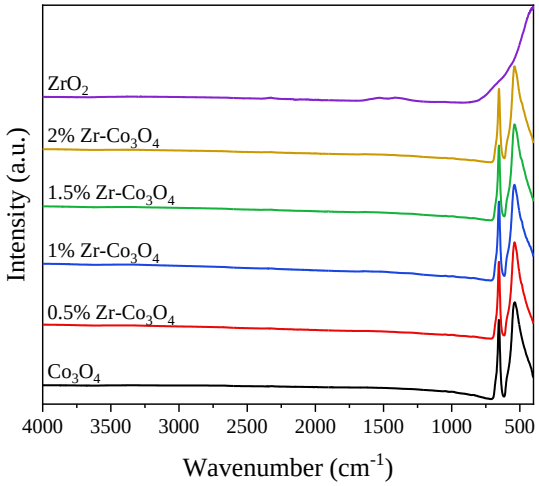

Fig. 4.15 FT-IR spectra of the synthesized x%Zr-Co_3O_4 catalysts.

(4) N_2-sorption

The N_2-sorption isotherms and pore size distribution curves are plotted in 4.16. The results showed that all the samples exhibited type IV isotherm with a H3 hysteresis loop except for ZrO_2 with a H2 hysteresis loop based on the IUPAC classification, indicating the presence of mesoporous in the samples [14,37]. From the pore size distribution curves, it was found that the pores with size below 10 nm were common to all the samples, but in different quantities, whereas the pores with size in the range of 10-50 nm only existed on the Zr-doped Co_3O_4 catalysts. The SSA and total pore volume values are listed in Table 4.4. Pure ZrO_2 exhibited the largest SSA, equal to 30 $m^2\ g^{-1}$, then, the order of the SSAs was as follows: 1% Zr-Co_3O_4 > 1.5% Zr-Co_3O_4 > 2% Zr-Co_3O_4 > 0.5% Zr-Co_3O_4 > Co_3O_4. The lowest crystallinity and smallest crystallite size of 1% Zr-Co_3O_4 well accounted for the largest SSA (22 $m^2\ g^{-1}$).

Apart from the smallest total pore volume of ZrO_2 that can be easily inferred by looking at the N_2-sorption isotherms, the total pore volumes of the Zr-doped catalysts were obviously larger than that of the undoped Co_3O_4 catalyst (Table 4.4). Considering the large SSA and total pore volume could expose more active sites, and facilitate the adsorption, diffusion and activation of the reactant molecules, it can be inferred that Zr-doping may promote the catalytic activity of Co_3O_4.

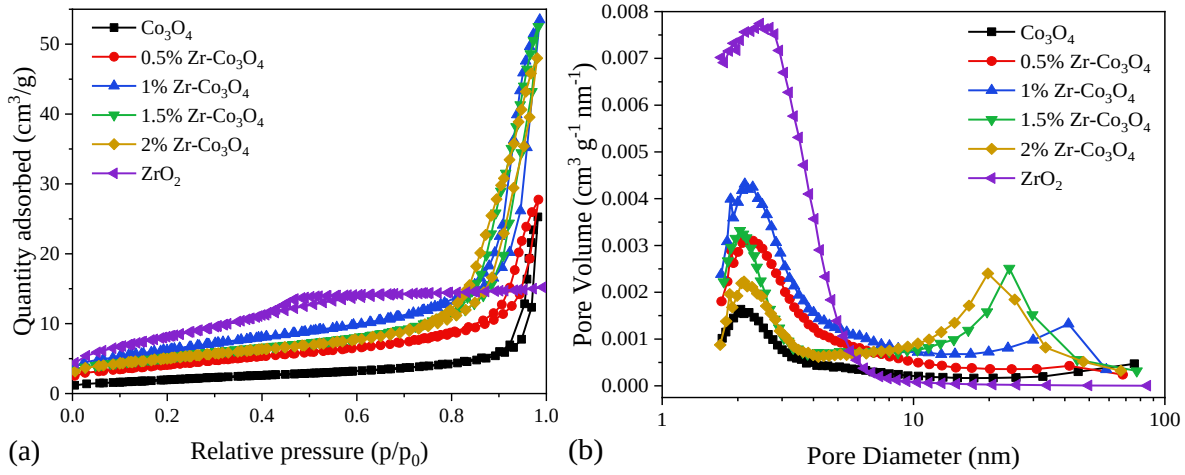

Fig. 4.16 (a) N_2 sorption isotherms and (b) pore size distributions of the synthesized x%Zr-Co_3O_4 catalysts.

(5) H_2-TPR

It has been reported that the reducibility of Co_3O_4-based catalysts is crucial to the catalytic performance of VOCs oxidation [19, 26]. Thus, H_2-TPR experiments were carried out to investigate the effect of Zr doping on the reduction behavior of the synthesized catalysts. The H_2-TPR profiles are shown in Fig. 4.17. ZrO_2 was not reducible in our experimental conditions, suggesting its superior stability and extremely low reducibility. For the Co_3O_4-based catalysts, the reduction processes started from ~185 °C and finished before 415 °C. All the H_2-TPR profiles of the x% Zr-Co_3O_4 catalysts were characterized by a small peak centered at around 290 – 300 °C (peak I), while this peak shifted to 308 °C as a shoulder peak in the case of Co_3O_4. Such peaks were attributed to the reduction of Co_3O_4 to CoO. At higher temperatures, ~350 °C, the main peak (peak II) occurred, which was assigned to the subsequent reduction of CoO to metallic Co [36, 39]. Looking at the TPR profiles, it was found that the first reduction step was greatly promoted by shifting the reduction peak to lower temperatures after the doping of Zr. The lowest reduction temperature was observed for 1% Zr-Co_3O_4. When the doping amount of Zr exceeded 1%, the reducibility slightly decreased. The same hindering effect due to an excessive amount of Zr was observed for the second reduction step in the H_2-TPR profiles. The reducibility order of the catalysts was as follows: 1% Zr-Co_3O_4 > 1.5% Zr-Co_3O_4 > 2% Zr-Co_3O_4 > 0.5% Zr-Co_3O_4 > Co_3O_4, which could be correlated with the crystallite sizes and the SSAs order. The smaller the crystallite size, and the larger the SSA, the better the reducibility. Moreover, the distortion of Co_3O_4 lattice caused by the doping of Zr could affect the crystalline symmetry, resulting in the formation of weaker Co–O bond than that of pure Co_3O_4, which was traced to the origin of the high reducibility of the Zr-doped Co_3O_4 catalysts [34].

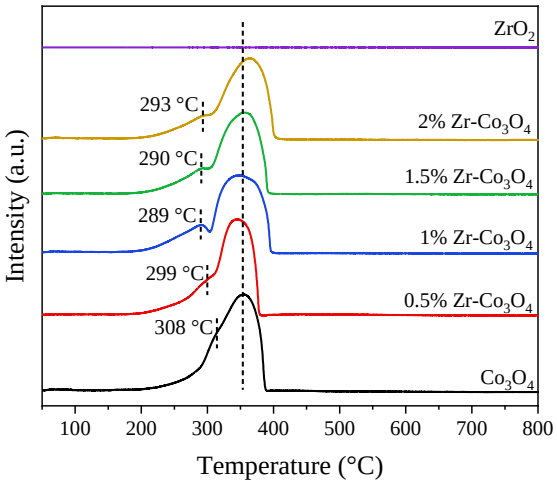

Fig. 4.17 H_2-TPR profile of the synthesized x%Zr-Co_3O_4 catalysts.

The quantitative evaluation of hydrogen consumption is shown in Table 4.5. The theoretical H_2 consumption for the complete reduction of Co_3O_4 to metallic Co is 16.61 mmol g^{-1} (slightly lower for the Zr-doped Co_3O_4 catalysts). However, the actual H_2 consumption was lower than the expected value for each sample. The presence of surface oxygen vacancies should be one important reason for this phenomenon; meanwhile, there might be two other possibilities: one was the formation of the Co–O–Zr species that could hardly be reduced, the other was the decrease of Co^{3+} content due to the substitution of Zr in the spinel structure. Considering the low doping amount of Zr, the former one should not make big difference to the H2 consumption. In view of the different radius of Co^{2+} (0.078 nm), Co^{3+} (0.065 nm) and Zr^{4+} (0.072 nm), Zr^{4+} would mainly replace Co^{3+} during the doping process [26], leading to the decrease of Co^{3+} content. On the other hand, to keep the charge balance, the amount of Co^{2+} would increase. Thus, the decrease of H_2 consumption was reasonable for that it took less H_2 to reduce Co^{2+} than Co^{3+}. From the ratio of actual H_2 consumption to theoretical H_2 consumption, it was inferred that there were more Co^{3+} displaced by Zr^{4+} for 1% Zr-Co_3O_4, which was in accordance with the XRD analysis. According to the literature, the area ratios of peak I to peak II could be regarded as a reference for the relative contents of Co^{3+} and Co^{2+}. Therefore, they were calculated and summarized in Table 4.5. The values of the Zr-doped Co_3O_4 catalysts were lower than that of pure Co_3O_4, and 1% Zr-Co_3O_4 showed the lowest ratio of Co^{3+}/Co^{2+}, which was in good agreement with the above results.

Table 4.5 H_2-TPR data of the synthesized x%Zr-Co_3O_4 catalysts.

Catalyst	H_2 consumption (mmol g^{-1})			A_{peakI} / A_{peakII}
	Theoretical	Actual	Actual/Theoretical	
Co_3O_4	16.61	15.13	0.911	0.31
0.5% Zr-Co_3O_4	16.53	14.49	0.877	0.27
1% Zr-Co_3O_4	16.44	12.11	0.737	0.24
1.5% Zr-Co_3O_4	16.36	13.46	0.823	0.24
2% Zr-Co_3O_4	16.28	13.80	0.848	0.25

(6) O_2-TPD

O_2-TPD experiments were carried out through TG analysis, as described in the experimental section. The samples were first pretreated with N_2 at 500 °C to remove any adsorbed species, then cooled down and saturated with O_2 adsorption, and finally heated to 800 °C in N_2 flow to deplete oxygen species. The weight losses during the last step were associated with the amount of oxygen vacancies, as well as the oxygen release capacity of the samples [40]. As plotted in Fig. 4.18, there were mainly three weight loss regions observed for all tested samples. The first one in the temperature range of 50–200 °C was ascribed to the desorption of physically adsorbed oxygen species (O_α), whereas the second one between 200 and 725 °C was assigned to the chemically adsorbed oxygen species (O_β), which can participate in the oxidation reaction as active oxygen species. The second one corresponded to the labile oxygen species filling oxygen vacancies, thus the total weight loss from 200 to 725 °C could be used to evaluate the content of oxygen vacancies. 1% Zr-Co_3O_4 and 1.5% Zr-Co_3O_4 showed much larger weight loss of O_β than the other catalysts, suggesting the presence of more surface oxygen vacancies in these two samples.

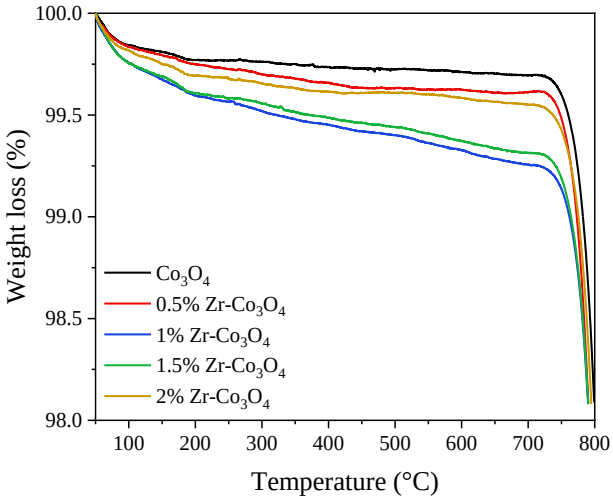

Fig. 4.18 Weight loss versus temperature of the synthesized x%Zr-Co_3O_4 catalysts during O_2-TPD experiments.

The calculated weight losses, representing the contents of O_α and O_β, are listed in Table 4.6. Pure Co_3O_4 had the lowest contents of both O_α and O_β, whereas 1% Zr-Co_3O_4 exhibited the highest contents of O_α and O_β among all the catalysts. The orders for the contents of O_α and O_β were the same, 1% Zr-Co_3O_4 > 1.5% Zr-Co_3O_4 > 2% Zr-Co_3O_4 > 0.5% Zr-Co_3O_4 > Co_3O_4. Specifically, 2% Zr-Co_3O_4 possessed a considerable content of Oα due to its large pore volume, whereas much lower content of O_β were found when compared to 1% Zr-Co_3O_4 and 1.5% Zr-Co_3O_4. As discussed above, excess zirconium in 2% Zr-Co_3O_4 could disperse on the surface of the catalyst, which may cover the oxygen vacancies and reduce the amount of chemically adsorbed oxygen species. Finally, all the tested samples showed significant weight losses above 725 °C, which was associated with the thermal reductive decomposition of Co_3O_4 to CoO.

Table 4.6 O_2-TPD and XPS data of the synthesized x%Zr-Co_3O_4 catalysts.

Catalyst	O_α (%)	O_β (%)	Co^{2+}/Co^{3+}	O_{ads}/O_{latt}
Co_3O_4	0.23	0.08	0.62	0.48
0.5% Zr-Co_3O_4	0.25	0.14	0.65	0.52
1% Zr-Co_3O_4	0.40	0.36	0.77	0.64
1.5% Zr-Co_3O_4	0.39	0.31	0.71	0.61
2% Zr-Co_3O_4	0.31	0.16	0.66	0.54

(7) XPS

Fig. 4.19 shows the Co 2p and O 1s XPS spectra of the pure Co_3O_4 and x% Zr-Co_3O_4 catalysts. The Co 2p spectra of pure Co_3O_4 displayed two main peaks at ~795.1 and 779.9 eV, corresponding to the Co $2p_{1/2}$ and Co $2p_{3/2}$ spin-orbital peaks of Co_3O_4 spinel [1, 15]. The spin-orbit splitting energy of these two peaks was around 15.2 eV, agreeing well with those reported in the literature [15, 35]. Similar Co 2p spectra were observed for the Zr-doped catalysts. By deconvolution of the Co 2p spectra, the Co $2p_{3/2}$ signal was decomposed into two components. One peak at B.E. of ~779.8 eV was attributed to the surface Co^{3+} species, while the other at B.E. of ~781.4 eV was assigned to the surface Co^{2+} species. The superficial Co^{2+}/Co^{3+} molar ratios calculated from the peak area percentages are listed in Table 4.6. Higher surface Co^{2+} concentrations were found for the Zr-doped Co_3O_4 catalysts as compared with that for pure Co_3O_4, indicating the presence of more surface oxygen vacancies [1, 35], which may be caused by the substitution of Co^{3+} by Zr^{4+} as discussed above and can promote the VOCs oxidation process. The highest surface Co^{2+} concentration was observed for 1% Zr-Co_3O_4, which was consistent with the maximum Zr^{4+} entering into the spinel lattice and made it a good candidate for propane oxidation.

The O 1s spectra were found to be broad for all the samples, indicating the existence of several kinds of surface oxygen species. Hence, the asymmetrical O 1s peaks were decomposed into two components at ~529.9 and 531.2 eV. The former was correlated with the surface lattice

species (O_{latt}), whereas the latter corresponded to the surface adsorbed oxygen species (O_{ads}) [32]. As seen from Table 4.6, the O_{ads}/O_{latt} ratios of the Zr-doped catalysts were higher than that of pure Co_3O_4, which was in agreement with the O_2-TPD results. 1% Zr-Co_3O_4 exhibited a higher O_{ads}/O_{latt} ratio than the other Zr-doped Co_3O_4 catalysts, which meant that there were more active oxygen species in 1% Zr-Co_3O_4 that can participate in oxidation reaction at low temperature [1, 3].

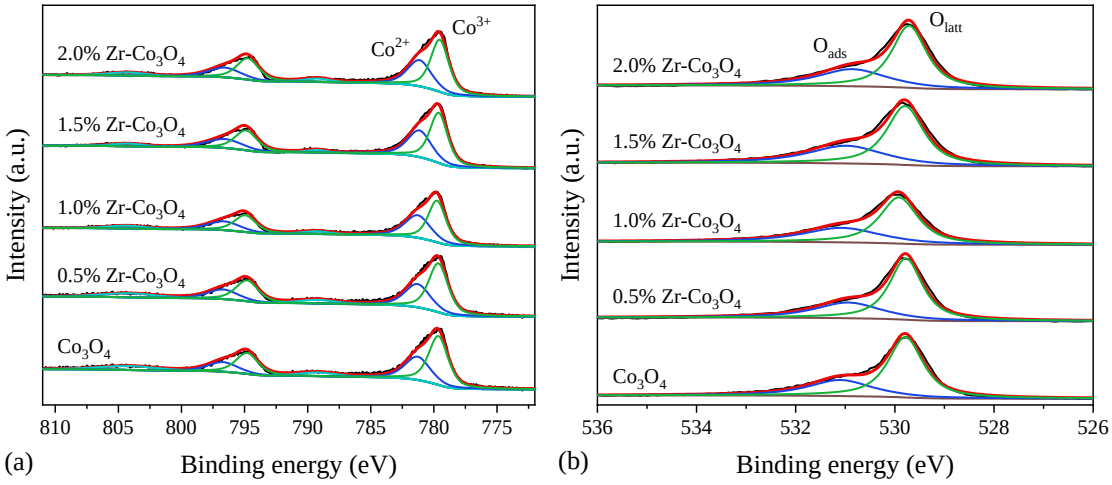

Fig. 4.19 XPS spectra of (a) Co 2p and (b) O 1s for the synthesized x%Zr-Co_3O_4 catalysts.

4.3.4 Catalytic performance of catalysts

The synthesized catalysts were applied to evaluate the catalytic activity for propane oxidation, which could be regarded as a model reaction of short-chain alkanes. The propane conversion curves versus temperature are plotted in Fig. 4.20a, and the values of T50 and T90 are listed in Table 4.7. ZrO_2 showed no activity for propane oxidation, which was consistent with its poor reducibility in TPR experiments. The other catalysts displayed considerable activity, among which the Zr-doped Co_3O_4 catalysts performed better than pure Co_3O_4. For instance, T_{50} and T_{90} over pure Co_3O_4 were 229 and 269 °C, while T_{50} and T_{90} over 1% Zr-Co_3O_4 were 212 and 241 °C, respectively. During the propane oxidation process, only trace amounts of by-product propene (< 8ppm) were detected at low temperatures, demonstrating the excellent selectivity of the synthesized catalysts for the total oxidation of propane. The carbon balance was estimated to be 99%−101%. Regarding the Zr-doped Co_3O_4 catalysts, the doping amount remarkably influenced their catalytic activity for propane oxidation. With introducing and increasing the amount of Zr, the T_{50} and T_{90} values gradually decrease. However, after the doping amount exceeded 1%, the light-off curves significantly shifted to high temperature regions. Taking 2% Zr-Co_3O_4 as an example, its T_{90} value is 20 °C higher than that of 1% Zr-Co_3O_4. The catalytic activity of Co_3O_4-based catalysts for total oxidation of propane was ranked as follows: 1% Zr-Co_3O_4 > 1.5% Zr-Co_3O_4 > 2% Zr-Co_3O_4 > 0.5% Zr-Co_3O_4 > Co_3O_4.

The reaction rates of the pure Co_3O_4 and Zr-doped Co_3O_4 catalysts at 185 °C were calculated and the results are summarized in Table 4.7. The Arrhenius plots of lnr versus 1000/RT are plotted in Fig 4.20b, and the activation energies (E_a) obtained from the slopes are listed in Table 4.7. It was found that E_a for propane oxidation over the Zr-doped Co_3O_4 catalysts was 77.4−85.0 kJ mol^{-1}, lower than that over pure Co_3O_4 (87.9 kJ mol^{-1}), suggesting that propane oxidation proceeded more easily on the Zr-doped Co_3O_4 catalysts. Besides, the Zr-doped Co_3O_4 catalysts presented much higher reaction rates than pure Co_3O_4 at 185 °C. For instance, the reaction rate of 1% Zr-Co_3O_4 is almost twice that of pure Co_3O_4. The reaction rates followed the order of 1% Zr-Co_3O_4 > 1.5% Zr-Co_3O_4 > 2% Zr-Co_3O_4 > 0.5% Zr-Co_3O_4 > Co_3O_4. Summarizing, 1% Zr-Co_3O_4 exhibited the highest catalytic activity for propane oxidation among all the synthesized catalysts.

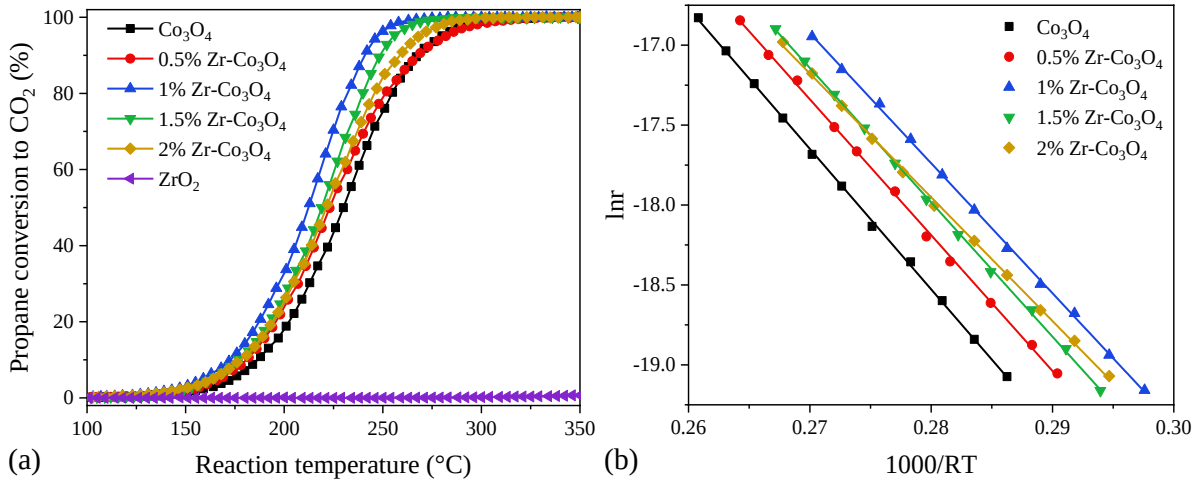

Fig. 4.20 (a) Light-off curves and (b) the Arrhenius plots of lnr of propane oxidation over the synthesized x%Zr-Co_3O_4 catalysts. Reaction condition: 1000 ppm propane and synthetic air balance; WHSV = 40000 mL g^{-1} h^{-1}.

Table 4.7 T_{50}, T_{90} and reaction rates at 185 °C of the synthesized x%Zr-Co_3O_4 catalysts in propane oxidation.

Catalyst	T_{50} (°C)	T_{90} (°C)	r × 10^8 (mol g^{-1} s^{-1})
Co_3O_4	229	269	4.65
0.5%Zr-Co_3O_4	223	268	6.12
1%Zr-Co_3O_4	212	241	9.03
1.5%Zr-Co_3O_4	219	249	7.07
2%Zr-Co_3O_4	220	261	6.66

Propane oxidation tests free of oxygen were carried out to investigate the content of active oxygen species and the mobility of lattice oxygen in the catalysts. Before the tests, the catalysts were pretreated at 300 °C for 1 h with He to remove weakly adsorbed surface species. To better represent the differences between the catalysts, a higher WHSV of 160,000 mL g^{-1} h^{-1} was

applied in the tests. The evolution of CO_2 concentration and temperature versus time were shown in Fig. 4.21. One can see that even in the absence of oxygen, some propane could be oxidized into CO_2 between 100 and 350 °C during the heating ramp over the catalysts. However, in the cooling stage, no CO_2 was produced in this temperature range. This phenomenon can be explained by the complete depletion of chemisorbed oxygen. On the other hand, continuous production of CO_2 was observed for 1 h at 350 °C, indicating that surface lattice oxygen in the catalysts can migrate and participate in propane oxidation. The amount of CO_2 production reflected the content of active oxygen species and oxygen mobility of the catalysts. Pure Co_3O_4 clearly showed the minimum active oxygen content and the weakest oxygen mobility. The content of active oxygen species and oxygen mobility of x%Zr-Co_3O_4 catalysts were significantly enhanced due to the incorporation of Zr, which was consistent with the O_2-TPD analysis. Among all the catalysts, 1% Zr-Co_3O_4 exhibited the largest amount of active oxygen species and the highest oxygen mobility.

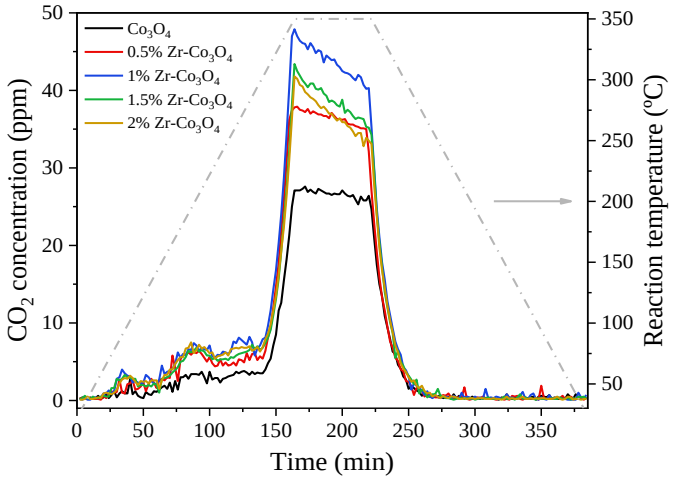

Fig. 4.21 The evolution of CO_2 concentrations in propane oxidation without oxygen over the synthesized x%Zr-Co_3O_4 catalysts.

The influence of WHSV on the catalytic performance of propane oxidation over 1% Zr-Co_3O_4 was investigated, and the results are presented in Fig. 4.22a. The space velocity is usually very high and changeable for the practical VOCs treatment. When increasing WHSV, the residence time of reactants through the catalyst bed decreases, resulting in a higher temperature required for the sufficient conversion of VOCs. As expected, the light-off curve of propane oxidation shifted to higher temperatures with the increase of WHSV. However, 100% conversion of propane can still be achieved below 300 °C at a WHSV as high as 160,000 mL g^{-1} h^{-1}, which is of great significance for the industrial application.

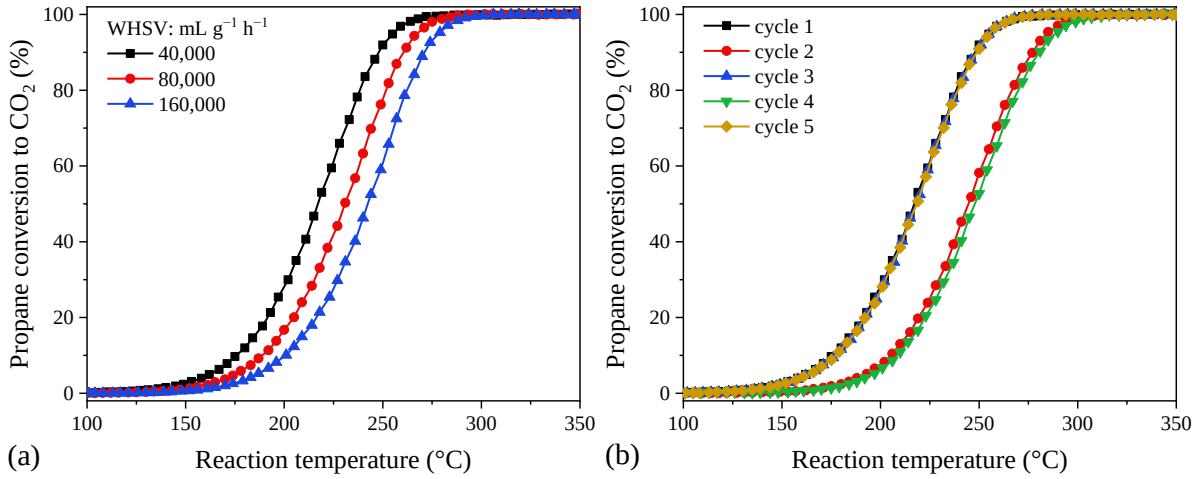

Fig. 4.22 Effects of (a) WHSV and (b) water vapor on propane oxidation over the 1%Zr-Co_3O_4 catalyst. Reaction conditions: 0.1 vol.% C_3H_8 + 21 vol.% O_2 at a WHSV of 40000 mL g^{-1} h^{-1} (cycle 1); introduction of 4 vol.% H_2O (cycle 2); removal of 4 vol.% H_2O (cycle 3); introduction of 8 vol.% H_2O (cycle 4); removal of 8 vol.% H_2O (cycle 5).

On the other hand, there is generally a certain amount of water vapor in the practical flue gas. Thus, the effect of water on the catalytic oxidation of propane over 1% Zr-Co_3O_4 was examined. As shown in Fig. 8b, the conversion efficiency of propane was suppressed when 4 vol.% H_2O was introduced into the feed stream. The value of T_{90} of propane conversion was increased to 277 °C, which was 36 °C higher than that in dry conditions. A further increase of water content to 8 vol.% had a similar negative effect, causing slightly more activity loss than 4 vol.% H_2O. This meant that the influence of water on propane oxidation was limited. A possible reason for such a decrease in activity may be the competitive adsorption between propane and water molecular on the active sites [41]. Moreover, the catalytic activity could be fully recovered after removing water from the inlet, suggesting the reversibility of the deactivation.

Toluene oxidation is another model reaction (aromatic hydrocarbon) commonly used to evaluate the catalytic activity of a catalyst. To check the versatility of the synthesized catalysts, Co_3O_4, 1% Zr-Co_3O_4, 2% Zr-Co_3O_4 and pure ZrO_2 were also tested in toluene oxidation. It was reported that the formation of CO_2 usually required a higher temperature than the conversion of toluene due to the adsorption of toluene and the formation of stable intermediates at low temperatures [10]. The light-off curves of the cooling ramp were thus established based on the CO_2 yield and shown in Fig. 4.23a, with the T_{50} and T_{90} values displayed in Table 4.8. Pure ZrO_2 showed negligible activity for toluene oxidation within the test temperature range, while Co_3O_4-based catalysts exhibited high performance starting from ca. 220 °C and completing before 300 °C. The catalytic performance of pure Co_3O_4 was significantly improved by Zr

doping, especially in the low temperature region. The promotion effect on 1% Zr-Co_3O_4 is more pronounced than that on 2% Zr-Co_3O_4.

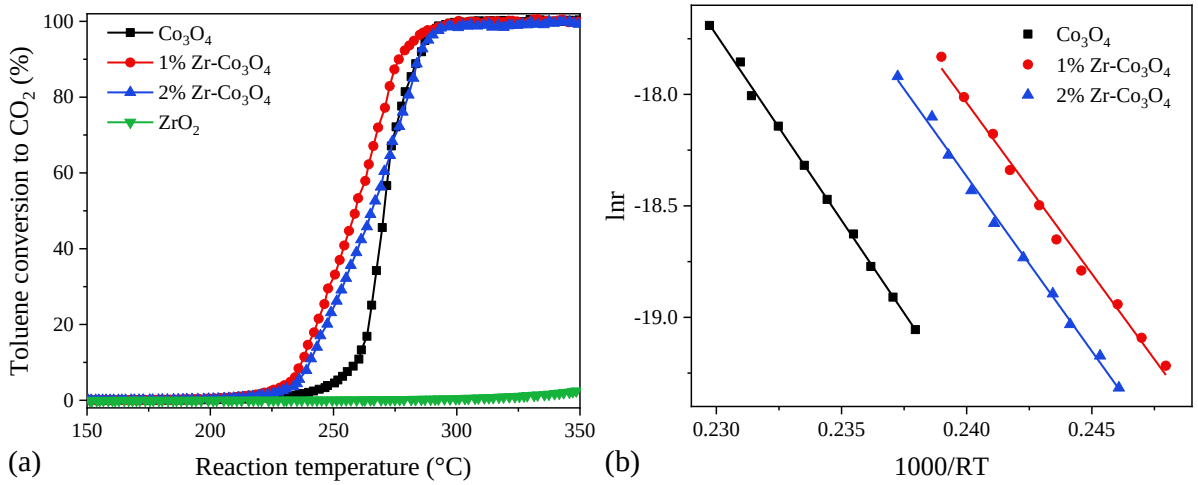

Fig. 4.23 (a) Light-off curves and (b) the Arrhenius plots of lnr of toluene oxidation over the synthesized x%Zr-Co_3O_4 catalysts. Reaction condition: 1000 ppm toluene and synthetic air balance; WHSV = 40000 mL g^{-1} h^{-1}.

Similarly, the reaction rates of the catalysts at 247 °C were calculated, and the Arrhenius plots of lnr versus 1000/RT (Fig. 4.23b) were drawn to get the activation energies. The results were listed in Table 4.8. One can see that the reaction rates of the Zr-doped Co_3O_4 catalysts (10.07×10^{-8} and 7.05×10^{-8} mol g^{-1} s^{-1} for 1% Zr-Co_3O_4 and 2% Zr-Co_3O_4, respectively)) are higher than that of pure Co_3O_4 (1.34×10^{-8} mol g^{-1} s^{-1}), again demonstrating the best activity of 1% Zr-Co_3O_4 for toluene oxidation. The apparent activation energies of the Zr-doped Co_3O_4 catalysts are significantly lower than that of pure Co_3O_4, suggesting the easier adsorption and activation of toluene after Zr doping [10].

Table 4.8 T_{50}, T_{90} and reaction rates at 247 °C of the synthesized x%Zr-Co_3O_4 catalysts in toluene oxidation.

Catalyst	T_{50} (°C)	T_{90} (°C)	r × 10^8 (mol g^{-1} s^{-1})
Co_3O_4	271	285	1.34
1%Zr-Co_3O_4	258	276	10.07
2%Zr-Co_3O_4	265	285	7.05

Stability is a key issue in the practical applications of the catalysts. With the increase of operating cycle or ageing time, catalyst crystal sintering or coke accumulation may occur, leading to a decrease in the catalytic activity. Herein, the stability of the most active catalyst (1% Zr-Co_3O_4) in propane oxidation was evaluated by performing three continuous heating-cooling cycles and long-term durability tests. The light-off curves of the three cycles in propane oxidation are shown in Fig. 4.24a. No shifts of the light-off curves were observed over 1% Zr-

Co_3O_4 among the three cycles in propane oxidation, demonstrating the decent cycling stability of 1% Zr-Co_3O_4.

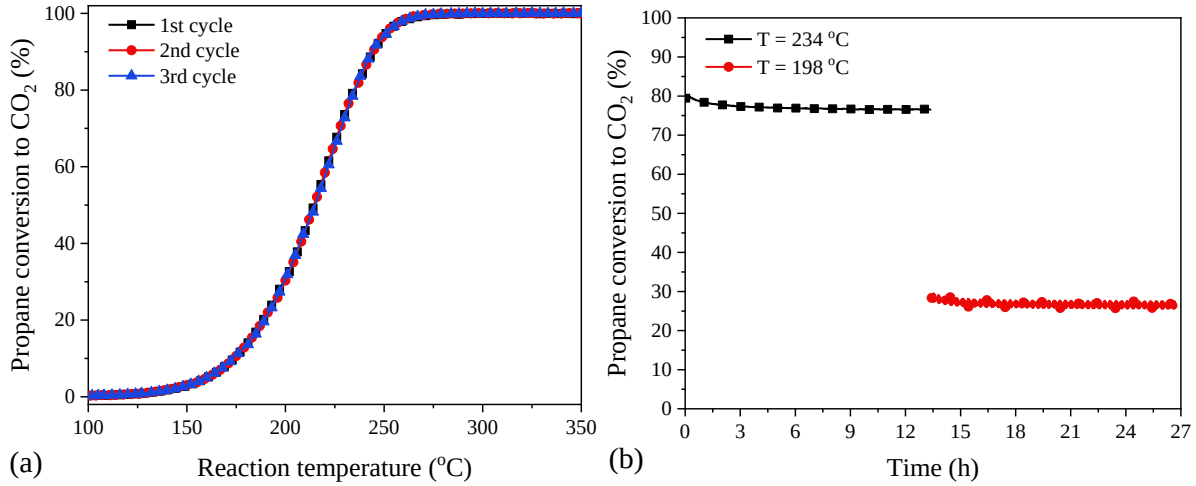

Fig. 4.24 (a) The light-off curves of the three continuous heating-cooling cycles and (b) the stability test for propane oxidation on 1%Zr-Co_3O_4. Reaction condition: 1000 ppm propane and synthetic air balance; WHSV = 40000 mL g^{-1} h^{-1}.

Two temperatures, one at the high conversion and the other at the low conversion, were chosen for the long-term durability tests of 1% Zr-Co_3O_4 in propane oxidation. The evolution of propane conversion during the test is shown in Fig. 4.24b. Stable propane conversion was maintained at both given temperatures, suggesting the excellent durability of 1% Zr-Co_3O_4 in propane oxidation. Subsequently, the used 1% Zr-Co_3O_4 catalyst was characterized by XRD and N_2-sorption (Fig. 4.25) to obtain the crystallite size and SSA. Negligible differences in the crystallite size (31.2 vs. 32.1 nm) and the SSA (22 vs. 21 m^2 g^{-1}) were observed between the fresh and used catalyst, indicating that the structural and textural properties of 1% Zr-Co_3O_4 remained unchanged in the long-term test.

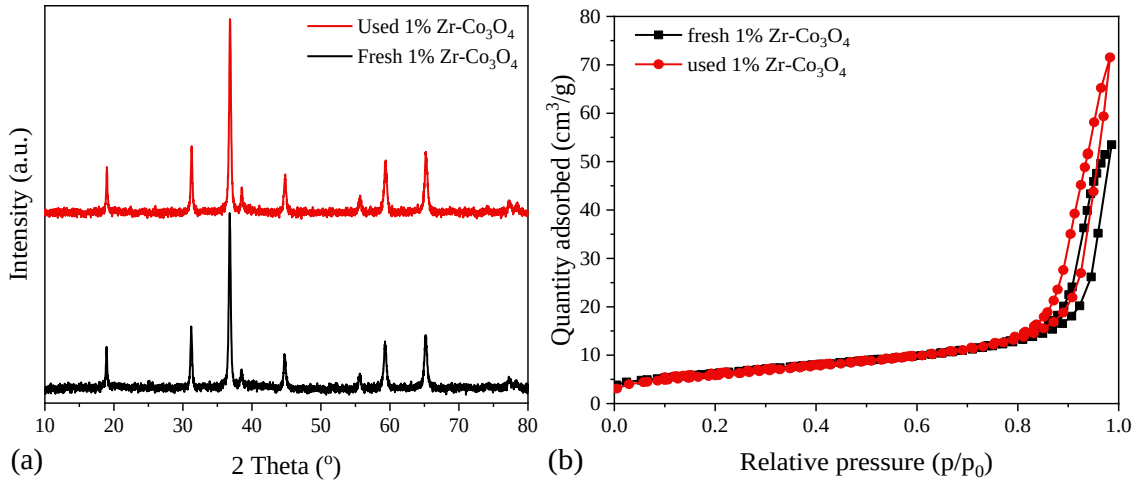

Fig. 4.25 (a) The XRD patterns and (b) N_2 sorption isotherms of 1%Zr-Co_3O_4 before and after the stability test for propane oxidation.

Fig. 4.26 shows the DRIFT spectra of the propane oxidation reaction at 220 °C over 1% Zr-Co_3O_4. For propane adsorption (Fig. 4.26a), the strong peak at ~2968 cm^{-1} together with the shoulder peaks at ~2982, 2901 and 2872 cm^{-1} are ascribed to the C–H vibrations of gaseous propane [9]. The peaks correspond to the asymmetric vibrations of COO^- species (~1542 and 1507 cm^{-1}), asymmetric vibrations of CH_3 species (~1432 and 1472 cm^{-1}), symmetric vibrations of CH_3 species (~1375 and 1346 cm^{-1}), and vibration of C–O (~1287 cm^{-1}) come from various carboxylate species, such as acetate and formate [8, 11]. The peak around 2345 cm^{-1} arises from gaseous CO_2 [8]. Once the propane was fed into the chamber, the formation of carboxylate species and CO_2 was observed. This indicates that the lattice oxygen species in the catalyst were readily involved in propane oxidation via the MvK mechanism, which agrees well with the experimental results of propane oxidation without oxygen. The peaks of propane and carboxylate intensified as the adsorption time increased, indicating the good adsorption capacity and oxidation ability of 1% Zr-Co_3O_4 towards propane.

After the incorporation of 10 vol.% O_2 (Fig. 4.26b), the signal at ~2968 cm^{-1} corresponding to gaseous propane deceased, suggesting the occurrence of oxidation reaction between propane and oxygen. The weakening of peak at ~1432 cm^{-1} may reflect a decrease in the concentration of acetate and the transformation of acetate into formate. At the desorption stage (Fig. 4.26c), the peaks of propane and CO_2 disappeared gradually in 25 min, indicating the excellent oxidation ability and quick CO_2 desorption ability of 1% Zr-Co_3O_4. It was also found that the peak at ~1542 cm^{-1} was gradually redshifted and merged with the peak at ~1507 cm^{-1}, suggesting the formation of more COO^- species [9]. The continuous weakening of peak at ~1432 cm^{-1} further confirmed the transformation of acetate into formate. Based on the above results, it is inferred that propane oxidation over 1% Zr-Co_3O_4 proceeds as follows: propane firstly adsorbs on the catalyst surface and immediately reacts with surface lattice oxygen, forming some partially oxidized intermediates (carboxylate), which was finally oxidized into CO_2 and H_2O by the activated oxygen species.

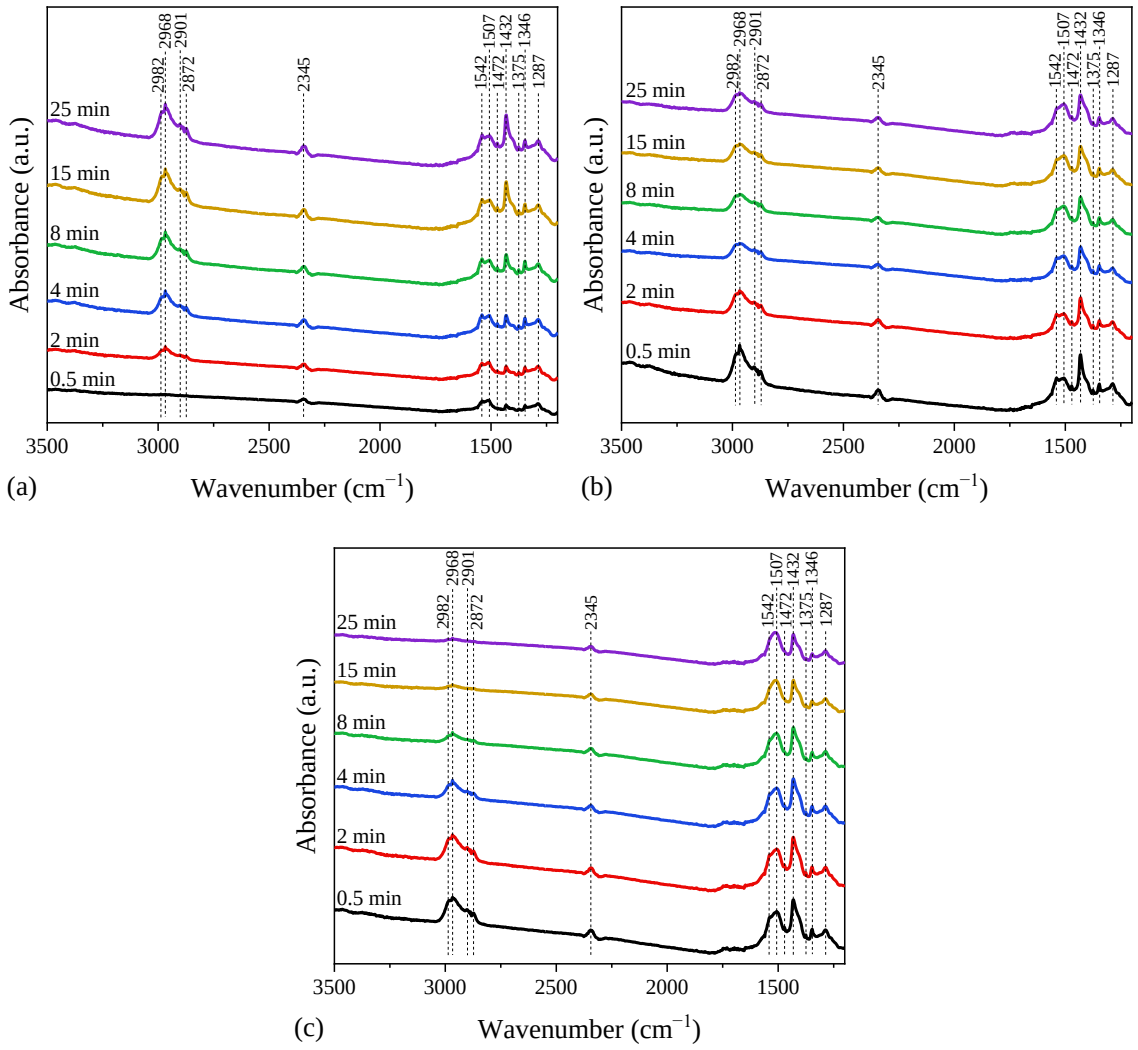

Fig. 4.26 Time-dependent in situ DRIFT spectra of (a) propane adsorption, (b) surface oxidation, and (c) desorption at 220 °C over 1%Zr-Co_3O_4.

4.3.5 Discussions

In this study, the low doping of Zr into Co_3O_4 was proved to influence not only the physicochemical properties of the x% Zr-Co_3O_4 catalysts but also their catalytic performance in propane oxidation. XRD and N_2 sorption results show that low doping of Zr inhibited the growth of Co_3O_4 crystallite, induced lattice expansion of the spinel, and led to larger SSA and porosity. Raman spectra results reveal the distortions and defective structures of the x% Zr-Co_3O_4 catalysts, which was associated with the presence of abundant oxygen vacancies. Both H_2-TPR and CO-TPR experiments demonstrate the enhanced reducibility of the x% Zr-Co_3O_4 catalysts as compared with pure Co_3O_4. Moreover, XPS and O_2-TPD analyses suggest that Zr doping resulted in more surface oxygen vacancies and adsorbed oxygen species, as well as lattice oxygen with higher mobility. As a result, the x% Zr-Co_3O_4 catalysts exhibited superior activity in propane oxidation than pure Co_3O_4. Among the doped catalysts, 1% Zr-Co_3O_4 presented the highest activity, with T_{90} of 241 °C at a WHSG of 40,000 mL g^{-1} h^{-1}.

It has been reported that propane oxidation over Co3O4-based catalysts proceeds via the MvK mechanism [9, 10, 45], in which the adsorbed propane first interacts with surface lattice oxygen, generating oxygen vacancies on the catalyst surface, then gaseous oxygen replenishes the oxygen vacancies and produces new active oxygen species for the new round of oxidation reaction. As revealed by the DRIFTS results, propane oxidation over 1% Zr-Co_3O_4 also follows this mechanism. In such a mechanism, the low-temperature reducibility, abundant active oxygen species and high oxygen mobility is required for achieving high catalytic activity toward VOCs oxidation [9, 46, 48]. As shown in Fig. 4.27a and 4.27b, a positive correlation is found between the propane oxidation rate and the low temperature reducibility and the content of O_β of the catalysts. Fig. 4.27c shows the propane oxidation rate, the surface Co^{2+}/Co^{3+} ratio, and the surface O_{ads}/O_{latt} ratio as a function of the Zr/(Co + Zr) ratio, in which all the profiles were found to be typical volcano-type curves. The catalytic activity of the catalysts correlates well with the surface vacancy concentration and the amount of surface adsorbed oxygen species, suggesting the key role of active oxygen species in the total oxidation of propane.

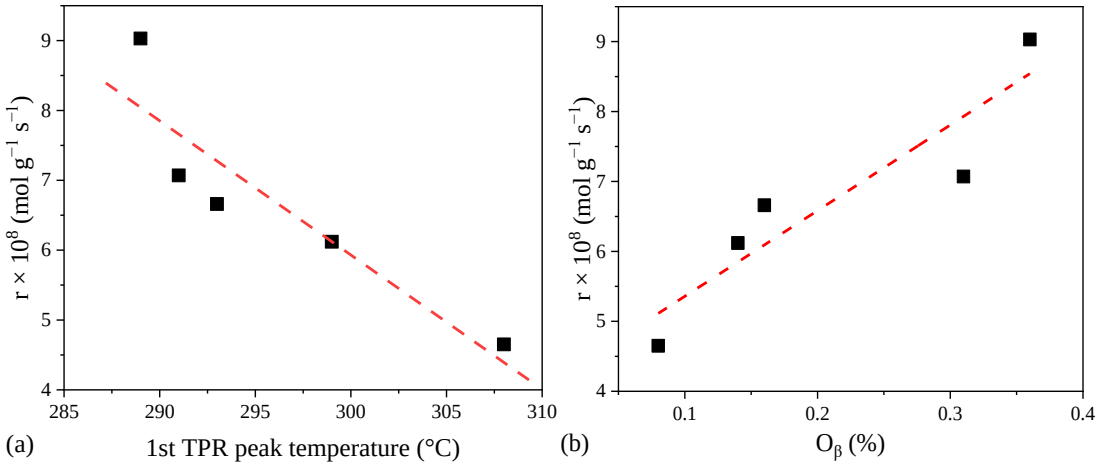

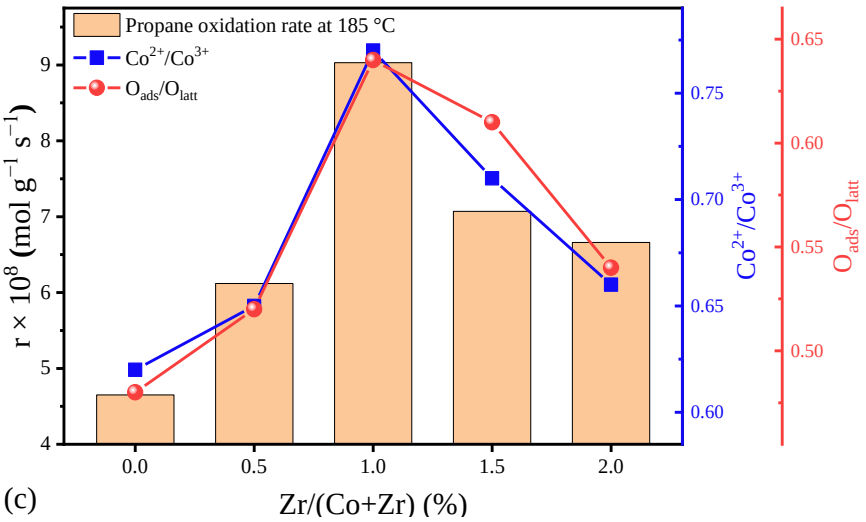

Fig. 4.27 The relationship between the propane oxidation rate and (a) the low temperature reducibility and (b) the content of O_β. (c) The correlation between propane oxidation rate (at 185 °C) and surface species concentration of the x% Zr-Co_3O_4 catalysts.

During the reaction, the larger SSA of the catalysts usually favors the adsorption of reactant molecules, since it can provide more active sites. It seems that SSA plays an important role in the enhancement of the catalytic performance of the Zr-doped catalysts. This is reasonable because the increase in SSA is accompanied by an increase in surface active oxygen species and more low-temperature reducible Co_3O_4 species as discussed in the manuscript. However, following the MvK mechanism, SSA is not the critical factor determining the catalytic activity. In this work, 1% Zr-Co_3O_4 exhibited the most defective structure, the best redox ability, and the largest concentration of oxygen vacancies and adsorbed oxygen species, thus showed remarkable catalytic activity in both propane and toluene oxidation. Special attention should be paid to the fact that 2% Zr-Co_3O_4 showed much lower activity of propane oxidation than 1.5% Zr-Co_3O_4, though they possessed similar crystallite size, SSA and reducibility. This can be explained by the big difference in the content of active oxygen species. The low content of superficial active oxygen species of 2% Zr-Co_3O_4 is responsible for its low activity.

Our study shows that doping a small amount of non-reducible Zr into the Co_3O_4 catalyst can greatly promote its VOCs oxidation activity, which sheds light on the development of other highly active catalysts for the removal of VOCs.

4.4 Conclusions

Firstly, a series of Zr-modified Co_3O_4 catalysts (Zr/(Zr + Co) mole ratio is 5-20%) were prepared by the sol-gel method, and characterization techniques, such as XRD, N_2-orption, SEM, H_2-TPR, NH_3-TPD and XPS, were used to investigate the crystal phase, specific surface area, crystallite size, morphology, reducibility, surface acidity and surface composition of the catalysts. The catalytic oxidation of VC was used as a model reaction to test the activity of the synthesized catalysts. The main conclusions are as follows:

1. Compared with pure Co_3O_4 catalyst, the Zr-modified Co_3O_4 catalyst showed better activity for the catalytic oxidation of VC. The most active catalyst is $Co_{95}Zr_5$, with T_{50} and T_{90} of 261 and 294 ℃, respectively. The polychlorinated by-products are also completely oxidized below 360 ℃.

2. With the addition of Zr, the crystallite size of Co_3O_4 decreases gradually, and the specific surface area increases. Combined with the SEM results, the presence of Zr may prevent the sintering of Co_3O_4 during the preparation of catalyst and inhibit the growth of Co_3O_4 particles. However, based on the analysis of the catalytic activity of the catalysts for VC

oxidation, crystallite size and specific surface area may not be the key factors affecting the catalytic activity in this work. Excessive Zr dispersion on the surface of Co_3O_4 may cover some of the active sites, thus negatively influencing the adsorption and activation of reactant molecules and inhibiting the activity of the catalysts.

3. The addition of Zr significantly improved the reducibility of Co_3O_4. At the same time, the surface acidity of Co_3O_4 was greatly enhanced by adding Zr. XPS results showed that there were more Co^{2+} and adsorbed oxygen species on the surface of the Zr-modified Co_3O_4 catalyst, indicating that the addition of Zr increased the oxygen vacancy concentration on the surface of Co_3O_4, which was conducive to the adsorption and activation of oxygen, and promoted the formation of active oxygen species and the oxygen mobility.

Another series of Zr-doped Co_3O_4 catalysts (molar ratio of Zr/(Zr + Co) is 0.5-2%) were prepared by sol-gel method. The catalysts were characterized by XRD, Raman, FT-IR, N_2-sorption, H_2-TPR, O_2-TPD and XPS, and applied in the catalytic oxidation of propane. The main conclusions are as follows:

1. Only a small amount of Zr can be doped into the lattice of Co_3O_4. When the Zr content increases, it tends to form ZrO_x on the surface of the catalyst. Excessive Zr would result in the decrease of the actual doping amount of Zr.

2. The moderate doping of Zr in Co_3O_4 can lead to a strong interaction between Zr dopant and Co_3O_4, resulting in smaller crystallite size, larger specific surface area, higher content of surface Co^{2+}, more defect structures and better reducibility of Co_3O_4. Meanwhile, the formation of active oxygen species and oxygen mobility of Co_3O_4 are also enhanced.

3. Zr doping significantly improves the activity of Co_3O_4 catalyst. When the doping amount is the largest, the catalytic activity of the catalyst for propane oxidation is the best (1%Zr-Co_3O_4), with T_{50} and T_{90} of 219 and 249 ℃ respectively. The origin can be mainly traced to the excellent low temperature reducibility and abundance of surface active oxygen species.

4. The catalytic oxidation of propane over 1%Zr-Co_3O_4 obeys Mars-van Krevelen mechanism, as investigated by DRIFT spectroscopy experiments.

References

[1] W. Zhang, F. Wu, J. Li, Z. You. Dispersion-precipitation synthesis of highly active nanosized Co_3O_4 for catalytic oxidation of carbon monoxide and propane. Applied Surface Science. 2017, 411: 136-143.

[2] L.F. Liotta. Catalytic oxidation of volatile organic compounds on supported noble metals. Applied Catalysis B: Environmental. 2010, 100: 403-412.

[3] B. Puértolas, A. Smith, I. Vázquez, A. Dejoz, A. Moragues, T. Garcia, B. Solsona. The different catalytic behaviour in the propane total oxidation of cobalt and manganese oxides prepared by a wet combustion procedure. Chemical Engineering Journal. 2013, 229: 547-558.

[4] M.N. Taylor, W. Zhou, T. Garcia, B. Solsona, A.F. Carley, C.J. Kiely, S.H. Taylor. Synergy between tungsten and palladium supported on titania for the catalytic total oxidation of propane. Journal of Catalysis. 2012, 285: 103-114.

[5] D. Delimaris, T. Ioannides. VOC oxidation over MnO_x-CeO_2 catalysts prepared by a combustion method. Applied Catalysis B: Environmental. 2008, 84: 303-312.

[6] U. Menon, V.V. Galvita, G.B. Marin, Reaction network for the total oxidation of toluene over CuO-CeO_2/Al_2O_3. Journal of Catalysis. 2011, 283: 1-9.

[7] J. Chen, X. Chen, W. Xu, Z. Xu, J. Chen, H. Jia, J. Chen. Hydrolysis driving redox reaction to synthesize Mn-Fe binary oxides as highly active catalysts for the removal of toluene. Chemical Engineering Journal. 2017, 330: 281-293.

[8] Z. Hu, S. Qiu, Y. You, Y. Guo, Y. Guo, L. Wang, W. Zhan, G. Lu. Hydrothermal synthesis of NiCeOx nanosheets and its application to the total oxidation of propane. Applied Catalysis B: Environmental. 2018, 225: 110-120.

[9] W. Zhu, X. Chen, J. Jin, X. Di, C. Liang, Z. Liu. Insight into catalytic properties of Co_3O_4-CeO_2 binary oxides for propane total oxidation. Chinese Journal of Catalysis. 2020, 41: 679-690.

[10] W. Zhang, J. Díez-Ramírez, P. Anguita, C. Descorme, J. L. Valverde, A. Giroir-Fendler. Nanocrystalline Co_3O_4 catalysts for toluene and propane oxidation: Effect of the precipitation agent. Applied Catalysis B: Environmental. 2020, 273: 118894.

[11] L. Ma, Y. Geng, X. Chen, N. Yan, J. Li, J.W. Schwank. Reaction mechanism of propane oxidation over Co_3O_4 nanorods as rivals of platinum catalysts. Chemical Engineering Journal. 2020, 402: 125911.

[12] Y. Xia, H. Dai, H. Jiang, L. Zhang. Three-dimensional ordered mesoporous cobalt oxides: highly active catalysts for the oxidation of toluene and methanol. Catalysis Communications. 2010, 11: 1171-1175.

[13] L. Hu, Q. Peng, Y. Li. Selective synthesis of Co_3O_4 nanocrystal with different shape and crystal plane effect on catalytic property for methane combustion. Journal of the American Chemical Society. 2008, 130: 16136-16137.

[14] J. Li, X. Xu, Z. Hao, W. Zhao. Mesoporous silica supported cobalt oxide catalysts for catalytic removal of benzene. Journal of Porous Materials. 2008, 15: 163-169.

[15] T. Cai, H. Huang, W. Deng, Q. Dai, W. Liu, X. Wang. Catalytic combustion of 1,2-dichlorobenzene at low temperature over Mn-modified Co_3O_4 catalysts. Applied Catalysis B: Environmental. 2018, 166-167: 393-405.

[16] Y.Z. Wang, Y.X. Zhao, C.G. Gao, D.S. Liu. Preparation and catalytic performance of Co_3O_4 catalysts for low-temperature CO oxidation. Catalysis Letters. 2007, 116: 136-142.

[17] B. Bai, H. Arandiyan, J. Li. Comparison of the performance for oxidation of formaldehyde on nano-Co_3O_4, 2D-Co_3O_4, and 3D-Co_3O_4 catalysts. Applied Catalysis B: Environmental. 2013, 142-143: 677-683.

[18] Y. Lou, J. Ma, X. Cao, L. Wang, Q. Dai, Z. Zhao, Y. Cai, W. Zhan, Y. Guo, P. Hu, G. Lu, Y. Guo. Promoting effects of In_2O_3 on Co_3O_4 for CO oxidation: tuning O_2 activation and CO adsorption strength simultaneously. ACS Catalysis. 2014, 4: 4143-4152.

[19] C. Wang, C. Zhang, W. Hua, Y. Guo, G. Lu, S. Gil, A. Giroir-Fendler. Catalytic oxidation of vinyl chloride emissions over Co-Ce composite oxide catalysts. Chemical Engineering Journal. 2017, 315: 392-402.

[20] M.P. Kapoor, A. Raj, Y. Matsumura. Methanol decomposition over palladium supported mesoporous CeO_2-ZrO_2 mixed oxides. Microporous and Mesoporous Materials. 2001, 44-45: 565-572.

[21] H.F. Lu, Y. Zhou, W.F. Han, H.F. Huang, Y.F. Chen. High thermal stability of ceria-based mixed oxide catalysts supported on ZrO_2 for toluene combustion. Catalysis Science & Technology. 2013, 3: 1480-1484.

[22] F. Wyrwalski, J.F. Lamonier, M.J. Perez-Zurita, S. Siffert, A. Aboukaïs. Influence of the ethylenediamine addition on the activity, dispersion and reducibility of cobalt oxide catalysts supported over ZrO_2 for complete VOC oxidation. Catalysis Letters. 2006, 108: 87-95.

[23] V.R. Choudhary, G.M. Deshmukh, S.G. Pataskar. Low-temperature complete combustion of a dilute mixture of methane and propane over transition-metal-doped ZrO_2 catalysts: Effect of the presence of propane on methane combustion. Environmental Science & Technology. 2005, 39: 2364-2368.

[24] Y. Wang, R. Wu, Y. Zhao. Effect of ZrO_2 promoter on structure and catalytic activity of the Ni/SiO_2 catalyst for CO methanation in hydrogen-rich gases. Catalysis Today. 2010, 158: 470-474.

[25] T. Wang, C. Li, L. Zhao, J. Zhang, S. Li, G. Zeng. The catalytic performance and characterization of ZrO_2 support modification on CuO-CeO_2/TiO_2 catalyst for the simultaneous removal of Hg^0 and NO. Applied Surface Science. 2017, 400: 227-237.

[26] Z. Pu, Y. Liu, H. Zhou, W. Huang, Y. Zheng, X. Li. Catalytic combustion of lean methane at low temperature over ZrO_2-modified Co_3O_4 catalysts. Applied Surface Science. 2017, 422: 85-93.

[27] B. de Rivas, R. López-fonseca, C. Jiménez-González, J.I. Gutiérrez-ortiz. Synthesis, characterization and catalytic performance of nanocrystalline Co_3O_4 for gas-phase chlorinated VOC abatement. Journal of Catalysis. 2011, 281: 88-97.

[28] H. Liu, X. Li, Q. Dai, H. Zhao, G. Chai, Y. Guo, Y. Guo, L. Wang, W. Zhan. Catalytic oxidation of chlorinated volatile organic compounds over Mn-Ti composite oxides catalysts: Elucidating the influence of surface acidity. Applied Catalysis B: Environmental. 2021, 282: 119577.

[29] P. Yang, S. Fan, Z. Chen, G. Bao, S. Zuo, C. Qi. Synthesis of Nb_2O_5 based solid superacid materials for catalytic combustion of chlorinated VOCs. Applied Catalysis B: Environmental. 2018, 239: 114-124.

[30] Z.Y. Tian, P.H. Tchoua Ngamou, V. Vannier, K. Kohse-Höinghaus, N. Bahlawane. Catalytic oxidation of VOCs over mixed Co-Mn oxides. Applied Catalysis B: Environmental. 2012, 117-118: 125-134.

[31] H. Wu, G. Pantaleo, G. Di Carlo, S. Guo, G. Marci, P. Concepción, A.M. Venezia, L.F. Liotta. Co_3O_4 particles grown over nanocrystalline CeO_2: influence of precipitation agents and calcination temperature on the catalytic activity for methane oxidation. Catalysis Science & Technology. 2015, 5: 1888-1901.

[32] L. Li, W. Wang. Synthesis and characterization of monoclinic ZrO_2 nanorods by a novel and simple precursor thermal decomposition approach. Solid State Communications. 2003, 127: 639-643.

[33] A. Alvarez, S. Ivanova, M.A. Centeno, J.A. Odriozola. Sub-ambient CO oxidation over mesoporous Co_3O_4: effect of morphology on its reduction behavior and catalytic performance. Applied Catalysis A, General. 2012, 431-432: 9-17.

[34] W. Deng, Q. Dai, Y. Lao, B. Shi, X. Wang. Low temperature catalytic combustion of 1,2-dichlorobenzene over CeO_2-TiO_2 mixed oxide catalysts. Applied Catalysis B: Environmental. 2016, 181: 848-861.

[35] J. González-Prior, R. López-Fonseca, J.I. Gutiérrez-Ortiz, B. de Rivas. Oxidation of 1,2-dichloroethane over nanocube-shaped Co_3O_4 catalysts. Applied Catalysis B: Environmental. 2016, 199: 384-393.

[36] Z. Zhu, G. Lu, Z. Zhang, Y. Guo, Y. Guo, Y. Wang. Highly active and stable Co_3O_4/ZSM-5 catalyst for propane oxidation: Effect of the preparation method. ACS Catalysis. 2013, 3: 1154-1164.

[37] Z. Sihaib, F. Puleo, J.M. Garcia-Vargas, L. Retailleau, C. Descorme, L.F. Liotta, J.L. Valverde, S. Gil, A. Giroir-Fendler. Manganese oxide-based catalysts for toluene oxidation. Applied Catalysis B: Environmental. 2017, 209: 689-700.

[38] C. Zhang, Y. Guo, Y. Guo, G. Lu, A. Boreave, L. Retailleau, A. Baylet, A. Giroir-Fendler. $LaMnO_3$ perovskite oxides prepared by different methods for catalytic oxidation of toluene. Applied Catalysis B: Environmental. 2017, 148-149: 490-498.

[39] L.F. Liotta, G. Di Carlo, G. Pantaleo, G. Deganello. Catalytic performance of Co_3O_4/CeO_2 and Co_3O_4/CeO_2-ZrO_2 composite oxides for methane combustion: Influence of catalyst pretreatment temperature and oxygen concentration in the reaction mixture. Applied Catalysis B: Environmental. 2007, 70: 314-322.

[40] S. Guo, F. Puleo, L. Wang, H. Wu, L.F. Liotta. $La_{0.6}Sr_{0.4}Co_{0.2}Fe_{0.79}M_{0.01}O_{3-\delta}$ (M = Ni, Pd) perovskites synthesized by citrate-EDTA method: oxygen vacancies effect on electrochemical properties. Advanced Powder Technology. 2018, 29: 2804-2812.

[41] H. Zhao, W. Han, F. Dong, Z. Tang. Highly-efficient catalytic combustion performance of 1,2-dichlobenzene over mesoporous TiO_2-SiO_2 supported CeMn oxides: the effect of acid sites and redox sites. Journal of Industrial and Engineering Chemistry. 2018, 64: 194-205

[42] Z. Shang, M. Sun, S. Chang, X. Che, X. Cao, L. Wang, Y. Guo, W. Zhan, Y. Guo, G. Lu. Activity and stability of Co_3O_4-based catalysts for soot oxidation: the enhanced effect of Bi_2O_3 on activation and transfer of oxygen. Applied Catalysis B: Environmental. 2017, 209: 33-44.

[43] W. Li, X. Nie, X. Jiang, A. Zhang, F. Ding, M. Liu, Z. Liu, X. Guo, C. Song. ZrO_2 support imparts superior activity and stability of Co catalysts for CO_2 methanation. Applied Catalysis B: Environmental. 2018, 220: 397-408.

[44] W. Huang, Y. Liu, Z. Wu. Enhanced stability of HZSM-5 supported copper oxides by Na doping for catalytic combustion of propene. Catalysis Communications. 2019, 122: 58-62.

[45] Z. Ren, Z. Wu. W. Song, W. Xiao, Y. Guo, J. Ding, S.L. Suib, P.X. Gao. Low temperature propane oxidation over Co_3O_4 based nano-array catalysts: Ni dopant effect, reaction mechanism and structural stability. Applied Catalysis B: Environmental. 2016, 180: 150-160.

[46] W. Liu, R. Liu, X. Zhang. Controllable synthesis of 3D hierarchical Co_3O_4 catalysts and their excellent catalytic performance for toluene oxidation. Applied Surface Science. 2020, 507: 145174.

[47] F. Wang, H. Dai, J. Deng, S. Xie, H. Yang, W. Han. Nanoplate-aggregate Co_3O_4 microspheres for toluene combustion. Chinese Journal of Catalysis. 2014, 35: 1475-1481.

[48] W. Tang, J. Weng, X. Lu, L. Wen, A. Subramanian, C.Y. Nam, P.X. Gao. Alkali-metal poisoning effect of total CO and propane oxidation over Co_3O_4 nanocatalysts. Applied Catalysis B: Environmental. 2019, 256: 117859.

Chapter 5 The preparation and catalytic performance of the Nb-doped Co_3O_4 catalysts

5.1 Introduction

The study in Chapter 4 shows that appropriate Zr doping significantly changes the physicochemical properties of the Co_3O_4 catalyst, and then affects its catalytic activity for propane oxidation. It is found that there is a maximum doping amount of Zr into Co_3O_4. Zr will preferentially form ZrO_x on the catalyst surface when the doping amount is higher than this amount, resulting in reducing its actual doping amount. Therefore, we suspect that the same phenomenon may occur when Co_3O_4 is doped with other metal elements.

Due to the rich surface acidity, NbO_x has attracted a certain amount of attention in the catalytic oxidation of CVOCs [1-2]. Yang et al. [1] prepared a series of composite oxide catalysts, $(Ce,Cr)_xO_2/MO_y$ (M = Ti, V, Nb, Mo, W, La) by the deposition-precipitation method, and applied these catalysts in the catalytic oxidation of 1,2-dichloroethane. It was found that the $(Ce,Cr)_xO_2/Nb_2O_5$ catalyst showed the best catalytic activity and stability. Subsequently, they prepared Nb_2O_5-based solid superacid catalysts for the catalytic oxidation of 1,2-dichloroethane by sol-gel method [2], and found that the porous structure and surface acidity of the catalyst promoted the adsorption, activation and scission of the C-Cl bond. The reductive sites enhanced the deep oxidation of by-products or intermediate species in the reaction.

In this chapter, a series of Nb-doped Co_3O_4 catalysts were prepared by sol-gel method, in which the molar ratio of Nb/(Nb + Co) was 0.5-1.5%. They were used for the catalytic oxidation of propane and VC, respectively. The catalytic activity and stability of the catalysts were evaluated. Meanwhile, the catalysts were characterized by XRD, Raman, FT-IR, N_2-sorption, H_2-TPR, NH_3-TPD and XPS, et al. The relationship between the physicochemical properties and the catalytic performance was studied.

5.2 Preparation of catalysts

A series of Nb-doped Co_3O_4 catalysts was synthesized via a sol-gel method using CA as the complexing agent. Typically, cobalt nitrate hexahydrate ($Co(NO_3)_2{\cdot}6H_2O$) and Ammonium niobate oxylate hydrate ($C_4H_4NNbO_9{\cdot}xH_2O$) were dissolved in 50 mL of distilled water. Then CA was added into the solution where the molar ratio of CA/(Co + Nb) was kept at 1.2. After complete dissolution of CA, the mixture was heated to 80 °C in a water bath and maintained at this temperature under stirring, until gel formation. After that, the gel was dried overnight in an oven at 120 °C to get a spongelike material that was calcined in a muffle

furnace at 200 °C for 2 h, and then at 500 °C for 2 h with a rate of 2 °C min^{-1}. The obtained catalysts were denoted by x% Nb-Co_3O_4 (x = 0.5, 1, 1.5), where x% represents the molar ratio of Nb/(Co + Nb). For the purpose of comparison, pure Co_3O_4 and NbO_x were prepared by the same method.

5.3 Evaluation of catalysts

The catalyst evaluation method is described in Chapter 2, Section 2.5.1 and 2.5.2.

5.4 Catalytic performance of catalysts

Firstly, the catalytic activity of propane oxidation over the x% Nb-Co_3O_4 catalyst was investigated. The propane conversion curves versus temperature are plotted in Fig. 5.1a, and the T_{50} and T_{90} data in the reaction process are listed in Table 5.1. Niobium oxide showed almost no activity for propane oxidation under experimental conditions. The other catalysts exhibited relatively high catalytic activity for propane oxidation, and the Nb-doped catalysts showed better activity than pure Co_3O_4. For example, the T_{50} and T_{90} of pure Co_3O_4 for propane oxidation are 229 and 269 °C, respectively. While the T_{50} and T_{90} of 1% Nb-Co_3O_4 decrease to 210 and 239 °C, respectively. At the same time, it was found that the doping amount of Nb significantly affected the catalytic activity of the catalysts for propane oxidation. With the increase of Nb doping amount, the T_{50} and T_{90} of the catalysts for propane oxidation gradually decreased, and 1% Nb-Co_3O_4 catalyst showed the best catalytic activity. However, when Nb doping exceeds 1%, the activity of the catalysts began to decline. The T_{50} and T_{90} of 1.5% Nb-Co_3O_4 were 215 and 246 °C, respectively. For the complete oxidation of propane, the order of the catalytic activity of the x% Nb-Co_3O_4 catalysts is as follows: 1% Nb-Co_3O_4 > 1.5% Nb-Co_3O_4 > 0.5% Nb-Co_3O_4 > Co_3O_4.

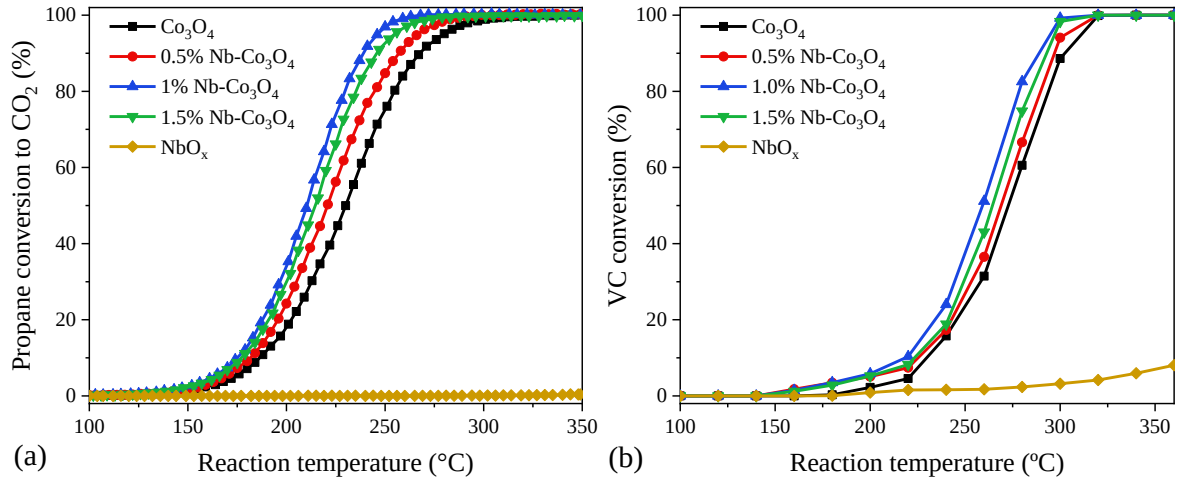

Fig. 5.1 Light-off curves of (a) propane oxidation and (b) VC oxidation over the synthesized x% Nb-Co_3O_4 catalysts. Reaction condition: 1000 ppm propane or VC and synthetic air (propane oxidation) or air (VC oxidation) balance; WHSV = 40000 (propane oxidation) or 30000 (VC oxidation) mL g^{-1} h^{-1}.

Then the x% Nb-Co_3O_4 catalysts were applied in the catalytic oxidation of VC. The VC conversion curves versus temperature are shown in Fig. 5.1b, and the T_{50} and T_{90} data in the reaction process are listed in Table 5.1. Different from propane oxidation, niobium oxide showed a certain activity for VC oxidation from 200 °C and could achieve ~ 8% conversion of VC at 360 °C. The other catalysts exhibited relatively high catalytic activity for VC oxidation. For example, 1% Nb-Co_3O_4 catalyst can completely convert VC at 300 °C, while pure Co_3O_4 requires a higher reaction temperature (~ 320 °C). At the same time, it was found that the doping amount of Nb had a certain effect on the catalytic performance of the catalysts for VC oxidation. With the increase of the Nb doping amount, the catalytic activity of the catalysts gradually increased, and 1% Nb-Co_3O_4 showed the best catalytic activity. However, when Nb doping exceeds 1%, the activity of the catalyst began to decline. For the complete conversion of VC, the catalytic activity sequence of the x%Nb-Co_3O_4 catalysts is 1% Nb-Co_3O_4 > 1.5% Nb-Co_3O_4 > 0.5% Nb-Co_3O_4 > Co_3O_4, which is consistent with the sequence of propane oxidation activity.

The reaction rates of the catalysts for propane and VC oxidation were calculated at 190 and 225 °C, respectively, and the results are listed in Table 5.1. It can be found that 1% Nb-Co_3O_4 has the highest reaction rates both for propane and VC oxidation.

Table 5.1 T_{50}, T_{90}, and reaction rates of the synthesized x% Nb-Co_3O_4 catalysts in propane and VC oxidation, respectively.

Catalyst	Propane			VC		
	T_{50} (°C)	T_{90} (°C)	$r \times 10^8$ (mol g^{-1} s^{-1})	T_{50} (°C)	T_{90} (°C)	$r \times 10^8$ (mol g^{-1} s^{-1})
Co_3O_4	229	269	5.94	273	303	3.60
0.5%Nb-Co_3O_4	221	257	7.63	269	297	4.82
1%Nb-Co_3O_4	210	239	11.26	259	288	6.80
1.5%Nb-Co_3O_4	215	246	9.64	264	293	5.33

In Chapter 4, it was found that many polychlorinated by-products appeared in the process of VC oxidation on Co_3O_4-based catalysts. Therefore, we also analyzed the by-products of catalytic oxidation of VC on the x% Nb-Co_3O_4 catalysts. Fig. 5.2 shows the by-products concentration curves versus reaction temperature during the reaction process. These polychlorinated by-products can be oxidized to carbon dioxide, water, and hydrogen chloride or chlorine gas at higher reaction temperatures. Among all the catalysts, 1% Nb-Co_3O_4 and 1.5% Nb-Co_3O_4 showed the best catalytic performance, with all the by-products completely oxidized at 340 °C. In particular, the type of polychlorinated by-products on the 1% Nb-Co_3O_4 and 1.5% Nb-Co_3O_4 catalysts was one less than that on pure Co_3O_4, with no CCl_4 produced during the whole reaction process. It indicated that Nb doping can inhibit the deep chlorination of intermediate species during the catalytic oxidation of VC. Apart from the chlorinated by-products, the other chlorine species were all transformed into HCl and/or Cl_2. A titration method [3, 4] was used to investigate the Cl_2 concentration over the most active catalyst, 1% Nb-Co_3O_4. The HCl concentration was calculated by the difference between the conversion concentration of VC and the other chlorinated products concentrations. The selectivity of HCl and Cl_2 in all the chlorinated products were shown in Fig. 5.2e. There was nearly no Cl_2 formed under 280 °C. however, the selectivity of Cl_2 began to increase from 280 °C and reached to 15.5% at 360 °C, which was attributed to the increasing Deacon reaction. The selectivity of HCl decreased below 240 °C mainly due to the increase of chlorinated organic by-products. When they were totally oxidized at higher temperature, the selectivity of HCl rose up to 84.5%.

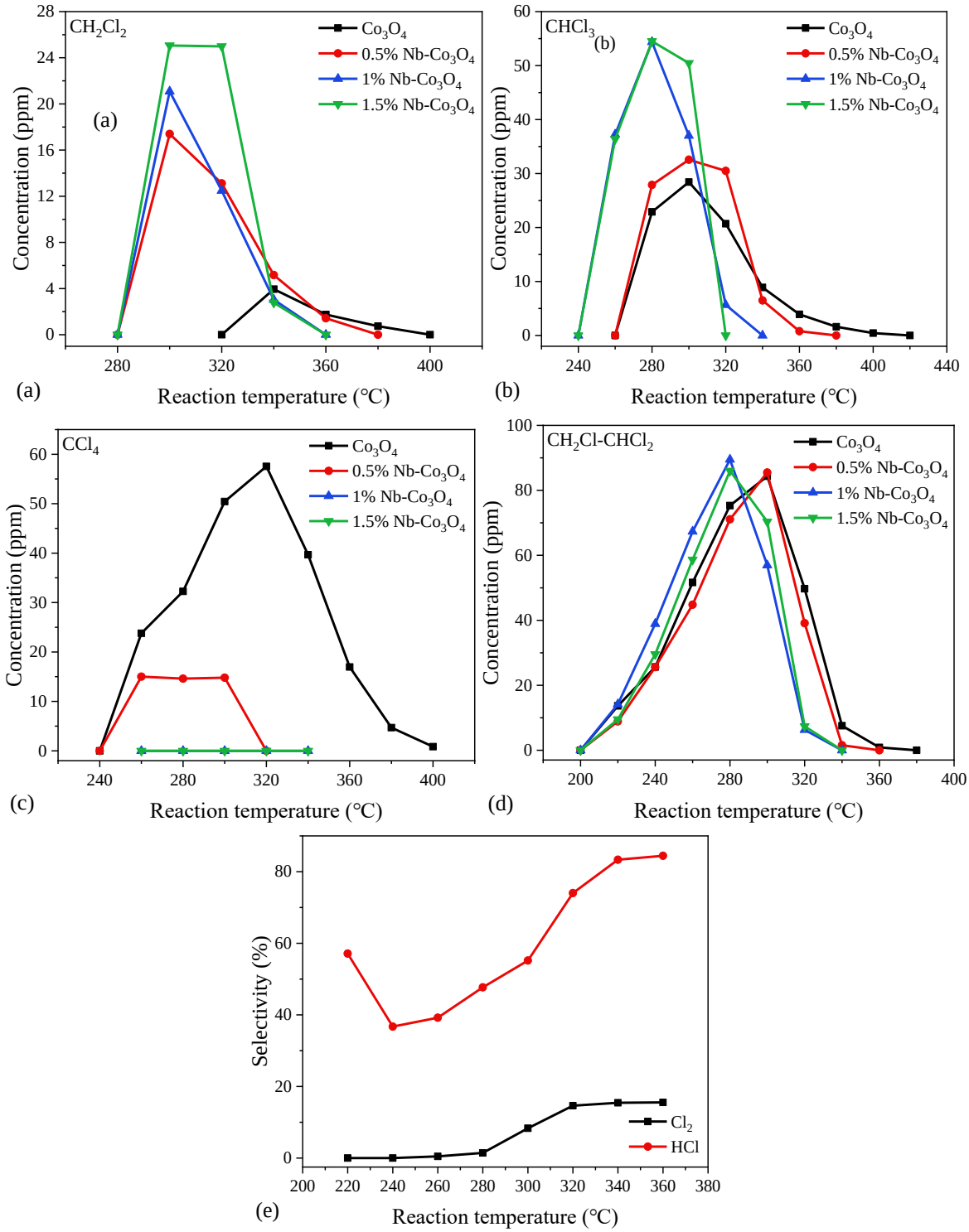

Fig. 5.2 (a-d) Concentrations of chlorinated by-products of VC oxidation over the synthesized x% Nb-Co_3O_4 catalysts, and (e) the selectivity of HCl and Cl_2 of VC oxidation on 1%Nb-Co_3O_4. Reaction condition: 1000 ppm VC and air balance; WHSV = 30000 mL g^{-1} h^{-1}.

For the stability tests of propane and VC oxidation on 1% Nb-Co_3O_4, the conversion of propane and VC during the tests are shown in Fig. 5.3. It can be seen that under the two reaction temperatures selected, the conversion of propane decreased slightly at the initial stage, and then remained unchanged. The results showed that the stability of 1% Nb-Co_3O_4 in propane

oxidation was relatively good. For the catalytic oxidation of VC, the conversion of VC decreased at the beginning of the test at the relatively low temperature (280 °C), and then remained basically unchanged. The stability of the catalyst was very good at the temperature of 340 °C. No decrease of the VC conversion was observed during the whole test (~ 75 hours), which remained at 100% all the time. It indicated that the catalyst could maintain relatively high stability in the catalytic oxidation of VC.

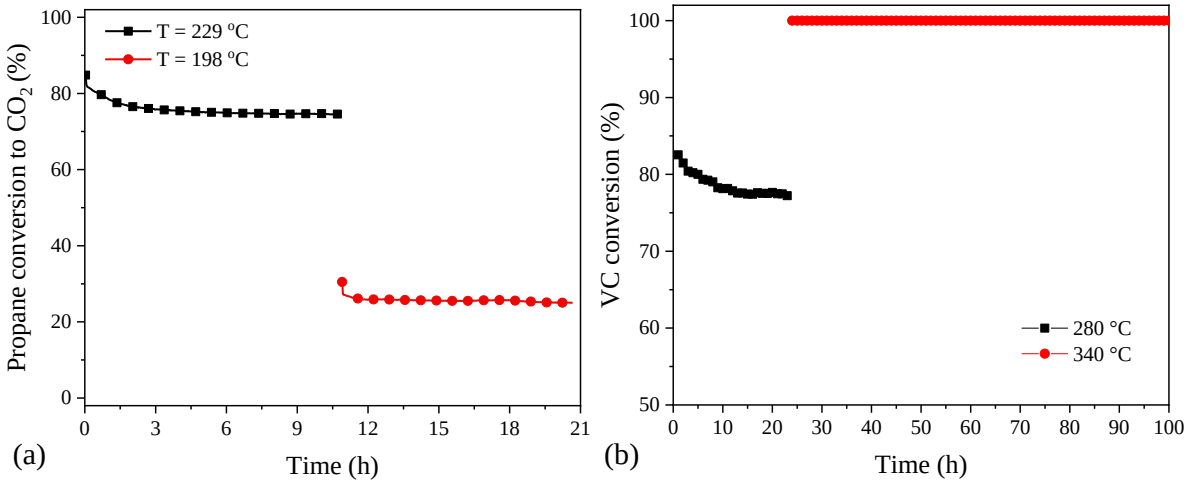

Fig. 5.3 Stability tests of (a) propane oxidation and (b) VC oxidation over the 1%Nb-Co_3O_4 catalyst. Reaction condition: 1000 ppm propane or VC and synthetic air (propane oxidation) or air (VC oxidation) balance; WHSV = 40000 (propane oxidation) or 30000 (VC oxidation) mL g^{-1} h^{-1}.

The influence of WHSV on the catalytic performance of propane and VC oxidation over 1% Nb-Co_3O_4 was investigated. The results are shown in Figure 5.4. When WHSV increases, the residence time of reactants through the catalyst bed decreases, thus causing negative effects on the catalytic oxidation of propane and VC. As expected, the conversion curves of the catalytic oxidation of propane and VC over 1% Nb-Co_3O_4 moved towards high temperature as the increase of WHSV. However, it can be found that the complete conversion of propane can still be completed below 300 °C even at the WHSV as high as 160000 mL g^{-1} h^{-1}. At the WHSV of 120,000 mL g^{-1} h^{-1}, VC can be completely converted below 340 °C, indicating that 1%Nb-Co_3O_4 had excellent catalytic performance for propane and VC oxidation.

On the other hand, the effect of water on the catalytic performance of propane and VC over 1%Nb-Co_3O_4 was examined. The results are shown in Figure 5.4. It can be seen that when 4 vol.% water was introduced into the feed gas, the propane conversion efficiency was severely inhibited, and the T_{90} for propane oxidation raised to 267 °C, which was 28 °C higher than that under dry conditions. The inhibition of water on propane oxidation over 1% Nb-Co_3O_4 was also observed when higher water contents (6 and 8 vol.%) were introduced. However, the activity of 1% Nb-Co_3O_4 for propane oxidation was basically the same when three different water content were introduced. It indicated that the inhibition of the catalytic activity would not

increase with the presence of more water content in a certain range. The decreased activity may be caused by the competitive adsorption of water and propane molecules at the active sites of the catalyst [5]. For VC oxidation, the catalytic activity of 1% Nb-Co_3O_4 was inhibited at low temperature when two different contents of water (2.3 and 4.7 vol.%) were introduced, and the inhibition effects were basically the same, indicating that within a certain range, water content had little effect on the catalytic activity inhibition of 1%Nb-Co_3O_4. However, with the increase of the temperature, the inhibition of water disappeared gradually, and the complete conversion temperature of VC was almost the same as that under dry condition. Considering the reasons for this phenomenon, the competitive adsorption of water and VC molecules still existed. However, the adsorption of water on the catalyst surface made the surface hydroxyl increase, which may make it easier for the generation of hydrogen chloride. The removal of the Cl species from the catalyst surface was thus accelerated, so that the catalytic activity at the high temperature can keep consistent with that under dry conditions. A titration method was used to measure the concentration of chlorine gas in the outlet gas when 2.3 and 4.7 vol. % water were introduced into the fed gas. The results showed that only hydrogen chloride was produced in the final products, which verified our above speculation. It can also be seen from the subsequent experimental results that when water was removed from the feed gas, the catalytic activity of 1% Nb-Co_3O_4 for propane and VC oxidation can basically return to the initial state, indicating that water has no destructive effect on the structure of the catalyst.

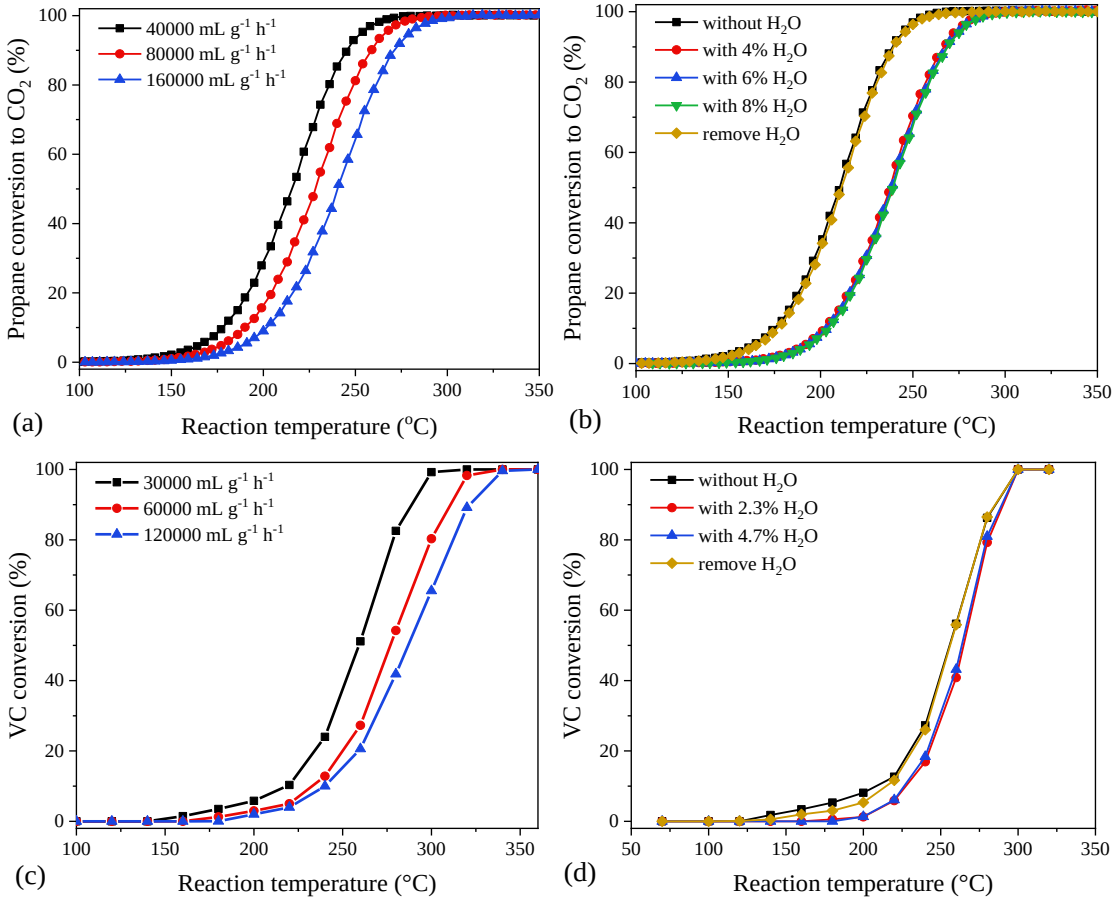

Fig. 5.4 Effect of WHSV and water vapor on (a, b) propane oxidation and (c, d) VC oxidation over the 1%Nb-Co_3O_4 catalyst.

At the same time, the polychlorinated by-products in VC oxidation with the presence of 2.3 and 4.7 vol.% water were analyzed, and the results are shown in Figure 5.5. It can be seen that when water was introduced, the concentration of dichloromethane byproduct hardly changed, while the formation of trichloromethane and 1,2,2-trichloroethane were inhibited to a certain extent. According to the results obtained above, the introduction of water can enhance the production of hydrogen chloride and promote the removal of chlorine species from the catalyst surface. The decrease of chlorine species on the catalyst surface made the generation of polychlorinated products difficult. Therefore, a certain amount of water introduced during VC oxidation on 1% Nb-Co_3O_4 will not have negative impact on the activity for the full conversion of VC. Moreover, the generation of the polychlorinated by-products and chlorine were restrained, which made the chlorine atoms in the feed gas finally converted to hydrogen chloride. This is beneficial to the decrease of secondary pollution and other harmful products with higher toxicity in the application of the catalysts. In the real working conditions, the presence of a certain content of water in the VOCs feed gas is inevitable, so the above results have very important practical significance.

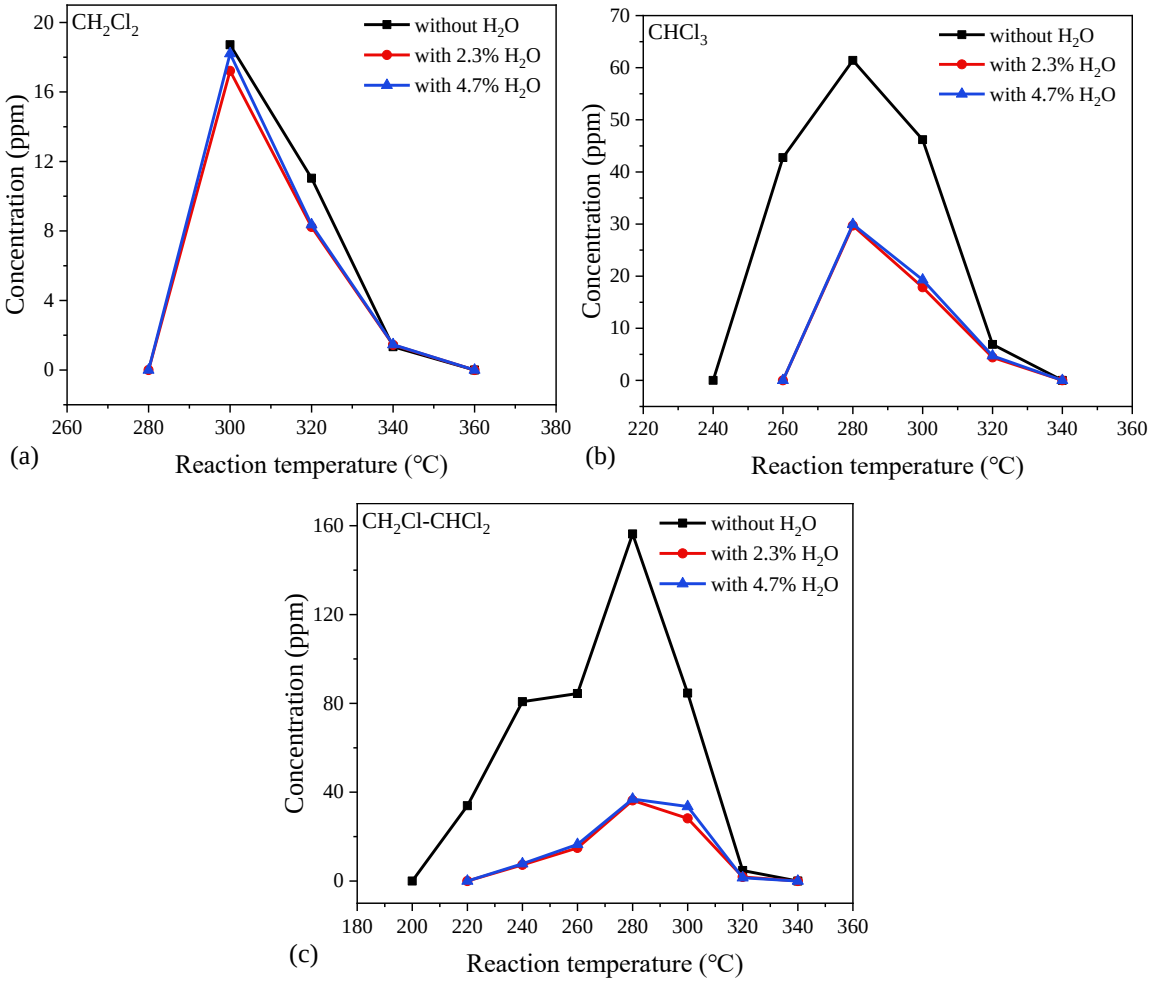

Fig. 5.5 Concentrations of chlorinated by-products of VC oxidation with or without the presence of water over the 1%Nb-Co_3O_4 catalyst.

5.5 Characterization of catalysts

Before the calcination of the dried gel powders, TGA was conducted to investigate their thermal decomposition profile and determine the correct calcination temperature. All the tested samples possessed similar weight loss curves (Fig. 5.6), with total mass loss of 65 ± 3%. Based on the above results, we have determined to use the two-step calcination of the dried powder as described in the catalyst preparation section to get the final catalysts. To determine the real contents of Nb and Co in the samples, ICP-OES analyses were performed, and the results are shown in Table 5.2.

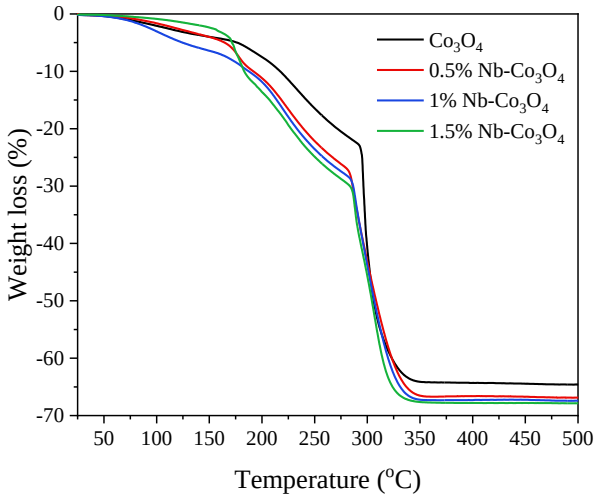

Fig. 5.6 TG curves of the dried precursors of the x%Nb-Co_3O_4 catalysts.

5.5.1 XRD

The wide-angle XRD patterns of the prepared catalysts are displayed in Fig. 4.13. For pure Co_3O_4, diffraction peaks located at 19.0°, 31.3°, 36.8°, 38.5°, 44.8°, 55.6°, 59.3° and 65.2°, corresponding to the (111), (220), (311), (222), (400), (422), (511) and (440) crystal facets, respectively, were ascribed to the cubic phase of Co_3O_4 spinel (PDF # 43-1003) [6]. NbO_x shows the XRD pattern of weak crystallization, and the diffraction peaks at 26.0°, 35.2° and 52.1° are attributed to the characteristic diffraction peaks of tetragonal phase NbO_2 (PDF # 43-1043) [7]. The Nb-doped Co_3O_4 catalysts showed crystalline features of cobalt oxide spinel and no signals due to any niobium phase were detected, which suggested the successful doping of Nb into Co_3O_4 lattice or the high dispersion of NbO_2, although we cannot exclude that it can be attributed to the low content of Nb. From the enlarged diffraction peaks of (311) crystal facet (Fig. 5.7b), it could be seen that the signals were weakened and broadened by Nb doping, suggesting the reduced crystallinity and the decrease of Co_3O_4 crystallite sizes. On the other hand, an obvious shift of the diffraction peaks of Nb-doped Co_3O_4 catalysts to smaller 2θ angles occurred, implying the lattice expansion due to Nb entering Co_3O_4 lattice [8, 9], The 1% Nb-Co_3O_4 sample showed the largest shift, suggesting that 1% represented the maximum amount of Nb that could enter into the Co_3O_4 lattice. The excess, as for 1.5% Nb-Co_3O_4, was likely as highly dispersed niobium oxide.

The average crystallite sizes and lattice constants of the samples were calculated by the Scherrer equation based on the six most intense diffraction peaks, as listed in Table 5.2. The crystallite sizes of Co_3O_4 followed the order: 1.5% Nb-Co_3O_4 < 1% Nb-Co_3O_4 < 0.5% Nb-Co_3O_4 < Co_3O_4. Pure Co_3O_4 showed the largest crystallite size of 50.4 nm and the smallest lattice constant of 8.0874 Å, whereas the crystallite size decreased, and the lattice constant increased with the doping of Nb, which was consistent with the intensities and shifts of the diffraction peaks. The smallest crystallite size equal to 28.4 nm and the largest lattice constant

of 8.0950 Å were obtained for 1% Nb-Co_3O_4. On the other hand, 1.5% Nb-Co_3O_4 showed the smaller lattice constant than 1.0% Nb-Co_3O_4, suggesting the lower doping amount of Nb. But the crystallite size of 1.5% Nb-Co_3O_4 was smaller than that of 1% Nb-Co_3O_4. On this basis, it could be argued that highly dispersed niobium oxides may inhibit Co_3O_4 crystals growth.

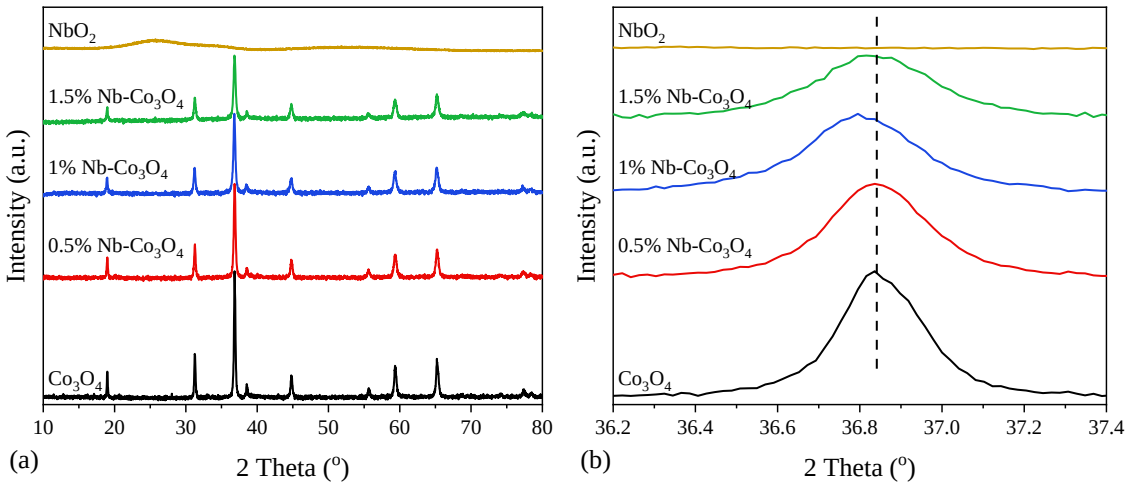

Fig. 5.7 (a) XRD patterns of the synthesized x%Nb-Co_3O_4 catalysts; (b) detail of the most intense diffraction peak of (311) crystal facet.

Table 5.2 Textural properties of the synthesized x%Nb-Co_3O_4 catalysts.

Catalyst	Nb/Co (wt. %)		d (nm)	a (Å)	SSA	V_{pore}
	Expected	Actual			($m^2\ g^{-1}$)	($cm^3\ g^{-1}$)
Co_3O_4	0/73.4	0/73.5	50.4	8.0874	7	0.039
0.5%Nb-Co_3O_4	0.6/72.9	0.4/72.4	36.4	8.0887	15	0.062
1%Nb-Co_3O_4	1.2/72.3	0.7/71.7	30.9	8.0950	26	0.089
1.5%Nb-Co_3O_4	1.7/71.7	1.1/71.3	28.4	8.0911	29	0.095
NbO_2	/	/	/	/	61	0.059

5.5.2 N_2-sorption

Fig. 5.8 shows the N_2-sorption isotherms of the x% Nb-Co_3O_4 catalysts. All the catalysts exhibited type IV isotherm with a H3 hysteresis loop, indicating the presence of mesoporous in the catalysts [10, 11]. The SSA and pore volume of the catalysts are listed in Table 5.2. NbO_2 showed the largest SSA (61 $m^2\ g^{-1}$), and the order of the SSAs for the other catalysts was as follows: 1.5% Nb-Co_3O_4 > 1% Nb-Co_3O_4 > 0.5% Nb-Co_3O_4 > Co_3O_4. The SSA of pure Co_3O_4 is only 7 $m^2\ g^{-1}$. The 1.5%Nb-Co_3O_4 catalyst exhibited a large SSA (29 $m^2\ g^{-1}$), which may be due to its lowest crystallinity and smallest crystallite size. Except for NbO_2, the total pore volume of the Nb-doped Co_3O_4 catalysts was larger than that of pure Co_3O_4(Table 5.2), and became larger with the increase of Nb doping amount. The larger SSA and pore volume can expose more active sites, which is conducive to the adsorption and activation of the reactant molecules and contributed to the catalytic activity of the catalysts.

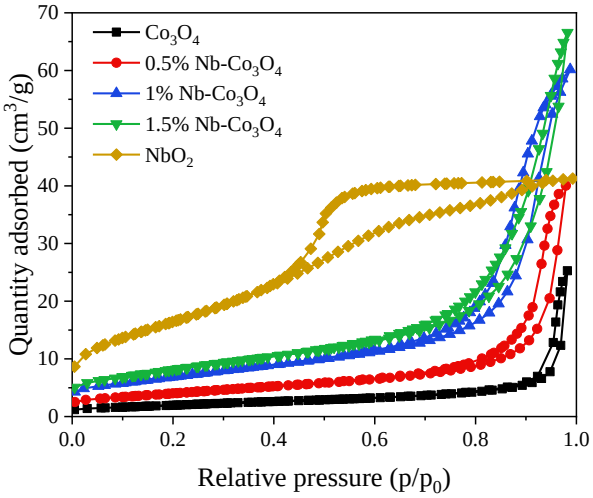

Fig. 5.8 N_2 sorption isotherms of the synthesized x%Nb-Co_3O_4 catalysts.

5.5.3 Raman

Raman spectra of the synthesized catalysts were shown in Fig. 5.9. Pure Co_3O_4 presented five well-defined bands at around 194 (F_{2g}^1), 488 (E_g), 522 (F_{2g}^2), 618 (F_{2g}^3) and 691(A_{1g}) cm^{-1}, corresponding to the vibration modes of spinel Co_3O_4 [9, 12]. Raman bands around 691 and 194 cm^{-1} were assigned to the octahedral sites with A_{1g} symmetry and the tetrahedral sites with F_{2g}^1 symmetry of the crystalline Co_3O_4, respectively. Whereas the bands located at 488, 522 and 618 cm^{-1} were attributed to the Eg, F_{2g}^2 and F_{2g}^3 symmetry, respectively [3]. Similar Raman bands were observed for the Nb-doped Co_3O_4 catalysts. While the bands became broader and the intensities were distinctly weakened, which could be correlated with the lattice distortion of the spinel structure caused by the doping of Nb that weakens the Co–O bonds [4]. Among the prepared samples, the weakest and broadest bands were observed for 1.5% Nb-Co_3O_4 and such finding is consistent with its lowest crystallinity and smallest crystallite size. In addition, the presence of Nb shifted the Raman bands to lower frequencies, which would result in highly defective structures of the Nb-doped Co_3O_4 catalysts [13].

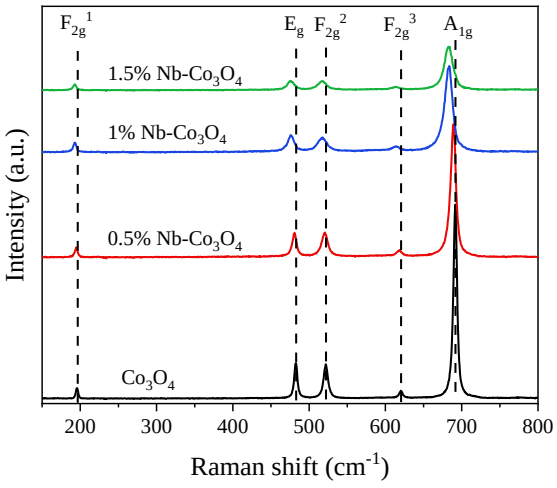

Fig. 5.9 Raman spectra of the synthesized x%Nb-Co_3O_4 catalysts.

5.5.4 FT-IR

The chemical structure of the synthesized catalysts was further investigated by FT-IR analysis (Fig. 4.15). For the pure Co_3O_4 and Nb-doped Co_3O_4 catalysts, the spectra displayed two sharp infrared adsorption bands at 654 and 539 cm^{-1}, which were assigned to the stretching vibrations of the metal-oxygen bond. The band at 654 cm^{-1} was attributed to the vibration mode of Co^{2+}-O from tetrahedral sites, whereas the band at 539 cm^{-1} was associated with the vibration mode of Co^{3+}-O from octahedral sites [14], which is consistent with the formation of spinel Co_3O_4 during the synthesis.

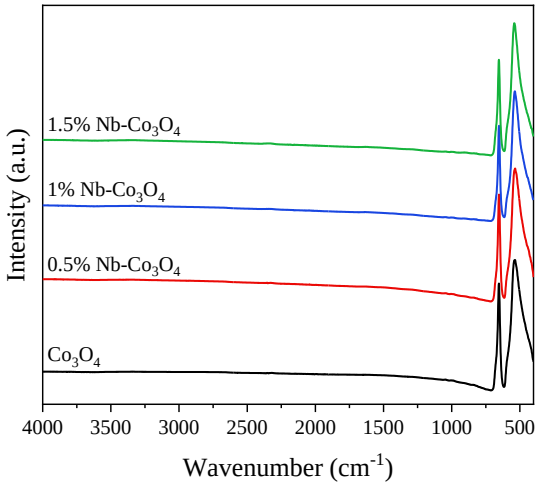

Fig. 5.10 FT-IR spectra of the synthesized x%Nb-Co_3O_4 catalysts.

5.5.5 H_2-TPR

H_2-TPR experiments were carried out to investigate the effect of Nb doping on the reduction behavior of the synthesized catalysts. The H_2-TPR profiles are shown in Fig. 5.11. NbO_2 was not reducible in our experimental conditions. For the Co_3O_4-based catalysts, the reduction processes started from ~200 °C and finished before 450 °C. The H_2-TPR curves of the Co_3O_4 and x%Nb-Co_3O_4 catalysts showed two reduction peaks. The first reduction peak is before 350 °C (peak I), corresponding to the reduction of Co_3O_4 to CoO. Another reduction peak (peak II) occurs around 400 °C, attributed to the reduction of CoO to metal Co [14]. By observing the TPR curves, it was found that the low temperature reducibility of the catalysts was in the order of 1%Nb-Co_3O_4 > 1.5%Nb-Co_3O_4 > 0.5%Nb-Co_3O_4 > Co_3O_4. When Co_3O_4 was doped with Nb, the first reduction peak shifted to the low temperature direction, indicating that the first reduction of Co_3O_4 was promoted. The lowest reduction temperature appeared on the 1%Nb-Co_3O_4 catalyst. The low temperature reducibility of the catalyst decreased slightly when Nb doping amount exceeds 1%. The distortion of Co_3O_4 lattice caused by the doping of Nb could affect the crystalline symmetry, resulting in the formation of weaker Co–O bond than that of pure Co_3O_4, which was traced to the origin of the high reducibility of the Nb-doped Co_3O_4 catalysts [4].

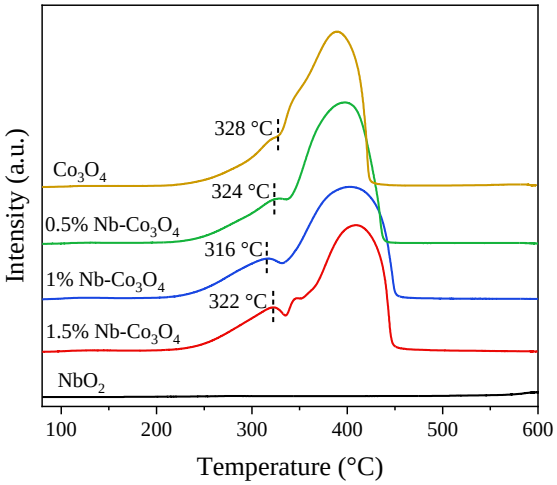

Fig. 5.11 H_2-TPR profiles of the synthesized x%Nb-Co_3O_4 catalysts.

The quantitative evaluation of hydrogen consumption is shown in Table 5.3. The actual H_2 consumption was lower than the expected value for each sample. The presence of oxygen vacancies and more Co^{2+} than the theoretical value should be the reasons for this phenomenon. In view of the different radius of Co^{2+} (0.078 nm), Co^{3+} (0.065 nm) and Nb^{4+} (0.068 nm), Nb4+ would mainly replace Co^{3+} during the doping process, leading to the decrease of Co^{3+} content. On the other hand, to keep the charge balance, the amount of Co^{2+} would increase, resulting in the further lowering of the H_2 consumption. From the ratio of actual H_2 consumption to theoretical H_2 consumption, it was inferred that there were more Co^{3+} displaced by Nb^{4+} for 1% Nb-Co_3O_4, which was in accordance with the XRD analysis. The area ratios of peak I to peak II could be regarded as a reference for the relative contents of Co^{3+} and Co^{2+}. Therefore, they were calculated and summarized in Table 5.3. The values of the Nb-doped Co_3O_4 catalysts were lower than that of pure Co_3O_4, and 1% Nb-Co_3O_4 showed the lowest ratio of Co^{3+}/Co^{2+}.

Table 5.3 H_2-TPR data of the synthesized x%Nb-Co_3O_4 catalysts.

Catalyst	Theoretical H_2 consumption (mmol g^{-1})	Actual H_2 consumption (mmol g^{-1})	Actual H_2 consumption/ Theoretical H_2 consumption	Reduction temperature of Co^{3+} to Co^{2+} (°C)	A_{peakI}/A_{peakII}
Co_3O_4	16.61	15.85	0.954	328	0.32
0.5%Nb-Co_3O_4	16.53	15.70	0.950	324	0.28
1%Nb-Co_3O_4	16.44	15.26	0.928	316	0.25
1.5%Nb-Co_3O_4	16.36	15.23	0.931	322	0.27

5.5.6 NH_3-TPD

The surface acidity of the catalyst is of great significance to the oxidation of CVOCs. We tested the surface acidity of the synthesized catalysts through NH_3-TPD experiments, and the results are shown in Figure 5.12. The total amount of acidity of the catalysts was calculated according to the desorption peak area of the catalysts. The calculated results are listed in Table

5.4. The desorption peak near 200 and 325 °C was attributed to the weak and medium acidity sites on the catalyst surface, respectively. While the desorption peak around 450 °C was corresponding to the strong acidity sites on the catalyst surface. Pure Co_3O_4 showed weak surface acidity, whereas NbO_2 showed the strongest surface acidity. The doping of Nb can significantly enhance the weak acidity sites Co_3O_4. In particular, the medium and strong acidity sites of 1% Nb-Co_3O_4 and 1.5% Nb-Co_3O_4 were obviously strengthened, which may be one of the reasons for the improvement of the catalytic activity for VC oxidation.

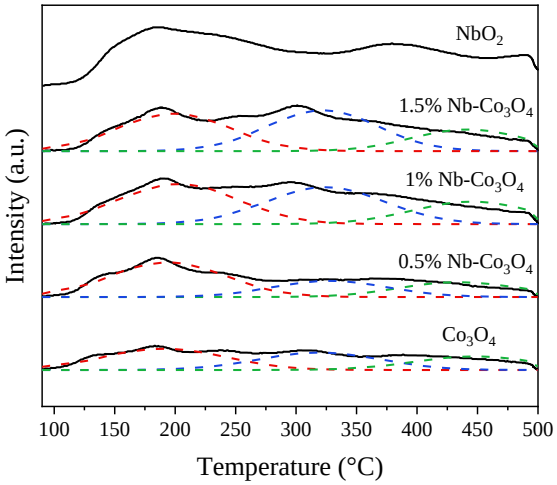

Fig. 5.12 NH_3-TPD profiles of the synthesized x%Nb-Co_3O_4 catalysts.

5.5.7 XPS

XPS analysis was carried out to investigate the surface chemical composition and valence distribution of the x%Nb-Co_3O_4 catalysts. Fig. 5.13 shows the Co 2p and O 1s spectra of the pure Co_3O_4 and x% Nb-Co_3O_4 catalysts. The Co 2p spectra of the catalysts displayed two main peaks at ~795.1 and 779.9 eV, corresponding to the Co 2p1/2 and Co 2p3/2 spin-orbital peaks of Co_3O_4 spinel [8, 15]. The spin-orbit splitting energy of these two peaks was around 15.2 eV, agreeing well with those reported in the literature [8, 13]. By deconvolution of the Co 2p spectra, the Co 2p3/2 signal was decomposed into two components. One peak at B.E. of ~779.8 eV was attributed to the surface Co^{3+} species, while the other at B.E. of ~781.4 eV was assigned to the surface Co^{2+} species. The superficial Co^{2+}/Co^{3+} molar ratios calculated from the peak area percentages are listed in Table 5.4. Higher surface Co^{2+} concentrations were found for the Nb-doped Co_3O_4 catalysts as compared with that for pure Co_3O_4, indicating the presence of more surface oxygen vacancies [13, 15], which may be caused by the substitution of Co^{3+} by Nb^{4+} as discussed above. The highest surface Co^{2+} concentration was observed for 1% Nb-Co_3O_4, which was consistent with the maximum Nb^{4+} entering into the spinel lattice and had important for propane and VC oxidation [15].

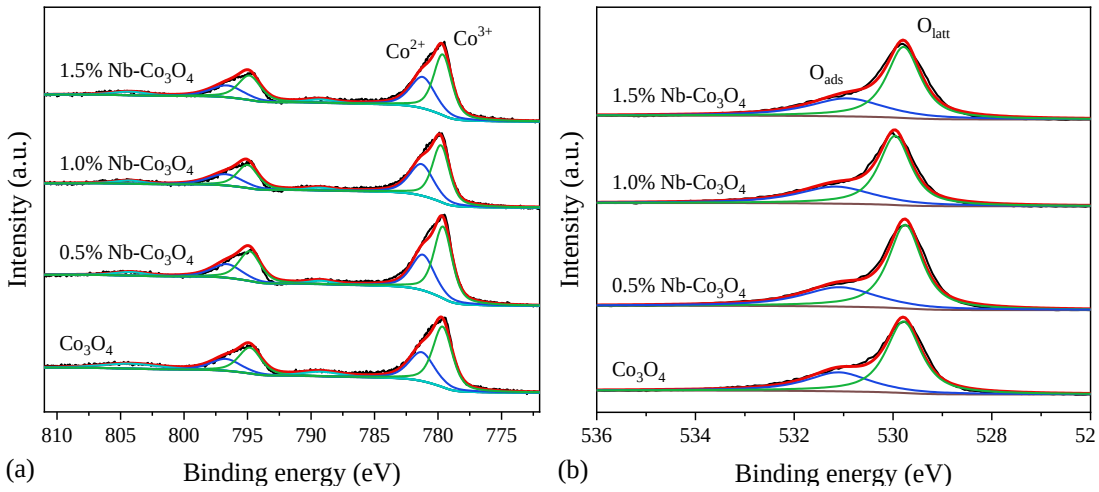

Fig. 5.13 XPS spectra of (a) Co 2p and (b) O 1s for the synthesized x%Nb-Co_3O_4 catalysts.

The O 1s spectra were found to be broad for all the samples, indicating the existence of several kinds of surface oxygen species. Hence, the asymmetrical O 1s peaks were decomposed into two components (Fig. 5.13b). The former was correlated with the surface lattice species (O_{latt}), whereas the latter corresponded to the surface adsorbed oxygen species (O_{ads}) [12]. As seen from Table 5.4, the O_{ads}/O_{latt} ratios of the Nb-doped catalysts were higher than that of pure Co_3O_4. 1% Nb-Co_3O_4 exhibited the highest O_{ads}/O_{latt} ratio, indicating that there were more active oxygen species in 1% Nb-Co_3O_4 that can participate in oxidation reaction at low temperature [15, 16].

Table 5.4 NH_3-TPD and XPS data of the synthesized x%Nb-Co_3O_4 catalysts.

Catalyst	Acidity (mmol NH_3 g^{-1})				Co^{2+}/Co^{3+}	O_{ads}/O_{latt}
	Total	Weak	Medium	Strong		
Co_3O_4	0.037	0.015	0.012	0.010	0.62	0.48
0.5%Nb-Co_3O_4	0.046	0.024	0.011	0.011	0.63	0.51
1%Nb-Co_3O_4	0.069	0.028	0.026	0.015	0.78	0.58
1.5%Nb-Co_3O_4	0.064	0.024	0.026	0.014	0.70	0.56
NbO_2	0.076	/	/	/	/	/

5.5.8 Propane oxidation without oxygen

Propane oxidation tests without oxygen were carried out to investigate the content of active oxygen species and the mobility of lattice oxygen in the catalysts. Before the tests, the catalysts were pretreated at 300 °C for 1 h with He to remove weakly adsorbed surface species. The evolution of CO_2 concentration and temperature versus time were shown in Fig. 5.14. One can see that even in the absence of oxygen, some propane could be oxidized into CO_2 between 100 and 350 °C during the heating ramp over the catalysts. However, in the cooling stage, no CO_2 was produced in this temperature range. This phenomenon can be explained by the complete depletion of chemisorbed oxygen. On the other hand, continuous production of CO_2 was

observed for 1 h at 350 °C, indicating that surface lattice oxygen in the catalysts can migrate and participate in propane oxidation. The amount of CO_2 production reflected the content of active oxygen species and oxygen mobility of the catalysts. Pure Co_3O_4 clearly showed the minimum active oxygen content and the weakest oxygen mobility. The content of active oxygen species and oxygen mobility of x% Nb-Co_3O_4 catalysts were significantly enhanced due to the incorporation of Nb. Among all the catalysts, 1% Nb-Co_3O_4 exhibited the largest amount of active oxygen species and the highest oxygen mobility.

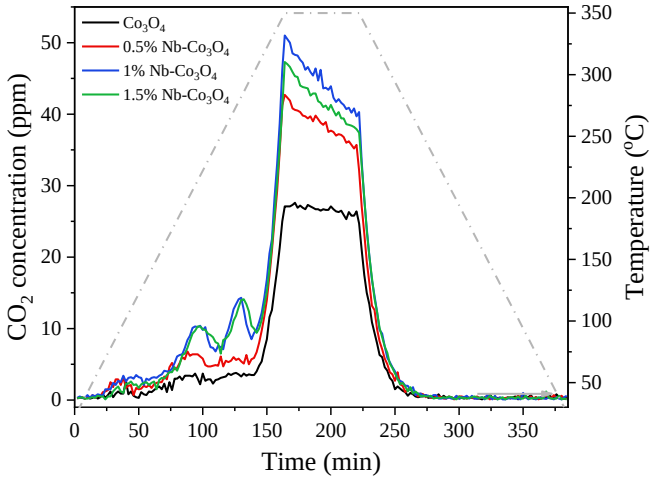

Fig. 5.14 CO_2 concentrations in propane oxidation without oxygen over the synthesized x%Nb-Co_3O_4 catalysts.

5.6 Discussions

The doping of Nb (< 2%) in Co_3O_4 can significantly influence its physicochemical properties, and then affect its catalytic performance for the oxidation of propane and VC. The interaction of dopant Nb and Co_3O_4 enhanced the crystallite size, specific surface area, reducibility, surface acidity, surface Co^{2+}/Co^{3+} molar ratio, surface adsorbed oxygen species content and oxygen mobility of the x% Nb-Co_3O_4 catalysts, thus improving its catalytic activity. 1%Nb-Co_3O_4 with the highest amount of Nb doping has the highest catalytic activity, with T_{90} of 239 ℃ for propane oxidation (WHSV of 40000 mL g^{-1} h^{-1}) and 288 ℃ for VC oxidation (WHSV of 30000 mL g^{-1} h^{-1}). Table 5.5 lists the activity data of the catalysts for CVOCs oxidation reported in the literature and compares them with the catalysts in this paper. It can be seen that noble metal catalysts usually show high catalytic activity for CVOCs oxidation. Specifically, the Ru-based catalysts have excellent catalytic performance. Different transition metal oxides also show relatively good catalytic activity for the catalytic oxidation of CVOCs. Among them, the Co_3O_4 catalysts can exhibit high activity for the catalytic oxidation of various CVOCs. This is consistent with its good catalytic activity in the low temperature catalytic

oxidation of VOCs [15], CO [15, 25] and diesel engine soot [26]. In the catalytic oxidation of DCE, the catalytic activity of Co_3O_4 is even higher than that of noble metal catalysts.

Table 5.5 Comparison of catalytic activities of the catalysts in this thesis with those in the references for CVOCs oxidation.

Catalyst	Reaction condition	Catalytic activity		Reference
		T_{50} (°C)	T_{90} (°C)	
Pt/TiO_2	0.5 g catalyst 1000 ppm CH_2Cl_2	> 320	/	[17]
Ru/TiO_2	30000 h^{-1}	~ 260	~ 307	
Cr_2O_3	1 g catalyst 3000 ppm CH_2Cl_2	292	~ 379	[18]
$CoCr_2O_4$-6	15000 h^{-1}	210	~ 291	
H-ZSM-5	0.85 g catalyst 1000 ppm TCE	~ 520	~ 625	[19]
Fe-ZSM-5, IE	13500 h^{-1}	~ 400	~ 461	
CeO_2	0.85 g catalyst 1000 ppm DCE 30000 h^{-1}	345	~ 425	[20]
$Pt(0.44wt.\%)/Al_2O_3$	0.85 g catalyst 1000 ppm DCE	~ 321	~ 355	[21]
$Pd(0.42wt.\%)/Al_2O_3$	15000 h^{-1}	~ 311	~338	
Co_3O_4 (CC-500)	0.85 g catalyst 1000 ppm DCE 15000 h^{-1}	250	300	[22]
MnO_x	0.20 g catalyst 1000 ppm VC	~ 333	~ 379	[23]
$Mn_{0.4}Ti_{0.6}O_x$	30000 mL g^{-1} h^{-1}	~ 201	~ 267	
Co_3O_4	0.6 g catalyst 1000 ppm VC	253	295	[24]
1%Ru/Co_3O_4	15000 h^{-1}	186	216	
$Co_{95}Zr_5$	0.2 g catalyst 1000 ppm VC 30000 mL g^{-1} h^{-1}	261	294	Chapter 4 in this thesis
1% Zr-Co_3O_4	0.2 g catalyst 1000 ppm VC 30000 mL g^{-1} h^{-1}	273	303	Chapter 5 in this thesis

Figure 5.15 shows the relationship between the catalytic performance and several physicochemical properties of the x% Nb-Co_3O_4 catalysts for propane and VC oxidation. It can be seen that T_{90} on 1%Nb-Co_3O_4 is the lowest, and the reaction rate is also the highest. XRD and N_2-sorption results showed that with the addition of Nb, the crystallite size of Co_3O_4 decreased significantly and the SSA increased. 1.5% Nb-Co_3O_4 had the smallest crystallite size, which may be due to inhibition the growth of Co_3O_4 particles caused by the high dispersion of Nb species on its surface. Combined with the results of the catalytic activity of the catalysts, it can be found that the crystallite size and SSA of the catalysts may not be the key factors in propane and VC oxidation in this work. On the contrary, the shift of reduction peak to low temperature in H_2-TPR experiments confirmed that the low temperature reducibility of the x% Nb-Co_3O_4 catalysts was significantly improved by Nb doping. And the change of A_{peakI}/A_{peakII} indicated that Co^{3+} decreased in the x% Nb-Co_3O_4 catalysts. Raman spectra revealed the lattice distortion and defective structures of the x% Nb-Co_3O_4 catalysts, which may be associated with the abundant oxygen vacancies. NH_3-TPD results showed that Nb doping can enhance the surface acidity of the catalysts. XPS characterization showed that Nb doping produced more surface oxygen vacancies and adsorbed oxygen species, as well as better oxygen mobility, which was conducive to the generation of active oxygen species. Therefore, the x% Nb-Co_3O_4 catalysts exhibited better catalytic activity for propane and VC oxidation than pure Co_3O_4. Among all the catalysts, 1% Nb-Co_3O_4 exhibited the highest catalytic activity, which mainly benefited from the better reducibility, more surface acidity and higher content of active oxygen species.

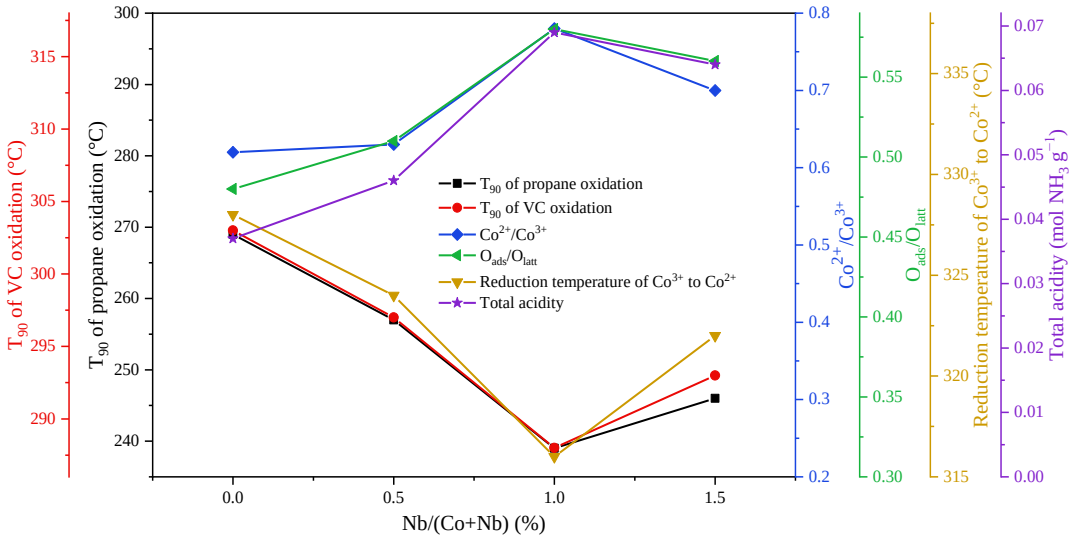

Fig. 5.15 The relationship between the catalytic performance of propane oxidation and several physical and chemical parameters of the x%Nb-Co_3O_4 catalysts.

5.7 Conclusions

A series of Nb-doped Co_3O_4 catalysts were prepared by the sol-gel method, and the activity and stability of the catalysts for the catalytic oxidation of propane and VC were investigated respectively. The physicochemical properties of the catalysts were characterized by XRD, Raman, FT-IR, N_2-sorption, H_2-TPR, NH_3-TPD, XPS and propane oxidation without oxygen experiments. The catalytic performance and structural properties of the catalysts were effectively correlated. The main conclusions are as follows:

1. There is a maximum amount of Nb that can be doped into the lattice of Co_3O_4. When the doping amount continues to increase, it tends to form NbO_x, and the actual doping amount of Nb would decrease. Nb doping improves the catalytic activity of the Co_3O_4 catalyst for propane and VC oxidation. When the doping amount of Nb is the largest, the catalytic activity of the catalyst is the best (1%Nb-Co_3O_4), with T_{90} of 239 ℃ and 288 ℃ for propane and VC oxidation, respectively.

2. The moderate doping of Nb in Co_3O_4 can lead to smaller crystallite size, larger specific surface area, more defect structures, better reducibility, stronger surface acidity, higher content of surface Co^{2+} and active oxygen species, and better oxygen mobility of Co_3O_4, resulting in the promotion of the catalytic performance of the Co_3O_4 catalyst for propane and VC oxidation.

3. For the catalytic oxidation of VC, the improvement of the surface acidity caused by Nb doping enhanced the resistance of the catalyst to chlorine poisoning and inhibited the generation of polychlorinated by-products to a certain extent. When a certain amount of water was added into the feed gas, the catalytic activity of 1%Nb-Co_3O_4 catalyst would not be decreased, and the formation of chlorine gas was inhibited.

4. The most active catalyst for propane and VC oxidation (1%Nb-Co_3O_4) can maintain high stability in the stability tests.

References

[1] P. Yang, S. Zuo, Z. Shi, F. Tao, R. Zhou. Elimination of 1,2-dichloroethane over $(Ce,Cr)_xO_2/MO_y$ catalysts (M = Ti, V, Nb, Mo, W and La). Applied Catalysis B: Environmental. 2016, 191: 53-61.

[2] P. Yang, S. Fan, Z. Chen, G. Bao, S. Zuo, C. Qi. Synthesis of Nb_2O_5 based solid superacid materials for catalytic combustion of chlorinated VOCs. Applied Catalysis B: Environmental. 2018, 239: 114-124.

[3] A. Alvarez, S. Ivanova, M.A. Centeno, J.A. Odriozola. Sub-ambient CO oxidation over mesoporous Co_3O_4: effect of morphology on its reduction behavior and catalytic performance. Applied Catalysis A, General. 2012, 431-432: 9-17.

[4] W. Deng, Q. Dai, Y. Lao, B. Shi, X. Wang. Low temperature catalytic combustion of 1,2-dichlorobenzene over CeO_2-TiO_2 mixed oxide catalysts. Applied Catalysis B: Environmental. 2016, 181: 848-861.

[5] H. Zhao, W. Han, F. Dong, Z. Tang. Highly-efficient catalytic combustion performance of 1,2-dichlobenzene over mesoporous TiO_2-SiO_2 supported CeMn oxides: the effect of acid sites and redox sites. Journal of Industrial and Engineering Chemistry. 2018, 64: 194-205

[6] H. Wu, G. Pantaleo, G. Di Carlo, S. Guo, G. Marci, P. Concepción, A.M. Venezia, L.F. Liotta. Co_3O_4 particles grown over nanocrystalline CeO_2: influence of precipitation agents and calcination temperature on the catalytic activity for methane oxidation. Catalysis Science & Technology. 2015, 5: 1888-1901.

[7] W. Sun, J. Sun, L. Du, C. Du, Y. Gao, G. Yin. Synthesis of nitrogen-doped niobium dioxide and its co-catalytic effect towards the electrocatalysis of oxygen reduction on platinum. Electrochimica Acta. 2016, 195: 166-174.

[8] T. Cai, H. Huang, W. Deng, Q. Dai, W. Liu, X. Wang. Catalytic combustion of 1,2-dichlorobenzene at low temperature over Mn-modified Co_3O_4 catalysts. Applied Catalysis B: Environmental. 2018, 166-167: 393-405.

[9] Z. Pu, Y. Liu, H. Zhou, W. Huang, Y. Zheng, X. Li. Catalytic combustion of lean methane at low temperature over ZrO_2-modified Co_3O_4 catalysts. Applied Surface Science. 2017, 422: 85-93.

[10] J. Li, X. Xu, Z. Hao, W. Zhao. Mesoporous silica supported cobalt oxide catalysts for catalytic removal of benzene. Journal of Porous Materials. 2008, 15: 163-169.

[11] Z. Sihaib, F. Puleo, J.M. Garcia-Vargas, L. Retailleau, C. Descorme, L.F. Liotta, J.L. Valverde, S. Gil, A. Giroir-Fendler. Manganese oxide-based catalysts for toluene oxidation. Applied Catalysis B: Environmental. 2017, 209: 689-700.

[12] L. Li, W. Wang. Synthesis and characterization of monoclinic ZrO_2 nanorods by a novel and simple precursor thermal decomposition approach. Solid State Communications. 2003, 127: 639-643.

[13] J. González-Prior, R. López-Fonseca, J.I. Gutiérrez-Ortiz, B. de Rivas. Oxidation of 1,2-dichloroethane over nanocube-shaped Co_3O_4 catalysts. Applied Catalysis B: Environmental. 2016, 199: 384-393.

[14] Z. Zhu, G. Lu, Z. Zhang, Y. Guo, Y. Guo, Y. Wang. Highly active and stable Co_3O_4/ZSM-5 catalyst for propane oxidation: Effect of the preparation method. ACS Catalysis. 2013, 3: 1154-1164.

[15] W. Zhang, F. Wu, J. Li, Z. You. Dispersion-precipitation synthesis of highly active nanosized Co_3O_4 for catalytic oxidation of carbon monoxide and propane. Applied Surface Science. 2017, 411: 136-143.

[16] B. Puértolas, A. Smith, I. Vázquez, A. Dejoz, A. Moragues, T. Garcia, B. Solsona. The different catalytic behaviour in the propane total oxidation of cobalt and manganese oxides prepared by a wet combustion procedure. Chemical Engineering Journal. 2013, 229: 547-558.

[17] S. Cao, X. Fei, Y. Wen, Z. Sun, H. Wang, Z. Wu. Bimodal mesoporous TiO_2 supported Pt, Pd and Ru catalysts and their catalytic performance and deactivation mechanism for catalytic combustion of Dichloromethane (CH_2Cl_2). Applied Catalysis A: General. 2018, 550: 20-27.

[18] J.-D. Liu, T.-T. Zhang, A.-P. Jia, M.-F. Luo, J.-Q. Lu. The effect of microstructural properties of $CoCr_2O_4$ spinel oxides on catalytic combustion of dichloromethane. Applied Surface Science. 2016, 369: 58-66.

[19] M. Romero-Sáez, D. Divakar, A. Aranzabal, J.R. González-Velasco, J.A. González-Marcos. Catalytic oxidation of trichloroethylene over Fe-ZSM-5: Influence of the preparation method on the iron species and the catalytic behavior. Applied Catalysis B: Environmental. 2016, 180: 210-218.

[20] J.I. Gutiérrez-Ortiz, B. de Rivas, R. López-Fonseca, J.R. González-Velasco. Combustion of aliphatic C_2 chlorohydrocarbons over ceria–zirconia mixed oxides catalysts. Applied Catalysis A: General. 2004, 269: 147-155.

[21] J.R. González-Velasco, A. Aranzabal, J.I. Gutiérrez-Ortiz, R. López-Fonseca, M.A. Gutiérrez-Ortiz. Activity and product distribution of alumina supported platinum and palladium catalysts in the gas-phase oxidative decomposition of chlorinated hydrocarbons. Applied Catalysis B: Environmental. 1998, 19: 189-197.

[22] B. de Rivas, R. López-Fonseca, C. Jiménez-González, J.I. Gutiérrez-Ortiz. Synthesis, characterization and catalytic performance of nanocrystalline Co_3O_4 for gas-phase chlorinated VOC abatement. Journal of Catalysis, 2011, 281: 88-97.

[23] H. Liu, X. Li, Q. Dai, H. Zhao, G. Chai, Y. Guo, Y. Guo, L. Wang, W. Zhan. Catalytic oxidation of chlorinated volatile organic compounds over Mn-Ti composite oxides catalysts: Elucidating the influence of surface acidity. Applied Catalysis B: Environmental. 2021, 282: 119577.

[24] C. Wang, C. Zhang, W. Hua, Y. Guo, G. Lu, S. Gil, A. Giroir-Fendler. Low-temperature catalytic oxidation of vinyl chloride over Ru modified Co_3O_4 catalysts. RSC Advances. 2016, 6: 99577-99585.

[25] Y. Lou, L. Wang, Z. Zhao, Y. Zhang, Z. Zhang, G. Lu, Y. Guo, Y. Guo. Low-temperature CO oxidation over Co_3O_4-based catalysts: Significant promoting effect of Bi_2O_3 on Co_3O_4 catalyst. Applied Catalysis B: Environmental. 2014, 146: 43-49.

[26] Z. Shang, M.Sun, S. Chang, X. Che, X. Cao, L. Wang, Y. Guo, W. Zhan, Y. Guo, G. Lu. Activity and stability of Co_3O_4-based catalysts for soot oxidation: The enhanced effect of Bi_2O_3 on activation and transfer of oxygen. Applied Catalysis B: Environmental. 2017, 209: 33-44.

Chapter 6 The influence of residual sodium on the catalytic performance of Co_3O_4 catalysts

6.1 Introduction

Synthesis process is of great importance to Co_3O_4 catalysts since it could determine the physicochemical properties, such as the crystallite size, morphology, and reducibility of Co_3O_4 catalysts, and then affect their catalytic activity [1-4]. The synthesized catalysts in Chapter 4 and 5 showed relatively high catalytic activity for propane and VC oxidation. However, for the preparation method of sol-gel, the colloid would greatly dilate to form spongiform catalyst precursor in the drying process. Thus, there is certain limitation for its practical application due to the selection and use of the container. Precipitation is one of the most widely used methods to prepare Co_3O_4 and other metal oxides catalysts in heterogeneous catalysis, which requires simple set-up, short time and can be easily scaled for practical industrial applications [5-8].

In this chapter, the Co_3O_4 catalysts with different contents of residual sodium were prepared by the precipitation method and applied in the catalytic oxidation of propane. Their activity and stability were evaluated. Finally, the physicochemical properties of the catalysts were investigated by a series of characterization methods, and the structure-performance relationship of the catalysts was studied.

6.2 Preparation of catalysts

A series of Co_3O_4 catalysts were prepared via precipitation using sodium carbonate as the precipitant. Typically, 20 mmol cobalt nitrate hexahydrate ($Co(NO_3)_2 \cdot 6H_2O$) and 22 mmol sodium carbonate (Na_2CO_3) were dissolved in 100 mL water, respectively. Then the solution of precipitant was added into the solution of $Co(NO_3)_2 \cdot 6H_2O$ under continuous stirring and the mixed solution was kept stirring for 1 h at room temperature. After centrifugation, the precipitates were washed with deionized water for 1, 2, 3 and 5 times (200 mL each time) in order to obtain samples with various contents of residual sodium. The pH of the liquor would be close to neutral after 3 times of washing. All the precipitates were dried in an oven at 80 °C overnight. After that, the dried powders were calcined under static air in a muffle furnace at 200 °C for 2 h, and then, 500 °C for 2 h, respectively. The obtained Co_3O_4 catalysts were denoted as Co-CO_3-xT, where x represents the numbers of washing.

6.3 Evaluation of catalysts

The catalyst evaluation method is described in Chapter 2, Section 2.5.2.

6.4 Characterization of catalysts

6.4.1 ICE-OES

The residual sodium content present in the catalysts was measured by ICP-OES. The results are shown in Table 6.1. This value was extremely high (2.4 wt.%) in Co-CO_3-1T, whereas it significantly decreased to 0.33 wt.% after washing the catalyst precursor twice, and further dropped to 0.14 wt.% with one more washing in Co-CO_3-3T. In this sense, Co-CO_3-5T, washed five times, was prepared in order to obtain a catalyst free of sodium in its structure.

Table 6.1 Physicochemical properties of the synthesized Co-Co_3-xT catalysts.

Catalyst	Na (wt.%)	d (nm)	a (Å)	SSA ($m^2\ g^{-1}$)	Average pore size (nm)	V_{pore} ($cm^3\ g^{-1}$)
Co-CO_3-1T	2.4	19.8	8.0914	28	13	0.085
Co-CO_3-2T	0.3	30.8	8.0882	27	12	0.081
Co-CO_3-3T	0.1	31.3	8.0882	25	10	0.064
Co-CO_3-5T	<0.1	33.0	8.0881	22	9	0.049

6.4.2 XRD

Fig. 6.1 displays the wide-angle XRD patterns of the catalysts with different residual sodium content. Diffraction peaks at 2θ = 18.9, 31.2, 36.6, 44.9, 59.4 and 69.1° were observed and attributed to a cubic phase of spinel Co_3O_4 (PDF # 74-2120) [9, 10]. These peaks could be ascribed to the (111), (220), (311), (400), (511) and (440) planes of Co_3O_4. No phase associated with sodium species were observed on all the samples, possibly due to the well dispersion and low contents of sodium. However, the diffraction peaks became sharp and intense as the number of washing steps increased, suggesting the growth of crystallite size, which was confirmed by the results calculated from the most intense (311) diffraction peak by the Scherrer equation (Table 6.1). Moreover, it could be seen that the (311) diffraction peak in the XRD pattern of Co-CO_3-1T appeared at a lower diffraction angle compared with that of other samples, as shown in Fig. 6.1b, indicating that sodium may be introduced into the spinel lattice of Co_3O_4, inducing the structure distortion and inhibiting the crystallization of Co_3O_4 [9]. Taking as a reference the above mentioned six diffraction peaks, the lattice constant of each sample was also estimated. This way, it was observed that the value of the lattice constant in Co-Co_3-2T, Co-Co_3-3T and Co-Co_3-5T were identical while that of Co-Co_3-1T was larger, which could be again associated with the presence of sodium into the Co_3O_4 lattice.

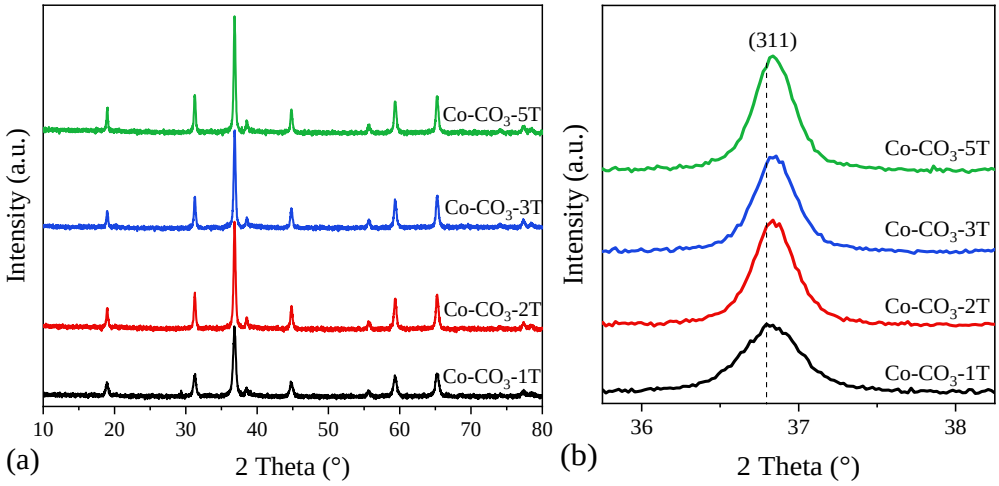

Fig. 6.1 (a) XRD patterns of the synthesized Co-CO_3-xT catalysts; (b) detail of the most intense diffraction peak of (311) crystal facet.

6.4.3 Raman

Raman spectra allows to get information about the lattice distortion of the catalysts (Fig. 6.2). Five bands at 191, 474, 514, 609 and 679 cm^{-1} were observed, corresponding to the stretching modes of the spinel Co_3O_4 [5]. The bands at 474 and 679 cm^{-1} were attributed to the E_g and A_{1g} modes, respectively, whereas the bands at 191, 514 and 609 cm^{-1} could be assigned to the F_{2g} modes. A_{1g} mode was associated with the octahedral sites whereas the F_{2g} and E_g modes corresponded to the vibration of tetrahedral and octahedral sites [11]. It was found that the Raman bands of Co-CO_3-1T shifted to lower frequencies compared with those of other catalysts, which was due to the lattice expansion and lattice distortion caused by the introduction of sodium. This result agrees well with the XRD analysis. Moreover, the red shift was also observed in Co-CO_3-2T, which suggests the defective structure of the catalyst.

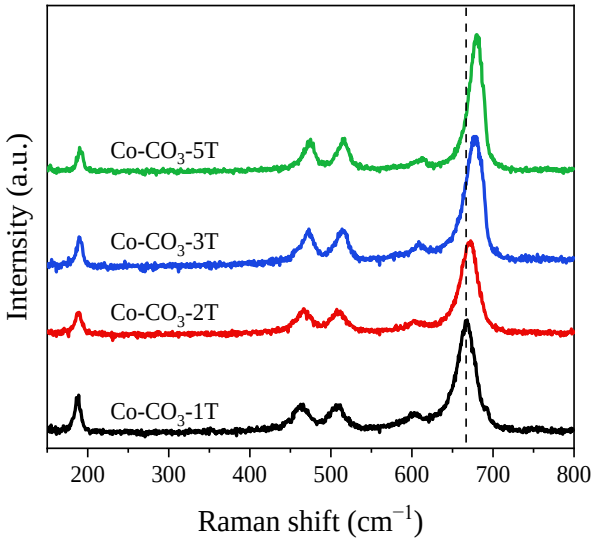

Fig. 6.2 Raman spectra of the synthesized Co-CO_3-xT catalysts.

6.4.4 FT-IR

The FT-IR adsorption spectra of the catalysts are shown in Fig. 6.3. Bands corresponding to the catalysts mainly occurred at 656 and 546 cm^{-1}, which was associated with the stretching vibration of Co-O in the Co_3O_4 spinel lattice. The former one could be assigned to the stretching vibration mode of Co^{2+}-O from the tetrahedral sites, whereas the latter one was attributed to the stretching vibration of Co^{3+}-O in the octahedral coordination [12]. One can see in Fig. 6.3b that the stretching vibration bands of octahedrally coordinated Co^{3+} and tetrahedrally coordinated Co^{2+} shifted to lower wavenumbers when the number of washing steps of the precursor was more than one, which would indicate the decrease in the strength of the Co-O bond [13]. In addition, some additional infrared adsorption bands at 836 and 1356 cm^{-1} were clearly observed in Co-CO_3-1T in Fig. 6.3c, which could be assigned to the stretching vibration of the undecomposed nitrate groups [14].

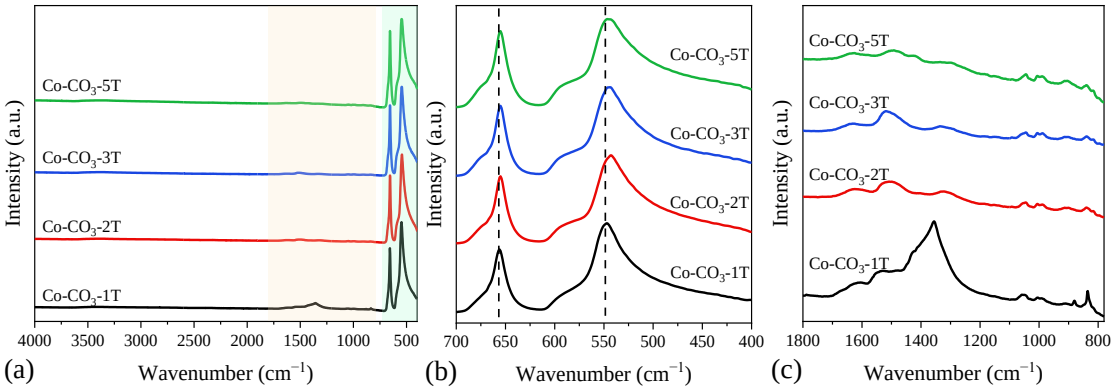

Fig. 6.3 (a) Full and (b, c) partial FT-IR spectra of the synthesized Co-CO_3-xT catalysts.

6.4.5 N_2-sorption

Fig. 6.4 shows the N_2-sorption isotherms and pore size distribution curves of the catalysts. All catalysts exhibited type IV isotherms with H3 hysteresis loops according to the IUPAC classification, being mesoporous in structure. The SSA, V_{pore} and average pore sizes of the catalysts are a function of the content of residual sodium. Co-CO_3-1T showed the largest SSA and V_{pore}, as well as the average pore size, which could be ascribed to the enhancement of textural properties caused by the distortion in the spinel lattice of Co_3O_4. The lower the residual sodium, the lower the values of SSA and V_{pore} both were observed, suggesting that the Co_3O_4 particles could easily sinter during the thermal treatment with less residual sodium. Regarding the pore size distribution of the catalysts, it was found that all samples exhibited a similar pore size of ca. 2.5 nm. However, Co-CO_3-1T had a broader pore size distribution than other samples, which might be attributed to the presence of accumulated holes between particles by nano-Co_3O_4 crystallite bridges [13], which could in turn contribute to the increase of the pore volume.

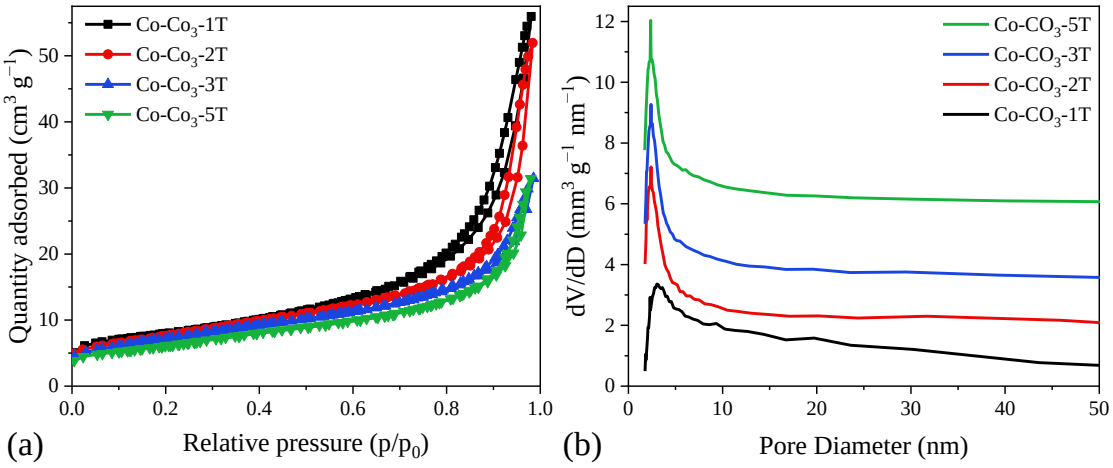

Fig. 6.4 (a) N_2 sorption isotherms and (b) pore size distribution curves of the synthesized Co-CO_3-xT catalysts.

6.4.6 CO-TPR

CO-TPR experiment allows to evaluate the reducibility of a catalyst. The evolution of CO_2 concentration at the device outlet during the reduction tests are shown in Fig. 6.5a and that of CO consumption are displayed in Fig. 6.5b. The consumption of CO matches perfectly with the formation of CO_2, indicating that all the consumed CO molecules were oxidized into CO_2 by depletion of oxygen species in the catalysts. The reduction process started for all samples from around 200 °C and was completed below 600 °C with two main reduction peaks observed. The former one in the range of 200 to 350 °C was associated with the reduction of Co_3O_4 to CoO, while the latter one detected between 350 and 550 °C was assigned to the reduction of CoO to metallic Co. From the profiles of CO_2 concentration, one could see that Co-CO_3-3T and Co-CO_3-5T were the most reducible ones with the lowest initial reduction temperature, followed by Co-CO_3-2T. Co-CO_3-1T showed the highest initial reduction temperature, which could probably be explained by the negative impact of residual sodium on the reducibility of Co_3O_4. It was reported that the reactivity of surface oxygen species and the mobility of lattice oxygen played a remarkable role in the oxidation performance of a catalyst [15, 16], which would be reflected by the reducibility of the catalysts. Thus, the shift of reduction peak to lower temperature would indicate the presence of more active oxygen species on Co-CO_3-3T and Co-CO_3-5T. It should be pointed out that a small peak of CO_2 production appeared at 235 °C for Co-CO_3-1T, which could be attributed to the reduction of surface NO_3^-, as confirmed by aforementioned FT-IR analysis.

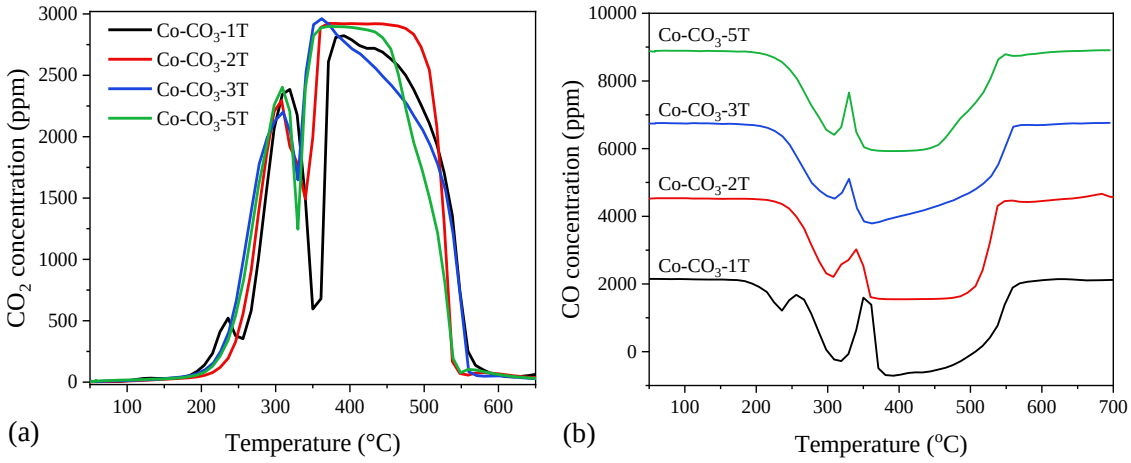

Fig. 6.5 Evolution of (a) CO_2 and (b) CO concentrations during the CO-TPR tests of the synthesized Co-CO_3-xT catalysts.

6.5 Catalytic performance of catalysts

The light-off curves of the third cooling run over the catalysts are plotted in Fig. 6.6a. The T_{50} and T_{90} values in propane oxidation are summarized in Table 6.2. Co-CO_3-3T exhibited the best performance for propane oxidation with T_{50} and T_{90} of 201 and 236 °C, respectively, which could be attributed to its highest reducibility. This catalyst was followed by Co-CO_3-5T, with similar activity in high conversion range but a little worse performance when reaction temperature was lower than 230 °C, probably due to the small SSA compared with Co-CO_3-3T. On the other hand, Co-CO_3-2T with lower reducibility presented lower catalytic performance (T_{90} value was 22 °C higher than that of Co-CO_3-3T). Finally, Co-CO_3-1T showed nearly no catalytic activity in the given temperature, which evidenced the strong inhibiting effect of excess residual sodium [9].

The CO concentrations were in-situ recorded during the whole reaction process, as shown in Fig 6.6b. It was found that CO was not produced with any of the catalysts tested, suggesting the superior oxidation ability of the synthesized Co-CO_3-xT catalysts and the high selectivity of CO_2 in the outlet gases for propane oxidation. The propane oxidation reaction rates were calculated at 175 °C and the results are listed in Table 6.2. Consequently, Co-CO_3-3T exhibited the largest reaction rate (9.9×10^{-8} mol g^{-1} s^{-1}).

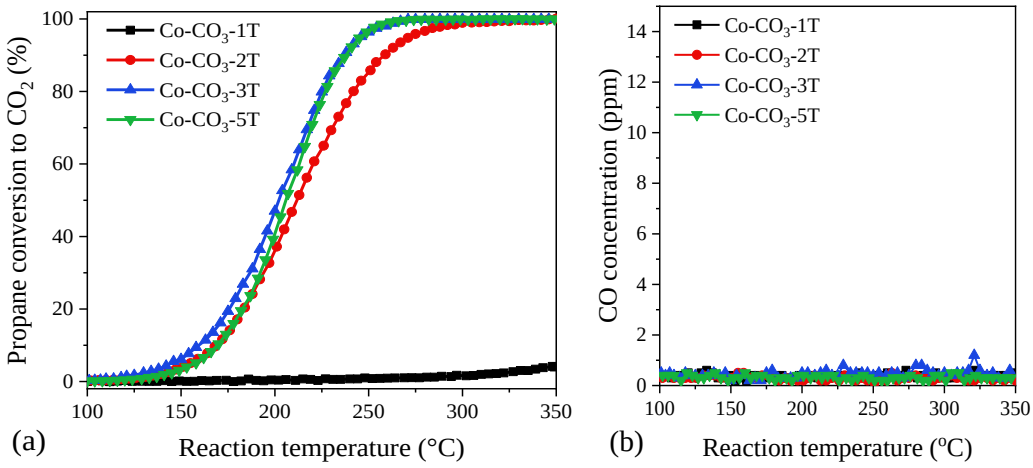

Fig. 6.6 (a) Light-off curves and (b) CO concentrations in the outlet gases of propane oxidation over the synthesized Co-CO_3-xT catalysts. Reaction condition: 1000 ppm propane and synthetic air balance; WHSV = 40000 mL g^{-1} h^{-1}.

Table 6.2 Catalytic performance of the synthesized Co-CO_3-xT catalysts for propane oxidation.

Catalyst	T_{50} (°C)	T_{90} (°C)	r × 10^8 (mol g^{-1} s^{-1})
Co-CO_3-1T	/	/	0.28
Co-CO_3-2T	211	258	6.59
Co-CO_3-3T	201	236	9.85
Co-CO_3-5T	206	238	6.87

Propane oxidation without oxygen was carried out to examine the mobility of the oxygen species in the catalysts. Fig. 6.7 shows the evolution of CO_2 concentration at the reactor exit during the tests. One could see that propane could be oxidized into CO_2 without the involvement of gaseous O_2 but with the help of oxygen species in the catalysts. The CO_2 production over Co-CO_3-3T and Co-CO_3-5T were almost the same and were much higher than that over Co-CO_3-2T, whereas nearly no CO_2 was produced with Co-CO_3-1T, which agreed well with the aforementioned catalytic activity trend. Moreover, the surface lattice oxygen rather than the surface lattice oxygen in the catalysts should be responsible for the CO_2 evolution considering the relatively low reaction temperature. The higher CO_2 production over Co-CO_3-3T and Co-CO_3-5T could be attributed to the better mobility of the surface lattice oxygen on them, which in turn contributed to their excellent performance in propane oxidation.

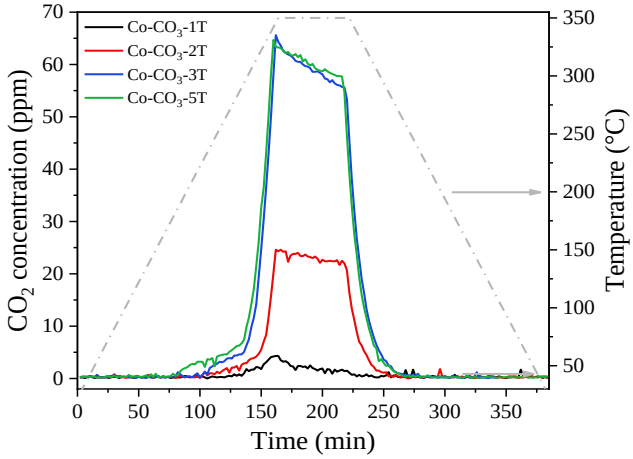

Fig. 6.7 CO_2 concentrations in propane oxidation without oxygen over the synthesized Co-CO_3-xT catalysts.

The long-term durability tests over the most active catalyst (Co-CO_3-3T) for propane oxidation were also carried out (Fig. 6.8). The test was performed as follows: the reactor was heated from temperature to 350 °C and held at the latter temperature for 1 h, then the temperature was decreased and controlled at 223 °C for 13.5 h and 193 °C for another 13.5 h. It was found that the conversion remained quite stable at both high and low conversion stages, demonstrating the good long-term stability of Co-CO_3-3T for propane oxidation.

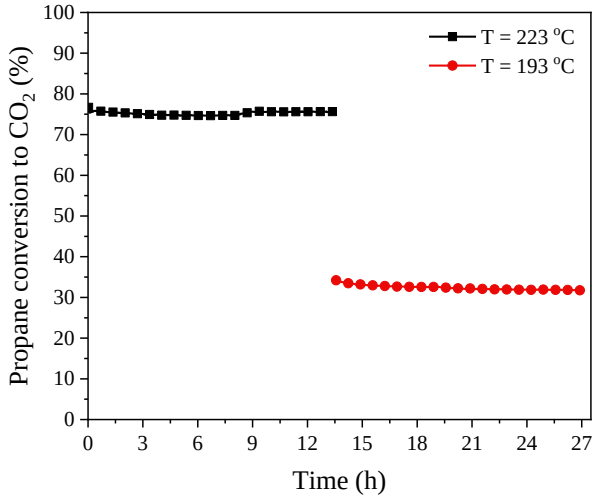

Fig. 6.8 Stability tests of propane oxidation over the Co-CO_3-3T catalyst. Reaction condition: 1000 ppm propane and synthetic air balance; WHSV = 40000 mL g^{-1} h^{-1}.

6.6 Discussions

In this study, it was proved that both the physicochemical properties of the synthesized Co-CO_3-xT catalysts and their catalytic activities for propane oxidation were influenced by the residual sodium in the catalysts. The sodium could be inserted into the Co_3O_4 spinel lattice, inducing defective structures, and leading to smaller crystallite size and larger specific surface

area of the Co_3O_4 catalysts. However, the residual sodium could meanwhile have negative influence on the reducibility and oxygen mobility of the catalysts. As a result, the residual sodium significantly affected the catalytic performance of the Co_3O_4 catalysts. For propane oxidation, Co-CO_3-3T presented the highest activity, with T_{90} of 236 °C (WHSV = 40,000 mL g^{-1} h^{-1}). However, Co-CO_3-2T with a little more residual sodium performed much worse (T_{90} = 258 °C) and Co-CO_3-1T with high sodium content displayed nearly no activity, which indicated that the residual sodium could be destructive to the catalytic activity of the Co_3O_4 catalysts for propane oxidation. Furthermore, the relatively worse activity of Co-CO_3-5T than that of Co-CO_3-3T suggested that proper number of washing steps of the precipitate during the catalyst preparation was important to maintain good textural properties as well as considerable catalytic activity of the Co_3O_4 catalysts. The better activity of Co-CO_3-3T was determined by its better reducibility and higher oxygen mobility, which favored the formation of active oxygen species that played a decisive role in the catalytic reaction.

6.7 Conclusions

Co_3O_4 catalysts with different contents of residual Na were prepared by washing the precipitate with different times and investigated in the catalytic oxidation of propane. The physicochemical properties of the catalysts were explored by a series of characterization methods. The following conclusions are drawn:

1. The residual sodium influenced both the physicochemical properties and the catalytic performance of the Co_3O_4 catalysts. Residual sodium could be partially inserted into the spinel lattice, inducing distortions and resulting in smaller crystallite size and larger specific surface area of the Co_3O_4 catalysts. Furthermore, the reducibility of the catalysts was inhibited by the presence of residual sodium.

2. For propane oxidation, trace residual sodium could poison the Co_3O_4 catalyst. The best performance was achieved on Co-CO_3-3T, which was traced to the better reducibility and higher oxygen mobility of Co-CO_3-3T.

3. Long-term stability tests showed that the activity of catalyst Co-CO3-3T was stable for propane oxidation.

References

[1] W. Hua, M. Li, Y. Guo, G. Chai, H. Liu, Y. Guo, L. Wang, W. Zhan. Catalytic combustion of vinyl chloride emissions over Co_3O_4 catalysts with different crystallite sizes. Rare Metals. 2021, 40: 817-827.

[2] A. Inayat, M. Ayoub, A.Z. Abdullah, S. Ullah, S.R. Naqvi. Decomposition of N_2O at low temperature over Co_3O_4 prepared by different methods. Environmental Progress & Sustainable Energy. 2019, 38(4): 13129.

[3] Q. Liu, L.C. Wang, M. Chen, Y. Gao, H.Y. He, K.N. Fan. Dry citrate-precursor synthesized nanocrystalline cobalt oxide as highly active catalyst for total oxidation of propane. Journal of Catalysis. 2009, 263: 104-113.

[4] B. Bai, H. Arandiyan, J. Li. Comparison of the performance for oxidation of formaldehyde on nano-Co_3O_4, 2D-Co_3O_4, and 3D-Co_3O_4 catalysts. Applied Catalysis B: Environmental. 2013, 142-143: 677-683.

[5] Z. Pu, H. Zhou, Y. Zheng, W. Huang, X. Li. Enhanced methane combustion over Co_3O_4 catalysts prepared by a facile precipitation method: Effect of aging time. Applied Surface Science. 2017, 410: 14-21.

[6] W. Zhang, J. Díez-Ramírez, P. Anguita, C. Descorme, J. L. Valverde, A. Giroir-Fendler. Nanocrystalline Co_3O_4 catalysts for toluene and propane oxidation: Effect of the precipitation agent. Applied Catalysis B: Environmental. 2020, 273: 118894.

[7] H. Wu, G. Pantaleo, G. Di Carlo, S. Guo, G. Marci, P. Concepción, A.M. Venezia, L.F. Liotta. Co_3O_4 particles grown over nanocrystalline CeO_2: influence of precipitation agents and calcination temperature on the catalytic activity for methane oxidation. Catalysis Science & Technology. 2015, 5: 1888-1901.

[8] E. Genty, J. Brunet, C. Poupin, S. Ojala, S. Siffert, R. Cousin. Influence of CO addition on the toluene total oxidation over Co based mixed oxide catalysts. Applied Catalysis B: Environmental. 2019, 247: 163-172.

[9] A. Choya, B. de Rivas, J.I. Gutiérrez-Ortiz, R. López-Fonseca. Effect of residual Na^+ on the combustion of methane over Co_3O_4 bulk catalysts prepared by precipitation. Catalysts. 2018, 8: 427.

[10] M. Haneda, Y. Kintaichi, N. Bion, H. Hamada. Alkali metal-doped cobalt oxide catalysts for NO decomposition. Applied Catalysis B: Environmental. 2003, 46: 473-482.

[11] L.F. Liotta. Catalytic oxidation of volatile organic compounds on supported noble metals. Applied Catalysis B: Environmental. 2010, 100: 403-412.

[12] Ž. Chromčáková, L. Obalová, F. Kovanda, D. Legut, A. Titov, M. Ritz, D. Fridrichová, S. Michalik, P. Kuśtrowski, K. Jirátová, K. Effect of precursor synthesis on catalytic activity of Co_3O_4 in N_2O decomposition. Catalysis Today. 2015, 257: 18-25.

[13] Z. Zhu, G. Lu, Z. Zhang, Y. Guo, Y. Guo, Y. Wang. Highly active and stable Co_3O_4/ZSM-5 catalyst for propane oxidation: Effect of the preparation method. ACS Catalysis. 2013, 3: 1154-1164.

[14] M. Sulaiman, N.A. Dzulkarnain, A.A. Rahman, N.S. Mohamed. Sol-gel synthesis and characterization of $LiNO_3$–Al_2O_3 composite solid electrolyte. Solid State Sciences. 2012, 14: 127-132.

[15] L.F. Liotta, G. Di Carlo, G. Pantaleo, G. Deganello. Catalytic performance of Co_3O_4/CeO_2 and Co_3O_4/CeO_2-ZrO_2 composite oxides for methane combustion: Influence of catalyst pretreatment temperature and oxygen concentration in the reaction mixture. Applied Catalysis B: Environmental. 2007, 70: 314-322.

[16] L. Hu, K. Sun, Q. Peng, B. Xu, Y. Li. Surface active sites on Co_3O_4 nanobelt and nanocube model catalysts for CO oxidation. Nano Research. 2010, 3: 363-368.

Chapter 7 General conclusions

This paper aims to develop high-performance Co_3O_4-based catalysts applied to catalytic oxidation of VOCs. The reaction mechanism of VC oxidation over the Co_3O_4 catalyst was investigated from the molecular scale based on the DFT calculations. Several series of Co_3O_4-based catalysts were prepared by different methods. The physicochemical properties and catalytic performance for VOCs oxidation, and the structure-performance relationship were studied. The main results are as follows:

1. The catalytic oxidation of VC over Co_3O_4 based on DFT

The reaction mechanism of VC oxidation on two representative (110) and (001) surfaces of Co_3O_4 was systematically explored at the molecular scale. The catalytic reaction pathway of VC oxidation consists of three steps, C-Cl bond scission after VC adsorption, CH_2CH oxidation and elimination of Cl species. The oxygen vacancy is indispensable to break the C-Cl bond on Co_3O_4(110), whereas the C-Cl bond cleavage can be achieved by the collaboration of two adjacent Co_{5c} sites at a lower energy barrier on Co_3O_4(001). Both surfaces are very reactive for CH_2CH oxidation. More importantly, the rate-determining step of VC oxidation over Co_3O_4 catalyst is identified to be the elimination of Cl species, and HCl is the preferential chlorine-containing product rather than Cl_2. In comparison with Co_3O_4(110), Co_3O_4(001) gives lower energy barrier for Cl elimination, indicating its potentially superior catalytic performance for VC oxidation. The barrier for Cl removal can be lowed by increasing the O coverage on the Co_3O_4(001) surface, which promotes the catalytic activity.

2. The catalytic performance of Zr-modified Co_3O_4 catalysts

The Zr-modified Co_xZr_y (x=95, 90, 80 and x +y=100) catalysts were prepared by the sol-gel method and applied in the catalytic oxidation of VC. The addition of Zr inhibits the sintering of Co_3O_4 particles during the preparation of the catalysts, reduces the crystallite size and increases the SSA of the catalysts. The higher the content of Zr, the more significant the increase of the SSA. The addition of Zr improves the reducibility and surface acidity of Co_3O_4, increases the content of surface Co^{2+} and adsorbed oxygen species, and promotes the formation of surface active oxygen species and oxygen mobility. The catalytic activity of the Co_xZr_y catalysts for VC oxidation increased with the addition of Zr and varied depending on the content of Zr. $Co_{95}Zr_5$ showed the highest activity due to the excellent reducibility, surface acidity and easy formation of active oxygen species. In terms of the stability, $Co_{95}Zr_5$ exhibited excellent performance, with no deactivation phenomenon in the stability evaluation of 100 h.

Another series of Zr-doped Co_3O_4 catalysts (x % Zr-Co_3O_4, x=0.5, 1, 1.5, 2) were prepared by the sol-gel method and applied in the catalytic oxidation of propane. Only a small amount

of Zr can be doped into the lattice of Co_3O_4. When the Zr content increases, it tends to form ZrO_x on the surface of the catalyst. Excessive Zr would result in the decrease of the actual doping amount of Zr. The moderate doping of Zr in Co_3O_4 can lead to a strong interaction between Zr dopant and Co_3O_4, resulting in smaller crystallite size, larger specific surface area, higher content of surface Co^{2+}, more defect structures and better reducibility of Co_3O_4. Meanwhile, the formation of active oxygen species and oxygen mobility of Co_3O_4 are also enhanced. There is a good correlation between the catalytic activity and physicochemical properties caused by the different doping amount of Zr. When the doping amount is the largest, the catalytic activity of the catalyst to propane oxidation is the best (1%Zr-Co_3O_4), with T_{50} and T_{90} of 219 and 249 ℃ respectively, which is mainly due to the excellent low temperature reducibility and abundance of surface active oxygen species. 1%Zr-Co_3O_4 also showed high stability in cycle and stability tests. Propane oxidation followed the Mars-van Krevelen mechanism over 1%Zr-Co_3O_4.

3. The catalytic performance of Nb-doped Co_3O_4 catalysts

The x% Nb-Co_3O_4 (x=0.5, 1, 1.5) catalysts with different doping content of Nb were prepared by the sol-gel method, and applied in the catalytic oxidation of propane and VC, respectively. There is a maximum amount of Nb that can be doped into the lattice of Co_3O_4. When the doping amount continues to increase, it tends to form NbO_x, and the actual doping amount of Nb would decrease. The moderate doping of Nb in Co_3O_4 can lead to smaller crystallite size, larger specific surface area, more defect structures, better reducibility, stronger surface acidity, higher content of surface Co^{2+} and active oxygen species, and better oxygen mobility of Co_3O_4. The catalytic activity and physicochemical properties of the x%Nb-Co_3O_4 catalysts can be correlated. 1%Nb-Co_3O_4 with the largest Nb doping content showed the best catalytic activity for propane and VC oxidation. For VC oxidation, the improvement of surface acidity caused by Nb doping enhanced the resistance to chlorine poisoning and reduced the generation of polychlorinated by-products. When a certain amount of water was added into the feed gas, the catalytic activity of 1%Nb-Co_3O_4 catalyst would not be decreased, and the formation of chlorine gas was inhibited. The most active catalyst for propane and VC oxidation (1%Nb-Co_3O_4) can maintain good stability in the stability tests.

4. The influence of residual sodium on the catalytic performance of Co_3O_4 catalysts

Co_3O_4 catalysts with different contents of residual Na were prepared by washing the precipitate with different times and investigated in the catalytic oxidation of propane. Residual Na can partially enter the Co_3O_4 lattice, causing lattice defects and increasing the SSA of the catalysts. At the same time, residual Na will negatively affect the reducibility and oxygen mobility of the catalysts. A small amount of residual Na will cause fatal damage to the catalytic activity of the catalysts for propane oxidation. The catalyst (Co-CO_3-3T) obtained by washing

the precipitate for three times in the preparation process showed the best catalytic activity, which was mainly due to the better reducibility and oxygen mobility, and easier formation of active oxygen species involved in the oxidation reaction. The Co-CO_3-3T catalyst showed excellent stability in the stability test.

List of papers published during doctoral study

List of journal papers published during doctoral study：

1. Guangtao Chai, Weidong Zhang, Leonarda Francesca Liotta, Mingqi Li, Yanglong Guo*, Anne Giroir-Fendler*. Total oxidation of propane over Co_3O_4-based catalysts: Elucidating the influence of Zr dopant. Applied Catalysis B: Environmental. 2021, 298: 120606.

2. Guangtao Chai, Sineng Pan, Yanglong Guo*, Wangcheng Zhan, Li Wang, Yun Guo, Haifeng Wang*. Insight into the surface-tuned activity and Cl_2/HCl selectivity in the catalytic oxidation of vinyl chloride over Co_3O_4(110) versus (001): A DFT study. The Journal of Physical Chemistry C. 2021, 125: 16975-16983.

3. **Guangtao Chai**, Dan Du, Chao Wang*, Chuanhui Zhang, Luis Cardenas, Nicolas Bion, Yanglong Guo*, Sonia Gil*, Anne Giroir-Fendler*. Spinel Co_3O_4 oxides-supports synergistic effect on catalytic oxidation of toluene. Applied Catalysis A, General. 2021, 614: 118044.

4. **Guangtao Chai**, Weidong Zhang, Yanglong Guo*, Jose Luis Valverde, Anne Giroir-Fendler*. The influence of residual sodium on the catalytic oxidation of propane and toluene over Co_3O_4 catalysts. Catalysts. 2020, 10: 867.

5. Chao Wang, Wenchao Hua, **Guangtao Chai**, Chuanhui Zhang*, Yanglong Guo*. Insights into the morphological effect of Co_3O_4 crystallite on catalytic oxidation of vinyl chloride. Catalysts. 2019, 9: 408.

6. Wenchao Hua, Chuanhui Zhang, Yanglong Guo*, **Guangtao Chai**, Chao Wang, Yun Guo, Li Wang, Yunsong Wang, Wangcheng Zhan*. An efficient $Sn_yMn_{1-y}O_x$ composite oxide catalyst for catalytic combustion of vinyl chloride emissions. Applied Catalysis B: Environmental. 2019, 255: 117748.

7. Wenchao Hua, Mingqi Li, Yanglong Guo*, **Guangtao Chai**, Hao Liu, Yun Guo, Li Wang, Wangcheng Zhan*. Catalytic combustion of vinyl chloride emissions over Co_3O_4 catalysts with different crystallite sizes. Rare Metals. 2021, 40: 817-827.

8. Hao Liu, Xian, Li, Qiguang Dai, Hailin Zhao, **Guangtao Chai**, Yanglong Guo*, Yun Guo, Li Wang, Wangcheng Zhan*. Catalytic oxidation of chlorinated volatile organic compounds over Mn-Ti composite oxides catalysts: Elucidating the influence of surface acidity. Applied Catalysis B: Environmental. 2021, 282: 119577.

List of conference papers published during doctoral study：

1. **Guangtao Chai**, Leonarda Francesca Liotta, Yanglong Guo, Anne Giroir-Fendler. Total oxidation of propane and toluene over trace zirconium doped Co_3O_4 catalysts. 17th International Congress on Catalysis (ICC). 2020. San Diego, United States. (poster)

2. **Guangtao Chai**, Jing Yang, Yanglong Guo, Anne Giroir-Fendler. The effect of zirconium on the catalytic oxidation of vinyl chloride over Co_3O_4-based catalysts. 11th International Conference on Environmental Catalysis. 2020. Manchester, United Kingdom. (poster)

3 **Guangtao Chai**，Haifeng Wang，Yanglong Guo. The catalytic oxidation of vinyl chloride oove Co_3O_4 based on density functional theory. 16th National Youth Conference on Catalysis. 2016. China (poster)

4 **Guangtao Chai**，Chai Wang，Wenchao Hua，Yanglong Guo，Wangcheng Zhan，Yun Guo，Li Wang，Guanzhong Lu. Morphological effect of Co_3O_4 crystallite on the catalytic oxidation of vinyl chloride. 18th National Conference on Catalysis. 2017. China (poster)

Acknowledgements

Time flies. Looking back the past, I was so stressed that I could not sleep well because of various difficulties in my experiments at the very beginning of my postgraduate studies. I had suspected that I was not suitable for the doctoral studies, and I also had the idea of dropping out. The disappointment and sense of loss made me crazy when the experiments results did not meet my psychological expectations. But now, after years of postgraduate study and exercise, I think if I meet similar situations in the future, I will be more calm to face them. Thanks for this period of time and experience in my life. I really grew up a lot.

First of all, I would like to express my sincere thanks to my supervisors, Prof. Anne Giroir-Fendler and Prof. Yanglong GUO, for your careful guidance in every stage, from the topic selection and experimental guide, to the discussion and manuscript modification. It is you who taught me how to do the scientific research correctly and guide me walk and move forward in the road of scientific research. Perhaps in the future I will do some different work, but the whole train of thought and logic thinking mode is permanent, which is going to help me for life. In addition to scientific research, I also want to thank you for your care in my life. I would like to express my thanks to my supervisor Anne Giroir-Fendler, who often took time out of her busy work to give me precise guidance on my academic research and thesis direction during the two-year joint training at UCBL1. Giroir-Fendler's humorous personality and positive and optimistic attitude towards life have helped me quickly adapt to the pace of life and work in France.

I would like to acknowledge Prof. Haifeng WANG from the Computing Center of ECUST for his guidance and help in my theoretical computing work. I would like to acknowledge Prof. Leonarda Francesca Liotta and Prof. Jose Luis Valverde for the advice and help in my experimental work. Thanks to Prof. Philippe Vernoux, Prof. Christian George, Sonia Gil, Antoinette Boreave, Pierrick Peixoto, Prof. Yun Guo, Prof. Wangcheng Zhan, Yunsong Wang, Li Wang for your guidance and help in my experiment.

Thanks also to my fellows and friends, Dr. Paola Anguita, Dr. Ioanna Kalaitzidou, Dr. Guillaume Petaud, Dr. Weidong Zhang, Dr. Guillermo Pedrosa, Brenda De-Araujo, Wenchao Hua, Yu Sun, Hao Liu, Hailin Zhao, etc. You gave me a lot of instructions and technical supports during my research in both institutes and universities.

My special thanks should be given to my family for the understanding and support. Your encouragement during these years make me go forward with more determination. In the end, I would like to thank myself. Never give up. Come on!